

PHOTO-INDUCED PROPERTIES OF BISMUTH FERRITE THIN FILMS  
PREPARED BY RF MAGNETRON SPUTTERING TECHNIQUE



A Thesis Submitted in Partial Fulfillment of the Requirement for the  
Degree of Doctor of Philosophy in Physics  
Suranaree University of Technology  
Academic Year 2021

สมบัติที่เกิดจากการเหนี่ยวนำด้วยแสงของฟิล์มบางบิสมีทเฟอร์ไรต์ที่เตรียม  
ด้วยเทคนิคอาร์เอฟแมกนีตรอนสเปตเตอริง

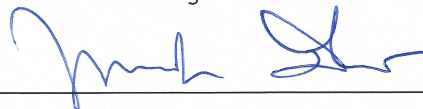


วิทยานิพนธ์นี้เป็นส่วนหนึ่งของการศึกษาตามหลักสูตรปริญญาวิทยาศาสตรดุษฎีบัณฑิต  
สาขาวิชาฟิสิกส์  
มหาวิทยาลัยเทคโนโลยีสุรนารี  
ปีการศึกษา 2564

PHOTO-INDUCED PROPERTIES OF BISMUTH FERRITE THIN FILMS PREPARED  
BY RF MAGNETRON SPUTTERING TECHNIQUE

Suranaree University of Technology has approved this thesis submitted in  
partial fulfillment of the requirements for the Degree of Doctor of Philosophy.

Thesis Examining Committee



(Assoc. Prof. Dr. Panomsak Meemon)

Chairperson



(Asst. Prof. Dr. Wittawat Saenrang)

Member (Thesis Advisor)



(Assoc. Prof. Dr. Worawat Meevasana)

Member (Thesis Co-Advisor)



(Assoc. Prof. Dr. Prayoon Songsiriritthigul)

Member



(Dr. Narong Chanlek)

Member



(Dr. Hideki Nakajima)

Member



(Assoc. Prof. Dr. Chatchai Jothityangkoon)

Vice Rector for Academic Affairs  
and Quality Assurance

(Prof. Dr. Santi Maensiri)

Dean of Institute of Science

พีรวัฒน์ เลาะทะนะ : สมบัติที่เกิดจากการเหนี่ยวนำด้วยแสงของฟิล์มบางบิสมาทเฟอร์ไรต์ที่เตรียมด้วยเทคนิคอาร์เอฟแมกนีตรอนสปัตเตอริง (PHOTO-INDUCED PROPERTIES OF BISMUTH FERRITE THIN FILMS PREPARED BY RF MAGNETRON SPUTTERING TECHNIQUE). อาจารย์ที่ปรึกษา : ผู้ช่วยศาสตราจารย์ ดร.วิฑูรย์ แสนรงค์, 81 หน้า.

คำสำคัญ: โครงสร้างเฮเทอโรของฟิล์มบางบิสมาทเฟอร์ไรต์/สมบัติของความต้านทานไฟฟ้าที่ไวต่อแสง/ระบบเซ็นเซอร์แสง/การวัดค่าความนำไฟฟ้า

สมบัติของความนำไฟฟ้าที่ไวต่อแสงของโครงสร้างเฮเทอโรโรนั้นมีความน่าสนใจเป็นอย่างมาก และสามารถนำมาประยุกต์ใช้ในระบบเซ็นเซอร์แสงและอุปกรณ์อิเล็กทรอนิกส์แบบโฟโตอิเล็กทรอนิกส์ได้ โดยสารเพอโรสไกต์ที่มีโครงสร้างแบบเฮเทอโร เช่น ฟิล์มบางบิสมาทเฟอร์ไรต์บนสตรอนเทียมไททานเตอไซด์ศึกษาการนำไฟฟ้าบริเวณรอยต่อที่เกิดจากกลุ่มอิเล็กตรอนแก๊สสองมิติ โดยมีการคำนวณตามทฤษฎีได้ระบุไว้ว่ามีกลุ่มอิเล็กตรอนแก๊สสองมิติบริเวณรอยต่อนี้ ในงานวิจัยนี้ได้นำเสนอการควบคุมค่าการนำไฟฟ้าของฟิล์มบางบิสมาทเฟอร์ไรต์บนสตรอนเทียมไททานเตอไซด์ โดยการให้สนามไฟฟ้าจากภายนอก ร่วมกับการฉายแสงในย่านอัลตราไวโอเล็ต โดยฟิล์มบางบิสมาทเฟอร์ไรต์ถูกเคลือบด้วยระบบอาร์เอฟแมกนีตรอนสปัตเตอริงทั้งหมดมีเงื่อนไข 3 เงื่อนไข ได้แก่ การปลูกฟิล์มที่อุณหภูมิห้อง (RT) จากนั้นเผาในบรรยากาศที่อุณหภูมิ 600 °C เป็นเวลา 2 ชั่วโมง (CAL) และการปลูกฟิล์มที่อุณหภูมิสูงที่ 600 °C (HT) และโครงสร้างแบบเฮเทอโรที่ได้ศึกษานั้นมี 3 รูปแบบ คือ Au/STO, Au/mBFO/STO (m ย่อมาจาก masked) และ Au/BFO/STO ในการทดลองนี้ฟิล์มบางบิสมาทเฟอร์ไรต์ที่ปลูกในเงื่อนไข RT จะเป็นตัวอย่างหลักในการศึกษาความนำไฟฟ้า และการควบคุมค่าการนำไฟฟ้าด้วยการให้สนามไฟฟ้าจากภายนอก ในขณะที่เงื่อนไข CAL และ HT นำมาเปรียบเทียบกับเงื่อนไข RT ของโครงสร้างเฮเทอโรแบบ Au/BFO/STO เพียงเท่านั้น การศึกษาความนำไฟฟ้าจะมีทั้งแบบฉายแสงในย่านอัลตราไวโอเล็ตและไม่มีการฉายแสง จากผลการศึกษาพบว่าค่าการนำไฟฟ้าของตัวอย่างเพิ่มขึ้นอย่างรวดเร็วและทำให้เกิดตำแหน่งว่างของออกซิเจนจนเกิดการเหนี่ยวนำกลุ่มอิเล็กตรอนแก๊สสองมิติบนรอยต่อได้ ซึ่งค่าการนำไฟฟ้าของโครงสร้างเฮเทอโรแบบ Au/mBFO/STO เพิ่มขึ้นแบบไม่เป็นเชิงเส้น และค่าการนำไฟฟ้านี้มากกว่าผลของฟิล์มบางบิสมาทเฟอร์ไรต์และสตรอนเทียมไททานเตอไซด์รวมกัน ซึ่งมีค่าความนำไฟฟ้าอยู่ที่ ~76.46 นาโนซีเมนส์ ในขณะที่ฟิล์มบางบิสมาทเฟอร์ไรต์และสตรอนเทียมไททานเตอไซด์มีค่าประมาณ ~0.23 และ ~3.67 นาโนซีเมนส์ตามลำดับ นอกจากนี้ค่าความนำไฟฟ้ายังสามารถควบคุมให้มีค่าเพิ่มขึ้นหรือลดลงได้โดยการให้สนามไฟฟ้าจากภายนอกเพื่อสลับทิศทางของโพลาริเซชันของฟิล์มบางบิสมาทเฟอร์ไรต์ ซึ่งค่าความนำไฟฟ้าของโครงสร้างเฮเทอโรแบบ Au/mBFO/STO จะมีเพิ่มขึ้น  $\Delta\sigma = 58.91$  นาโนซีเมนส์และ

ลดลง  $\Delta\sigma = 9.93$  นาโนซีเมนส์ หลังจากการให้สนามไฟฟ้าจากภายนอกในทิศทางและทิศลบภายใต้การฉายแสงในย่านอัลตราไวโอเลตร่วมด้วยตามลำดับ นอกจากนี้ยังสามารถสลับทิศทางของไดโอดระหว่างการไบอัสตรงและการไบอัสย้อนกลับได้อีกด้วย ในลำดับสุดท้ายลักษณะเฉพาะของแรงดันไฟฟ้ากับกระแสไฟฟ้า (I-V curve) แสดงให้เห็นถึงพฤติกรรมของตัวอย่างเป็นเซลล์แสงอาทิตย์ที่อนุมาณถึงสนามไฟฟ้าแบบโพลาริไซในในตัวในฟิล์มบางบิสมัทเพอร์ไรต์ ภายใต้การฉายแสงในย่านอัลตราไวโอเลตร่วมด้วย การใช้สนามไฟฟ้าเพื่อเปลี่ยนโพลาริเซชันของฟิล์มบางบิสมัทเพอร์ไรต์สามารถควบคุมการลัดวงจรกระแส ( $I_{sc}$ ) และเปิดวงจรแรงดันไฟฟ้า ( $V_{oc}$ ) ให้มีค่าเพิ่มขึ้นหรือลดลงได้จากผลการทดลองเหล่านี้อาจจะใช้ในระบบเซ็นเซอร์แสงและพัฒนาอุปกรณ์โฟโตอิเล็กทรอนิกส์รุ่นต่อไปได้



สาขาวิชาฟิสิกส์

ปีการศึกษา 2564

ลายมือชื่อนักศึกษา พิชญ์ เกษณะ

ลายมือชื่ออาจารย์ที่ปรึกษา วิภาวดี กลมรุ่ง

ลายมือชื่ออาจารย์ที่ปรึกษาร่วม [ลายมือ]

PEERAWAT LAOHANA : PHOTO-INDUCED PROPERTIES OF BISMUTH FERRITE  
THIN FILMS PREPARED BY RF MAGNETRON SPUTTERING TECHNIQUE. THESIS  
ADVISOR : ASST. PROF. WITTAWAT SAENRANG, Ph.D. 81 PP.

Keyword: BIFEO<sub>3</sub> THIN FILMS HETEROSTRUCTURE/PHOTORESISTIVE PROPERTY/PHOTO-  
SENSING SYSTEMS/CONDUCTANCE MEASUREMENT

Photoconductivity of a heterostructure is very interesting and can be applied in photo-sensing systems and photo-electric electronic devices. The perovskite heterostructures of BiFeO<sub>3</sub> (BFO) on SrTiO<sub>3</sub> (STO) have been studied for the photo-induced conductance of two-dimensional electron gas (2DEG), where the theoretical calculation indicates that a 2DEG exists at the interfaces. In this thesis, we present how to control the conductance of BFO thin films as a function of an external electric field and UV light irradiation. We prepared BFO thin films on STO (100) using an RF magnetron sputtering system with 3 different conditions as follows: at room temperature (RT), then calcination at 600 °C for 2 hours (CAL), in air, and at high temperature 600 °C (HT). There are 3 configurations of the heterostructure as follows: Au/STO, Au/mBFO/STO (m stands for masked), and Au/BFO/STO. In the experiment, the BFO thin films with RT conditions were the main sample to study the conductance of the heterostructure in 3 configurations and the effect of biasing high voltage. While the CAL and HT conditions were compared to the conductance with the RT condition, only the Au/BFO/STO configuration was tested. The conductance was studied with and without UV irradiation. It was found that when the UV light was turned on, the conductance of all samples increased abruptly due to the formation of oxygen-vacancy-induced 2DEG states with slow-charging. The conductance has non-linearly increased, with the Au/mBFO/STO configuration having greater conductance than the total of each individual BFO film and STO crystal. Under UV exposure, the conductance was ~76.46 nS, while the BFO film and STO crystal were ~0.23 nS and ~3.67, respectively. Moreover, the conductance can be controlled to increase or decrease by using an electric field to switch the ferroelectric polarization of BFO thin films. The conductances of the Au/mBFO/STO configuration were increased by  $\Delta\sigma = 58.91$  nS and

decreased by  $\Delta\sigma = 9.93$  nS after the positive and negative bias under UV illumination. The electric fields with positive and negative bias can also be switched in the diode directions with the forward and reverse bias directions, respectively. Finally, the current-voltage characterization (I-V curve) demonstrated the photovoltaic behaviors that inferred the self-polarized and built-in electric field in BFO thin films under illumination. The short-circuit current ( $I_{sc}$ ) and open-circuit voltage ( $V_{oc}$ ) can be controlled to increase or decrease by using an electric field to change the polarization of BFO thin films. These effects may find new applications in photo-sensing systems with research development for next generation optoelectronic devices.



School of Physics  
Academic Year 2021

Student's Signature Peerawat Laohana  
Advisor's Signature วิมล วัฒนชัย  
Co-Advisor's Signature สมชาย

## ACKNOWLEDGEMENTS

This thesis was completed with the help and support of several people. First, I would like to thank my advisor, Asst. Prof. Dr. Wittawat Saenrang. He provided this opportunity and led me along the path of research under his supervision. He is an excellent advisor due to his kindness, dedication, and encouragement. I learned a great deal from him, including the research process, data collection, data analysis, and time management. My experience working with him has been very enjoyable. With his leadership, he has helped and supported me through every step to get to where I am today. I also would like to thank my co-advisor, Assoc. Prof. Dr. Worawat Meevasana. He is a very kind advisor. I was very fortunate to participate in his research group. I was introduced to his research by a senior student. While interviewing, I became interested in the work he had done. Afterwards he gave me his phone number so that I could contact him to further discuss future opportunities. The inspiration I received from him enabled me to complete this research. He also provided me with an opportunity to perform research abroad for the first time at Soleil Synchrotron in France and sent me to train on the coating machine in Shanghai, China. So for these reasons and more, I am extremely appreciative to both of my advisors.

For the initial installation of the RF magnetron sputtering machine, I would like to thank Dr. Pat Photongkam and Mr. Tachgiss Jampreecha. Dr. Photongkam, a scientist at the Synchrotron Light Research Institute, helped to repair a vacuum operating problem until it could run and be used. Mr. Jampreecha, a Ph.D. student, helped me to design the base for the chamber and set up all components of the system.

I am extremely grateful to the following members of the thesis examination committee: Assoc. Prof. Dr. Panomsak Meemon, Assoc. Prof. Dr. Prayoon Songsiriritthigul, Dr. Narong Chanlek, and Dr. Hideki Nakajima for reviewing my thesis and providing constructive feedback during my Ph.D. defense.

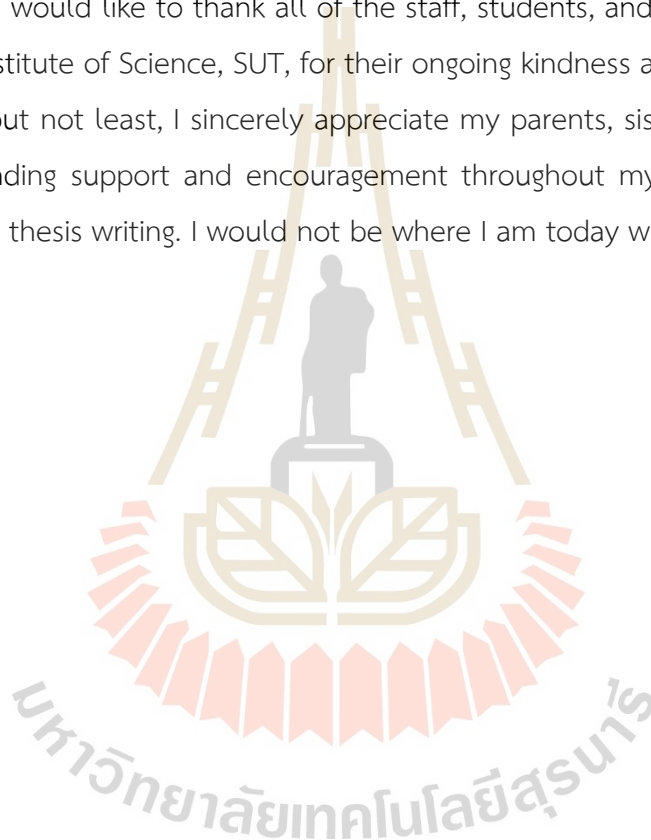
I would like to acknowledge the Science Achievement Scholarship of Thailand (SAST) for providing financial support while pursuing my bachelor's degree.

I would like to thank all the members of the Meevasana group, particularly Dr. Siwat Polin, Dr. Sumet Siriroj, and Ms. Manlika Sriondee, along with Asst. Prof. Dr. Wittawat Saenrang's Research Group (WSRG) for their support and guidance through a variety of challenges. We often had good discussions on a variety of topics. Additional thank you to Dr. Warakorn Jindata for reviewing the paper for publication and helping to analyze the results and to Dr. Sujinda Chaiyachad, Ms. Aissara Rasritat, and Mr. Nantawat Tanapongpisit for helping with the measurements.

Also, I would like to thank all of the staff, students, and friends at the School of Physics, Institute of Science, SUT, for their ongoing kindness and support.

Last but not least, I sincerely appreciate my parents, sisters, and girlfriend for their neverending support and encouragement throughout my Ph.D. studies, thesis research, and thesis writing. I would not be where I am today without all of you.

Peerawat Laohana



# CONTENTS

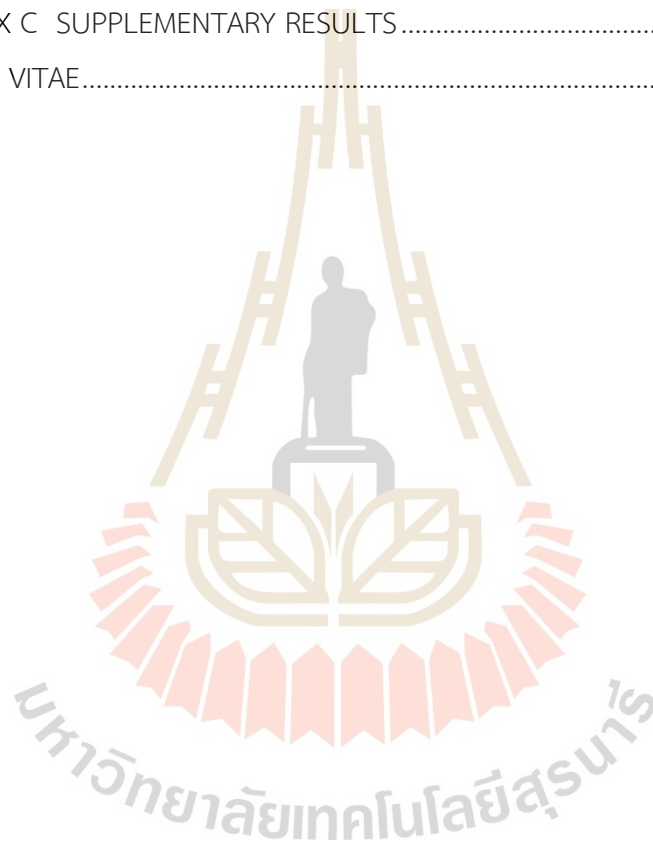
	Page
ABSTRACT IN THAI .....	I
ABSTRACT IN ENGLISH .....	III
ACKNOWLEDGEMENTS .....	V
CONTENTS .....	VII
LIST OF FIGURES .....	X
<b>CHAPTER</b>	
<b>I INTRODUCTION .....</b>	<b>1</b>
1.1 Background and motivation.....	1
1.2 Research objectives .....	4
1.3 Outline of thesis .....	4
<b>II LITERATURE REVIEWS.....</b>	<b>5</b>
2.1 Bismuth ferrite (BiFeO <sub>3</sub> ).....	5
2.1.1 Preparation of Bismuth ferrite thin films.....	6
2.1.2 Ferroelectric property in Bismuth ferrite thin films .....	10
2.2 Dynamic mechanism.....	12
2.2.1 Photoconductivity effect.....	12
2.2.2 Photoelectric effect.....	15
2.2.3 Ferroelectric photovoltaic effect .....	16
2.3 Non-dynamic mechanism .....	20
2.3.1 Electronic structures of two-dimensional electron gases .....	20
2.3.2 Effects of oxygen vacancy .....	24
<b>III THIN FILMS PREPARATION AND CHARACTERIZATION .....</b>	<b>26</b>
3.1 Thin film deposition and sample processing.....	26
3.1.1 BiFeO <sub>3</sub> thin films deposition by RF magnetron sputtering.....	26
3.1.2 Fabrication of Au top electrode.....	27

## CONTENTS (Continued)

	<b>Page</b>
3.2 Basic characterization.....	28
3.2.1 X-ray diffraction (XRD).....	28
3.2.2 Atomic force microscope (AFM).....	29
3.2.3 Field emission scanning electron microscope (FESEM).....	30
3.2.4 Energy dispersive X-ray spectroscopy (EDS).....	31
3.2.5 Ultraviolet visible spectroscopy (UV-VIS).....	31
3.3 Conductance characterization.....	33
3.3.1 Principle of 2-wire sensing.....	33
3.3.2 Conductance measurement.....	33
3.3.3 Sample configurations.....	34
<b>IV RESULTS AND DISCUSSION.....</b>	<b>38</b>
4.1 Basic characterization.....	38
4.1.1 X-ray diffraction (XRD).....	38
4.1.2 Atomic force microscope (AFM).....	39
4.1.3 Field emission scanning electron microscope (FESEM).....	40
4.1.4 Energy dispersive X-ray spectroscopy (EDS).....	40
4.1.5 Ultraviolet visible spectroscopy (UV-VIS).....	41
4.2 Conductance characterization.....	43
4.2.1 Various configurations.....	43
4.2.2 Various thicknesses of BFO thin films.....	44
4.2.3 Various Au/mBFO/STO and Au/BFO/STO configurations.....	47
4.2.4 Various BiFeO <sub>3</sub> conditions of the Au/BFO/STO configuration.....	49
4.2.5 The effect of the electric field of the Au/mBFO/STO configuration....	50
4.3 Current-voltage characterization.....	51
4.4 Mechanism and discussion.....	54
<b>V CONCLUSION AND FUTURE RESEARCH.....</b>	<b>56</b>
5.1 Conclusions.....	56
5.2 Improvement and future research.....	57

## CONTENTS (Continued)

	Page
REFERENCES .....	58
APPENDICES.....	68
APPENDIX A RF MAGNETRON SPUTTERING SYSTEMS.....	69
APPENDIX B PUBLICATIONS AND PRESENTATIONS .....	75
APPENDIX C SUPPLEMENTARY RESULTS.....	77
CURRICULUM VITAE.....	81



## LIST OF FIGURES

Figure	Page
2.1 A schematic of the rhombohedral structure of perovskite BFO (R3c space-group) with two unit cells along [111] direction.....	6
2.2 The schematic diagram illustrating the basic components of a magnetron sputtering system .....	7
2.3 The ferroelectric hysteresis loop of BFO/SRO/STO thin films (a) at a frequency of 15 kHz and (b) at different orientation of (001), (101), and (111) BFO films.....	11
2.4 The ferroelectric hysteresis loop at a frequency of 1 kHz (a) BFO thin films on SRO/Pt/TiO <sub>2</sub> /SiO <sub>2</sub> /Si substrate at different thicknesses of 190-600 nm and (b) amorphous BFO thin films on Pt/Ti/SiO <sub>2</sub> /Si substrate with various applied electric fields.....	12
2.5 The schematic diagram of a bulk material with a cross section of the current path (A), the length between the electrodes (L), and the applied voltage between the two electrodes (V) with incident electromagnetic radiation ( $\lambda$ ).....	14
2.6 (a) The I-V characteristics in the dark (blue) and during UV exposure (red) on BFO/LAO thin films and the schematic device geometry (insert), and (b) the conductivity as a function of time and the extended plot of the blue area as a gradual decay with the dark condition (insert figure).....	14
2.7 The schematic diagram of ferroelectric photovoltaic device with (a) vertical and (b) lateral structures.....	16

## LIST OF FIGURES (Continued)

Figure	Page
2.8 (a) The schematic device geometry for PFM and current density $J(E)$ measurements on Ag/BFO/Ag samples with electric pulses $\pm 150$ V ( $E \approx 17$ kV cm <sup>-1</sup> ). (b) The topography (top panel) and the out-of-plane PFM image with color-scaled after +150 V pulse (middle panel) and -150 V pulse (bottom panel). (c) The $J(E)$ curves after the +150 V, -150 V, and +150 V pulses, respectively.....	17
2.9 The schematic diagram for I-V measurement with electrodes oriented (a) parallel and (b) perpendicular to the domain wall geometry. The I-V characteristics in the dark (blue) and after white-light exposure (red) on BFO/DSO thin films of the electrodes oriented (c) parallel and (d) perpendicular to the domain walls .....	18
2.10 (a) The I-V characteristics under white-light exposure on BFO/DSO thin films with electrodes oriented perpendicular to the domain wall for as-grown (black) and after bias a voltage pulses of $\pm 200$ V (blue and red). (b) PFM images of the device structures as-grown (top panel), +200 V (middle panel), and -200 V (bottom panel).....	19
2.11 The I-V characteristics in the dark (black open circles) and under green laser illumination (black solid circles) with (a) downward and (b) upward polarizations. The insets for (a) and (b) is the schematic device geometry with downward and upward polarization for I-V measurement, respectively.....	20
2.12 The 2DEG states of the lightly 0.1% La-doped STO after exposure to synchrotron (UV) light. (a) ARPES data of La-doped STO at $T = 20$ K, with corresponding momentum distribution curves in (b). (b) the parabolic fits to the data points from the ARPES data. (c) Fermi surface map from the ARPES data. (d) the schematic Fermi surface and band dispersions obtained from the measured electronic structure.....	21

## LIST OF FIGURES (Continued)

Figure	Page
2.13 The 2DEG states of the STO under exposure to synchrotron (UV) light. (b) The valence band of the oxygen state ( $O_{2p}$ ) and the oxygen-vacancy state as a function of UV irradiation dose (the zoomed-in graph is shown in the inset).....	22
2.14 The creation of 2DEG at the BFO/STO interface with (a) surface topographic image and (b) nanoscale current mapping .....	23
2.15 The measured resistance (conductance) of the STO surface where the on-off UV irradiation process and the schematic diagram of the measurement setup (inset figure) (a) Suwanwong et al. and (b) Jaiban et al., respectively.....	25
3.1 The schematic diagram of the planar electrode of (a) Au/STO, (b) Au/mBFO/STO, and (c) Au/BFO/STO.....	27
3.2 The x-ray diffraction principle.....	28
3.3 Basic principle of atomic force microscopy .....	29
3.4 The field emission scanning electron microscope (FESEM) principle .....	30
3.5 A schematic of the main components in a UV-Vis spectrophotometer .....	32
3.6 The schematic diagram of resistance measuring circuit of 2-wire system.....	33
3.7 The schematic device geometry for conductance measurements of the Au/STO configuration.....	34
3.8 (a) The device geometry (top right) of STO crystal and Au/mBFO/STO configuration with Au electrodes. The optical surface image (top left) and surface morphology (bottom) and (b) the schematic device geometry for conductance measurements of Au/mBFO/STO configuration.....	35
3.9 The schematic device geometry for conductance measurements of Au/mBFO/STO configuration with applying high voltage on the top and bottom electrodes.....	35
3.10 The schematic device geometry for conductance measurements of Au/BFO/STO configuration.....	36

## LIST OF FIGURES (Continued)

Figure	Page
3.11 (a) The schematic diagram of the Au/mBFO/STO configuration during bias high voltage. (b) the direction of positive and negative bias high voltage. ....	37
4.1 XRD spectra of BFO/STO thin films at RT, HT, and CAL conditions. The diffraction peaks labeled with “*” are from the STO (100) substrates diffracted by the Cu-K $\beta$ radiation. ....	39
4.2 The line profile of the BFO/STO sample at 30 min and the AFM image. ....	40
4.3 FESEM images of (a) STO crystal and (b) BFO/STO sample in the RT condition at a deposition time of 1 min. ....	40
4.4 EDS elemental analysis of (a) STO crystal. BFO on STO thin films in RT conditions with deposition times of (b) 1 min, (c) 5 min, and (d) 30 min. ....	41
4.5 The plots between $(\alpha h\nu)^2$ versus $h\nu$ of BFO/STO (RT) conditions with the thickness of 20, 115, and 743 nm. ....	42
4.6 The transmission of BFO films at a monochromatic light wavelength of 405 nm with the thickness of 20, 115, and 743 nm. ....	42
4.7 The time-dependent conductance with different configurations with multiple UV light exposure cycles with Au/SiO <sub>2</sub> /Si, Au/mBFO/SiO <sub>2</sub> /Si, Au/STO crystal, and Au/mBFO/STO with the 115-nm-thick BFO films. ....	44
4.8 The time-dependent conductance of Au/STO and Au/mBFO/STO configurations with different BFO thicknesses of 20, 115, and 743 nm with multiple UV light exposure cycles. ....	45
4.9 The stack column of the maximum conductance at different configurations with Au/mBFO/SiO <sub>2</sub> /Si (115-nm-thick BFO films), Au/STO, and Au/mBFO/STO (20-nm-thick BFO films) configurations under illumination. ....	45
4.10 The transmission (black) and conductance (red) of BFO films with thicknesses of 20, 115, and 743 nm with the experiment data (symbol) and fitted data (line). ....	46

## LIST OF FIGURES (Continued)

Figure	Page
4.11 The conductance of Au/STO and Au/mBFO/STO (20-nm-thick BFO films) configurations with and without (dark) UV illumination.....	47
4.12 The time-dependent conductance with different configurations with multiple UV light exposure cycles of Au/mBFO/STO and Au/BFO/STO configurations. ....	48
4.13 Schematic diagram of the 2DEG creation with (a) Au/mBFO/STO and (b) Au/BFO/STO configurations.....	48
4.14 The time-dependent conductance with RT, HT, and CAL conditions with multiple UV light exposure cycles.....	50
4.15 The time-dependent conductance of the Au/mBFO/STO configuration With the as-grown, after positive and negative bias conditions (applying electric fields across the BFO/STO interface) with multiple UV light exposure cycles. ....	51
4.16 The I-V characteristics of the Au/mBFO/STO configuration with the as-grown, after positive, and negative bias conditions under UV light exposure (a) from -10.0 V to 10.0 V and (b) from -5.0 V to 5.0 V. These zoomed in areas clearly present photovoltaic behaviors. ....	52
4.17 (a) Conductance and voltage with UV illumination with the as-grown, after positive, and negative bias. (b) The I-V characteristics of the Au/mBFO/STO configuration with the as-grown, after positive, and negative bias in the dark condition. ....	53
4.18 The I-V characteristics of the Au/mBFO/Si configuration with the as-grown, after positive, and negative bias with (a) under UV light exposure and (b) in the dark condition. ....	54

## LIST OF FIGURES (Continued)

Figure	Page
4.19 Schematic diagram of UV-light-induced oxygen vacancies. (a) STO crystal and BFO/STO interface with (c) zero bias, (e) positive bias, and (g) negative bias. The electrostatic potential changes as a function of depth Z from the surface to the bulk. (b) STO crystal and BFO/STO interface with the (d) zero bias, (f) positive bias, and (h) negative bias. The yellow and pink positive charges represent the oxygen vacancy charge of STO and the BFO/STO interface, respectively. The injection charges are red and blue charges for positive and negative bias, respectively. The green charges represent polarization charges, while the black and white arrows represent polarization directions ( $P$ ) caused by UV light and bias, respectively.....	55
A.1 A 2-dimensional drawing of the cylindrical stainless steel chamber.....	69
A.2 A schematic diagram of vacuum systems.....	70
A.3 A schematic diagram of the water system.....	71
A.4 A schematic diagram of the RF power supply systems. Noted: e=Electrical line. ....	72
A.5 A schematic diagram of the substrate holder. ....	73
C.1 The thickness of the BFO/STO at RT, HT, and CAL conditions.....	77
C.2 FESEM images of the BFO/STO sample in RT, HT, and CAL conditions with deposition times of 1, 5, and 30 min.....	78
C.3 EDS elemental analysis of BFO on STO thin films in HT conditions with deposition times of (a) 1 min, (b) 5 min, and (c) 30 min. ....	79
C.4 EDS elemental analysis of BFO on STO thin films in CAL conditions with deposition times of (a) 1 min, (b) 5 min, and (c) 30 min. ....	80

# CHAPTER I

## INTRODUCTION

### 1.1 Background and motivation

Resistivity of a material is used to compare the ability of different materials to conduct electric currents, e.g., the resistivity of insulators is higher than that of conductors. In addition, resistivity of materials depends on temperature, such as the resistivity of conductors typically increases as temperature rises, whereas the resistivity of semiconductors normally decreases as temperature rises (Lacy, 2010). The four-point probe technique is a typical way to measure electrical resistivity in bulk and thin-film materials (Schroder, 2015). This technique removes the effect of the resistance of a wire and contacts. Resistivity can be applied to many different applications, such as resistive sensors (thermal, light, and gas sensors) (Wu et al., 2020; Yu et al., 2009), resistive touch screens (displays of smartphones, tablets, and screen monitors) (Nam et al., 2021), and resistive switching devices next-generation memory, resistive random access memory (RRAM), and computing applications (Khan et al., 2021). The use of such materials is determined by the specific application. Therefore the development of materials, particularly multiferroic materials in various forms, including ceramic bulks, thin films, and nanostructures, has been extensively studied as materials in spintronics (Sando et al., 2013), magnetoelectrics (Bibes and Barthél my, 2008), and resistive sensors (Dziubaniuk et al., 2013). Multiferroic materials, which exhibit ferroelectrics and ferromagnets or antiferromagnets behaviors simultaneously, have attracted much attention due to their interesting physics and immense potential for multifunctional applications. The resistive switching phenomenon in multiferroic thin films is one of the interesting properties that is being intensively studied. This is a complicated phenomenon that influences from polarization states (Singh et al., 2021), point defects (Das and Kumar, 2021), and electron injection processes from electrodes (Andreeva et al., 2020). In addition, light illumination voltage pulses and white light can be used to control the resistive switching (Silva et al., 2016). This opens new

opportunities for energy-related and photoelectric devices.

Photoelectric devices or light sensors transform light energy (photons), whether visible or infrared light, into an electrical (electrons) signal. It can be divided into two types. First, the illumination creates electricity, such as photovoltaics or photoemissive devices. When a sufficient photon energy strikes photodevices, it causes free electrons to be released from sensitive substances. The photon energy is determined by the frequency of the incident light. As the frequency of light increases, the photon energy also increases. Therefore, more photon energy can be converted into more electrical energy too. Second, photoresistors or photoconductors change the electrical resistance when light illuminates to the device. Photoconductivity occurs when light strikes a semiconductor materials such as cadmium sulphide (CdS) and cadmium selenide (CdSe) (Acharya et al., 2010). A light-dependent resistor (LDR) is another name for a photoresistor. The resistance of a photoresistor decreases with increasing incident light intensity.

The oxide heterointerfaces have attracted a lot of attention due to their photoresistive properties. Aswin et al. measured photoconductivity on  $\text{LaAlO}_3$  (LAO) and  $\text{LaAlCrO}_3/\text{SrTiO}_3$  (STO) heterostructures and the persistent photoconductivity seen in these heterostructures might be due to charge separation (Aswin et al., 2016). Furthermore, the heterointerfaces also have an important phenomenon, namely the two-dimensional electron gas (2DEG). Ohtomo and Hwang discovered the 2DEG at the interface of the insulating oxides LAO and STO (Ohtomo and Hwang, 2004). This has been creating new principle in all-oxide electronics device with various interesting properties such as superconductivity (Wan et al., 2015), magnetoresistivity (Kormondy et al., 2018), negative electron compressibility (Riley et al., 2015) and ferroelectricity (Kim et al., 2013). The creation and control of 2DEG have been extensively studied via various effects such as a mechanical-bending-induced flexoelectricity (F. Zhang et al., 2020), a strain-induced ferroelectric polarization (Guo et al., 2016), and an intensive ultraviolet irradiation (Meevasana et al., 2011). The 2DEG states at the bare lightly 0.1% La-doped STO (001) surface have been previously reported after being exposed to ultraviolet synchrotron light probed by angle-resolved photoemission spectroscopy (ARPES) (Meevasana et al., 2011). The carrier densities can be controlled by the UV

irradiation dose due to the oxygen vacancy induction at the undoped STO (001) surface (Suwanwong, Eknapakul, et al., 2015). The formation of 2DEG has also been studied on  $\text{KTaO}_3$  (KTO),  $\text{BaTiO}_3$  (BTO) and (Ca, Zr)-doped BTO surfaces using the same methodology (Jaiban et al., 2020; King et al., 2012). The conducting interface and the carrier densities, which are associated with the surface conductivity, can be suited for nano-scale oxide and photoconductors devices (Jaiban et al., 2020; Masingboon et al., 2013; Suwanwong, Eknapakul, et al., 2015; Suwanwong, Kullapapinyokul, et al., 2015).

Recently, a 2DEG has been studied on the perovskite heterostructures  $\text{BiFeO}_3$  (BFO) on STO interfaces where the theoretical calculation indicates that a 2DEG exists at the  $(\text{BiO})^+$  and  $(\text{TiO}_2)^0$  interfaces (Z. Zhang et al., 2011). In terms of chemistry, the BFO/STO heterostructure is quite comparable to the LAO/STO one. However, BFO exhibits ferroelectric and antiferromagnetic properties simultaneously at room temperature (Catalan and Scott, 2009; Ederer and Spaldin, 2005; Lebeugle et al., 2007) while LAO does not have those. This helps to distinguish the BFO/STO from the LAO/STO structure. The creation of a 2DEG state on BFO/STO has demonstrated a metallic nature at the interface. The fluctuation in the valence state of the interfacial Ti atoms in STO causes the 2DEG and the Ti to diffuse into the Fe atoms of BFO at interfaces (Chen et al., 2015). The conducting interface can also be controlled by the ferroelectric polarization of a BFO/STO superlattice (Fu et al., 2021) and a BFO/ $\text{TbScO}_3$  (TSO) heterostructure (Y. Zhang et al., 2018). Under UV irradiation, the formation of an oxygen-vacancy-induced 2DEG state has been reported in the slightly doped metal  $\text{Bi}_{0.95}\text{La}_{0.05}\text{FeO}_3$  (BLFO) (Nathabumroong et al., 2020). The creation of 2DEG has required epitaxially BFO thin films so far. To do that, the BFO thin films have to be grown on the STO (100) substrates at a high substrate temperature (580-750 °C) (Ji et al., 2010; Nakashima et al., 2018; Nakashima et al., 2020; Saenrang et al., 2017). However, there are a few studies on amorphous oxides on STO substrate, that can create 2DEG via oxygen vacancy formation (Lee et al., 2012; Li et al., 2018; Scigaj et al., 2015).

In this work, we studied the photo-induced conductivity of a 2DEG at an amorphous BFO/STO interfaces. The conductivity of UV-irradiated STO and BFO/STO samples has been investigated. Furthermore, we demonstrate that conductivity can be controlled by an electric field. This research could pave the way for new

approaches to controlling the conductivity induced by UV irradiation and electric field in diode-like rectification applications.

## 1.2 Research objectives

1.2.1 To develop the RF magnetron sputtering system and deposit BFO thin films using our own system.

1.2.2 To prepare the BFO on STO substrate for studying the optical property, crystal structure, chemical composition, surface morphology, and thickness of BFO thin films.

1.2.3 To investigate the electrical properties of the Au/mBFO/STO thin films heterostructure under UV light exposure.

1.2.4 To understand the mechanism of the Au/mBFO/STO thin films heterostructure under UV light exposure.

## 1.3 Outline of thesis

To help you understand the overview of this dissertation, each chapter is described below. The thesis is divided into five main chapters. Chapter I is the introduction that includes the background and motivation, research objectives, and outline of the thesis. In chapter II, we describe the fundamental structure, preparation, and properties of BFO-based thin films. The effect of light irradiation on the BFO surface is explained by dynamic and non-dynamic mechanisms. In chapter III, the procedure of fabricating the BFO thin films heterostructure, including sample processing of the 3 configurations, e.g., Au/STO, Au/mBFO/STO, and Au/BFO/STO, is described. Moreover, the basic, conductance, and current-voltage characterizations used in this work are discussed. Chapter IV presents the experimental results and discussion, consisting of basic, conductance, and current-voltage characterizations, as well as mechanism and discussion. Finally, the conclusions and future research for this thesis are given in Chapter V.

## CHAPTER II

### LITERATURE REVIEWS

This chapter describes the fundamental structure, preparation, and properties of BiFeO<sub>3</sub> based thin films. The electrical conductivity on the surface of perovskite metal oxides is explained, such as the single crystals of SrTiO<sub>3</sub> and BiFeO<sub>3</sub>. The effect of light irradiation on the surface is also described with two mechanisms. The first is the dynamic mechanism. The electrical conductivity changes immediately when light is exposed to the surface of the materials. The dynamic mechanisms are related to photoconductivity, photoelectric, and ferroelectric photovoltaic effects. The second is the non-dynamic mechanism. The conductance still changes with the light exposure, but it remains at that value for some time after the light is turned off. The two-dimensional electron gases and oxygen vacancy are related to the non-dynamic process.

#### 2.1 Bismuth Ferrite (BiFeO<sub>3</sub>)

Bismuth ferrite (BiFeO<sub>3</sub> or BFO), is a multiferroic material that exhibits ferroelectric and antiferromagnetic properties simultaneously at room temperature (Catalan and Scott, 2009; Ederer and Spaldin, 2005; Lebeugle et al., 2007). The first study on BFO was started by Smolenskii in 1959, and it is a typical multiferroic material that has been extensively explored in recent years. However, the growth of a single phase BFO was challenging (Smolenskii et al., 1959). To overcome this problem, removing the secondary phases by treating the material with HNO<sub>3</sub> (nitric acid) was used to synthesize a single phase BFO (Achenbach et al., 1967; Michel et al., 1969). A few decades later, Kubel and Schmid were the first to investigate the monodomain single phase in 1990 by X-ray diffraction (Kubel and Schmid, 1990). Since the single-phase of BFO was synthesized, it manifests the intrinsic properties. In 2003, a large ferroelectric polarization of ~60 μC/cm<sup>2</sup> was demonstrated for the first time by BFO epitaxial thin films on an SrRuO<sub>3</sub> (SRO)/STO substrate (Wang et al., 2003). The films dis-

played a room-temperature spontaneous polarization higher than that of the bulk BFO ( $\sim 6.1 \mu\text{C}/\text{cm}^2$ ) (Teague et al., 1970) by 15 times. This was the first time which a high polarization in BFO thin films was used to create a new opportunity in memories and the next generation spintronic devices. Until recently, researches have focused on the synthesis and characterization of BFO in ceramic bulk, thin films, and nanostructure.

The structure of a single phase of BFO at room temperature was classified as rhombohedral distorted perovskite structure, belonging to the  $R3c$  space group (Moreau et al., 1971). The structure of the perovskite BFO is shown in Figure 2.1, which consists of a Bi ion at the corner positions, a transition Fe ion at the middle of the cubic, and the six oxygen ions at the face centers (Naganuma, 2011). The BFO in ceramic bulk exhibits ferroelectric properties below Curie temperature ( $T_C \approx 1103 \text{ K}$ ) and antiferromagnetic properties below Néel temperature ( $T_N \approx 643 \text{ K}$ ) (Sosnowska et al., 1982). The rhombohedral structure of perovskite BFO have lattice parameters of  $a=3.96 \text{ \AA}$  and a rhombohedral angle of  $\alpha=89.4^\circ$  at room temperature with ferroelectric polarization along the pseudocubic  $[111]$  direction (Catalan and Scott, 2009).

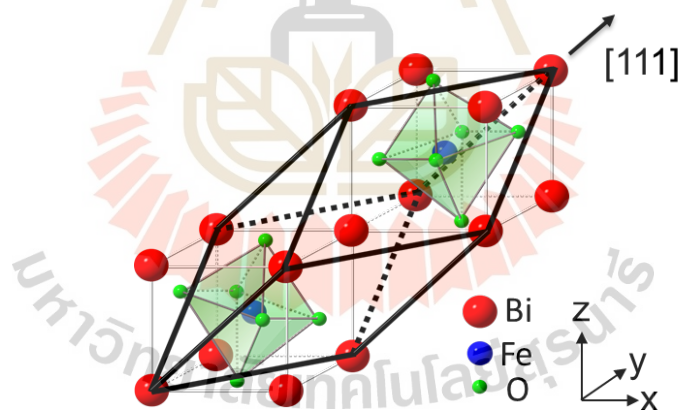


**Figure 2.1** A schematic of the rhombohedral structure of perovskite BFO ( $R3c$  space group) with two unit cells along  $[111]$  direction (Naganuma, 2011).

### 2.1.1 Preparation of Bismuth ferrite thin films

The RF magnetron sputtering technique has been widely used for depositing complex oxide thin films. Eom et al. were the first to deposit high-quality films over large areas with the RF magnetron sputtering technique (Eom et al., 1989). Normally, direct current (DC) magnetron sputtering technique is a method of coating

using metal targets such as gold (Au) (Ji et al., 2010), but it is not suitable for oxide materials as targets. The RF magnetron sputtering was operated with the alternating current (AC) to avoid a charge accumulation on the oxide sputtering target. The typical sputtering process is described as follows. The sputtering chamber is evacuated to reach a high vacuum ( $10^{-7}$  torr). Then, an inert gas (argon gas) was flowed into a vacuum chamber so that the pressure increases to  $10^{-3}$  Torr. The radio frequency voltage was applied between a substrate (anode) and a target (cathode). The power of the supply is increased slowly, and then the Ar gases are ionized into Ar ions ( $\text{Ar}^+$ ) and electrons.  $\text{Ar}^+$  gains energy that corresponds to the voltage between a substrate and a target. These ions are accelerated due to the electric field from applied voltage and bombard the target surface. The sputtered atoms were ejected into vapors and transported to the substrate. While the ionized electrons were trapped over the target by magnets that were placed behind the cathode in order to enhance the bombardment. The schematic diagram of the basic components of a magnetron sputtering system is shown in Figure 2.2.

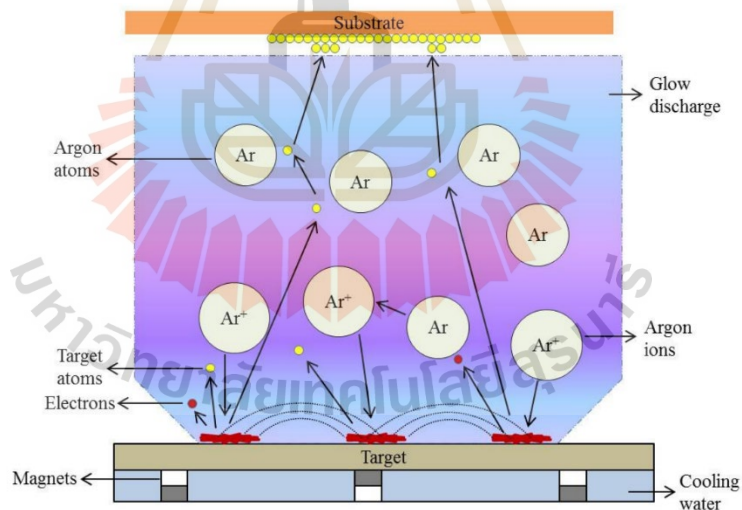


**Figure 2.2** The schematic diagram illustrating the basic components of a magnetron sputtering system (Maurya et al., 2014).

The BFO thin films can be prepared by several thin film deposition methods, including metal organic chemical vapor deposition (MOCVD) (Micard et al., 2020; S. Yang et al., 2010), pulsed-laser deposition (PLD) (Pei et al., 2020; You et al., 2018), electron beam (e-beam) evaporation (Mijiti et al., 2021; Y. Zhang et al., 2018),

spray pyrolysis (Kossar et al., 2021), chemical solution deposition (CSD) (B. Yang et al., 2021), the sol-gel method (Jiankang Li et al., 2020; Yin et al., 2010), and radio frequency (RF) magnetron sputtering (Ichinose et al., 2021). However, MOCVD and spray pyrolysis are normally used to grow films at a high temperature (800 °C) (Micard et al., 2020). Therefore, these techniques are not suitable for BFO thin films at low operating temperatures. The PLD and e-beam evaporation processes can grow only on a small area of substrate. So, these techniques are not suitable for making large-scale, homogeneous thin films. The CSD and sol-gel methods coat thin films on substrates at an ambient temperature, but thin films must crystallize at a high post-annealing temperature (700 °C) (B. Yang et al., 2021). So, for these reasons, the RF magnetron sputtering method is a simple process for growing high-quality thin films on large area substrates at low operating temperatures. This technique is favored for scaling up, and is highly compatible with the electronic industry (Y. Li et al., 2008; J. Wu and Wang, 2010; Zhu et al., 2018). The depositions of BFO thin films by RF magnetron sputtering were studied under various conditions as follows.

Ji et al. deposited epitaxial BFO thin films on vicinal STO (001) substrates by RF magnetron sputtering with the SRO as a bottom electrode. Before the deposition of BFO thin films, the STO substrate was cleaned with deionized water (DI) in an ultrasonic bath and etched in buffered oxide etchant. Finally, the STO samples were annealed in the air at 950 °C for 1 hour. The thin layer of SRO was first grown on the substrate. After that, the BFO thin films with a thickness of 170 nm were grown with an Ar:O<sub>2</sub> ratio of 7:1 at 5.8 mTorr and the RF power of 120 W. The substrate temperature was 680 °C. The XRD results revealed that the (001) BFO films were epitaxially grown on the (001) STO substrate (Ji et al., 2010).

Katiyar et al. prepared the BFO films with a thickness of 200 nm on SRO as a buffer layer on Pt/TiO<sub>2</sub>/SiO<sub>2</sub>/Si substrates by the RF magnetron sputtering technique. The growth condition was an Ar:O<sub>2</sub> ratio of 5:2 and kept the substrate temperature at 675 °C. The XRD results revealed that the BFO thin films have a polycrystalline rhombohedral phase (Katiyar et al., 2015).

Nakashima et al. used RF magnetron sputtering to deposit a 300-nm-thick of BFO thin films with a single-domain structure with no domain walls on STO

(111) and a vicinal angle of  $4^\circ$  on STO (001) substrates. The diameter of a 4" target, which was mixed between  $\text{Bi}_2\text{O}_3$  (99.99%) and  $\alpha\text{-Fe}_2\text{O}_3$  (99.99%), was used. The temperature of the substrate, the sputtering pressure, and the partial pressure of oxygen were all set at  $640^\circ\text{C}$ , 1.12 mTorr, and 3.75 mTorr, respectively. The XRD results revealed that the (001) and (111) oriented perovskite single-phase BFO thin films were formed on vicinal STO (001) and STO (111) substrates, respectively (Nakashima et al., 2015).

Gomez-Iriarte et al. grew BFO thin films on Si (100) substrates by RF magnetron sputtering. The BFO target manufactured by AJA International, Inc. was used. To eliminate the  $\text{SiO}_2$  layer and induce a hydrophobic surface, all substrates were treated with hydrofluoric acid. The base pressure, working pressure, and RF power were  $10^{-8}$  Torr,  $3 \times 10^{-3}$  Torr, and 35 W at a pure Ar atmosphere, respectively. BFO is usually deposited in an  $\text{O}_2$  atmosphere, while this work deposited the BFO in an atmosphere of  $\text{O}_2$  free. During deposition, the substrate temperature was kept constant at  $600^\circ\text{C}$ . The in situ annealing was performed at  $700^\circ\text{C}$  for 1 hour at the base pressure for pure BFO phase formation. The XRD results revealed that a R3cH polycrystalline BFO pure phase was observed without any secondary phase (Gomez-Iriarte et al., 2018).

Zhu et al. employed an off-axis RF magnetron sputtering technique to deposit the BFO thin films on the STO substrate (Zhu et al., 2018). The SRO was first grown on STO. The  $\text{Bi}_{1.05}\text{FeO}_3$  target was used. The 5% Bi excess in the target compensated for the loss of this volatile element during the deposition process. The base pressure and substrate temperature were set at  $1.5 \times 10^{-6}$  Torr and  $650^\circ\text{C}$ , respectively. After that, the BFO thin films were deposited on the SRO/STO substrate at an  $\text{Ar}:\text{O}_2$  ratio of 4:1 with a working pressure of  $1.0 \times 10^{-2}$  Torr and the RF power was 96 W. Finally, the systems were cooled to room temperature with the flow of pure oxygen. According to the XRD result, the BFO thin films were well crystallized into a single perovskite structure with (001)-oriented with no secondary phase (Zhu et al., 2018).

**Table 2.1** Summary of the RF magnetron sputtering conditions of BFO thin films.

Substrate	Working pressure (mTorr)	Ratio of Ar:O <sub>2</sub>	RF power (W)	Substrate temperature (°C)	Crystal structure	References
SRO/STO (001)	5.8	7:1	120	680	Epitaxial	(Ji et al., 2010)
SRO/Pt/TiO <sub>2</sub> /SiO <sub>2</sub> /Si	-	5.2	-	675	Polycrystalline	(Katiyar et al., 2015)
STO (111) and vicinal STO (001)	4.87	3.3:1	70	640	Monodomain	(Nakashima et al., 2015)
Si (100)	3	Pure Ar	35	600	Polycrystalline	(Gomez-Iriarte et al., 2018)
SRO/STO (001)	10	4:1	96	650	Single crystal	(Zhu et al., 2018)

### 2.1.2 Ferroelectric property in Bismuth ferrite thin films

Ferroelectric materials is the materials that exhibit a spontaneous electric polarization that switches polarization when exposed to an electric field (Lines and Glass, 2001). When perovskite oxide materials change the structural phase from the centrosymmetric cubic phase at a higher temperature to the low-symmetry phase below the transition temperature, also known as the Curie temperature, the ferroelectric phase occurs. The cation ions in oxide perovskite are moved relative to the arrangement of the anion ions via this mechanism. The result of this process produces the electric dipole moment, which is the cause of spontaneous polarization. Ceramic bulk BFO exhibits ferroelectric and antiferromagnetic properties at room temperature due to high Curie temperature ( $T_C \approx 1103$  K) and Néel temperature ( $T_N \approx 643$  K) (Sosnowska et al., 1982). In 2003, a large remanent polarization of  $\sim 60 \mu\text{C}/\text{cm}^2$  was demonstrated for the first time of 200-nm-thick epitaxial BFO thin films on an SRO/STO (001) substrate, as shown in Figure 2.3(a) (Wang et al., 2003). The films displayed a room-temperature spontaneous polarization higher than that of the bulk BFO ( $\sim 6.1 \mu\text{C}/\text{cm}^2$ ) (Teague et al., 1970). About a year later, the effects of substrate orientation on ferroelectric properties were studied. The pure phase of 200-nm-thick BFO thin films were grown on (001), (101) and (111) single crystal SRO/STO substrates. For each orientation, the hysteresis loops were found to have a remanent polarization

( $P_r$ ) of  $\sim 55$ ,  $\sim 80$ , and  $\sim 100 \mu\text{C}/\text{cm}^2$  for (001), (101), and (111) STO substrates, respectively. The BFO films grown on the (111) orientation have a single crystal with a rhombohedral structure, whereas films grown on the (101) or (001) orientations are monoclinically distorted from the rhombohedral structure due to the epitaxial constraint (Jiefang Li et al., 2004). Das et al. also grew 600-nm-thick BFO thin films on (001), (101) and (111) oriented STO substrates. The hysteresis loops were found to have a remanent polarization ( $P_r$ ) of  $\sim 55$ ,  $\sim 86$ , and  $\sim 98 \mu\text{C}/\text{cm}^2$  for (001), (101), and (111) STO substrates, respectively, as shown in Figure 2.3(b) (Das et al., 2006). Both works confirm that the direction of spontaneous polarization lies close to the (111) orientation, which is similar to the bulk crystals and ceramics.

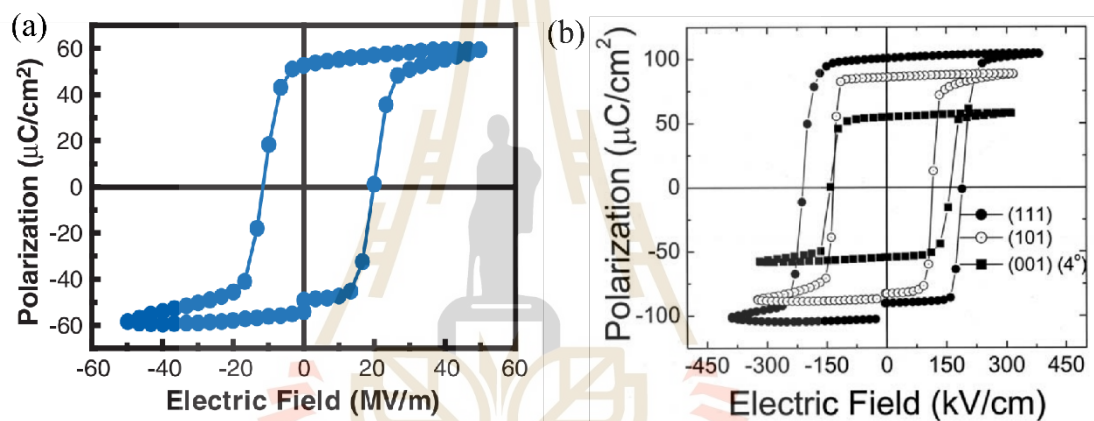


**Figure 2.3** The ferroelectric hysteresis loop of BFO/SRO/STO thin films (a) at a frequency of 15 kHz (Wang et al., 2003) and (b) at different orientation of (001), (101), and (111) BFO films (Das et al., 2006).

The pure phase of BFO thin films with different thicknesses of 190-600 nm were grown on SRO/Pt/TiO<sub>2</sub>/SiO<sub>2</sub>/Si (100) substrates by RF sputtering, which also exhibited a large polarization. The polarization shows  $\sim 80$ - $95 \mu\text{C}/\text{cm}^2$  with a mixture of (110) and (111) orientations at 1 kHz and room temperature as shown in Figure 2.4(a) (J. Wu et al., 2011). The highest spontaneous polarization occurs in the (111) direction for BFO thin films because the ions are displaced along the pseudocubic [111] direction from their equilibrium locations (Ederer and Spaldin, 2005). As a result, the combination of (110) and (111) orientations significantly improves the ferroelectric characteristics of BFO thin films. To date, the polarization of BFO thin films normally shows in epitaxial or polycrystalline thin films with a pure phase. However, there was

a study on amorphous BFO thin films on Pt/Ti/SiO<sub>2</sub>/Si substrate. The polarization value of thin films rises as the electric field increases, and the maximum polarization ( $P_m$ ) of amorphous BFO thin films was 25  $\mu\text{C}/\text{cm}^2$  at 1 kHz with applied electric field of 1705 kV/cm. At low electric fields, the P-E loops have a narrow shape and a small  $P_r$  value, as shown in Figure 2.4(b) (Z. Li et al., 2021).

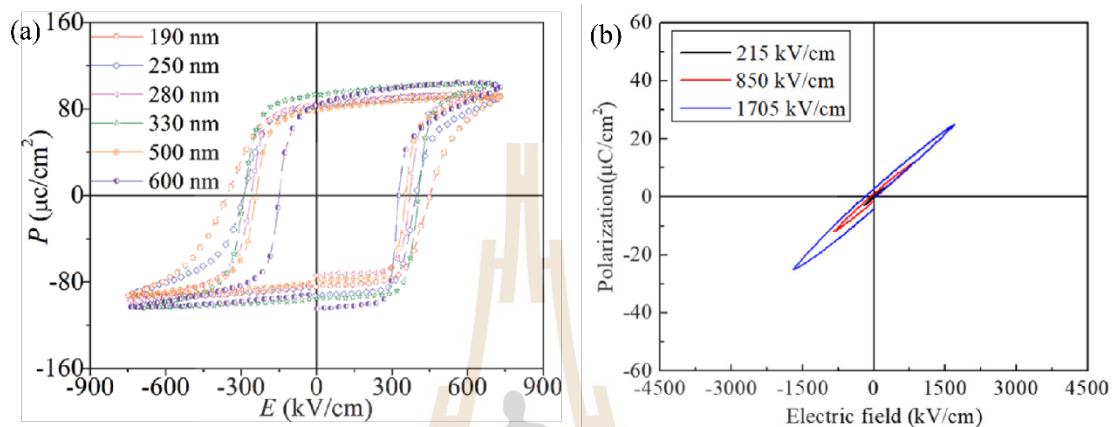


**Figure 2.4** The ferroelectric hysteresis loop at a frequency of 1 kHz (a) BFO thin films on SRO/Pt/TiO<sub>2</sub>/SiO<sub>2</sub>/Si substrate at different thicknesses of 190-600 nm (J. Wu et al., 2011) and (b) amorphous BFO thin films on Pt/Ti/SiO<sub>2</sub>/Si substrate with various applied electric fields (Z. Li et al., 2021).

## 2.2 Dynamic mechanism

### 2.2.1 Photoconductivity effect

Photoconductivity is an electrical phenomenon in which a material (semiconductors and some insulators) becomes more conductive after absorbing the electromagnetic radiation, e.g., visible, ultraviolet, and infrared lights, or gamma radiation. When the incident photons are absorbed on a material, the number of free electrons and holes rises, which it increases the material's electrical conductivity. The photons must have equal or greater energy than the band gap ( $E_g$ ) of the material to excite the electrons and produce this effect (Qiu et al., 2020). The relationship between the wavelength of radiation converts to photon energy ( $E$ ) are shown in equation 2.1.

$$E \text{ (eV)} = \frac{1,240}{\lambda \text{ (nm)}} \quad (2.1)$$

Where  $E$  is the photon energy and  $\lambda$  is the wavelength of the incident light. Figure 2.5 shows the schematic diagram of a bulk material with a cross section ( $A$ ) and length ( $L$ ). The material was connected to electrodes for applying voltage ( $V$ ) on positive (+) and negative (-) electrodes and was exposed to an incident electromagnetic radiation with wavelength ( $\lambda$ ), as shown in Figure 2.5 (Pollock, 2018). When the light was exposed on the surface, a voltage was created, corresponding to an electric field, allowing a current to flow through the material. A large number of electron-hole pairs will be created. Therefore, the change in electrical conductivity ( $\Delta\sigma$ ) can be expressed with the number of free electrons ( $\Delta n$ ) and holes ( $\Delta p$ ), as shown in equation 2.2.

$$\Delta\sigma = \Delta ne\mu_n + \Delta pe\mu_h \quad (2.2)$$

Where  $\mu_n$  is the mobility of the electrons,  $\mu_h$  is the mobility of the holes, and  $e$  is the elementary charge. Using Ohm's law,

$$V = IR \quad (2.3)$$

Where  $V$  is the applied voltage between the two electrodes and  $R$  is the electrical resistance which can be found as in equation 2.4.

$$R = \rho \frac{L}{A} \quad (2.4)$$

Where  $\rho$  is the electrical resistivity and the reciprocal of electrical conductivity ( $\rho = \frac{1}{\sigma}$ ),  $L$  is the length between the electrodes, and  $A$  is a cross section of the current path. Therefore, the photocurrent  $I_{ph}$  is shown as in equation 2.5.

$$I_{ph} = \frac{A}{L} \Delta\sigma V \quad (2.5)$$

A basic model of the photoconductivity of a bulk material with an applied voltage ( $V$ ), the cross section ( $A$ ), and length ( $L$ ) is shown in Figure 2.5.

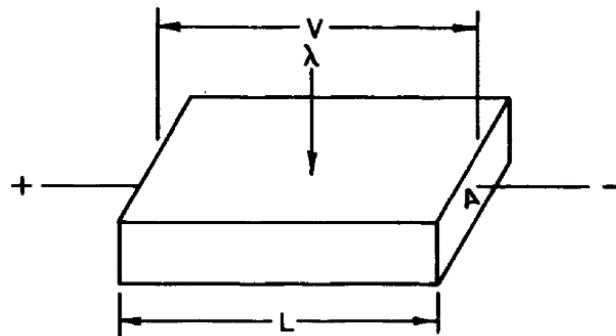


**Figure 2.5** The schematic diagram of a bulk material with a cross section of the current path ( $A$ ), the length between the electrodes ( $L$ ), and the applied voltage between the two electrodes ( $V$ ) with incident electromagnetic radiation ( $\lambda$ ) (Pollock, 2018).

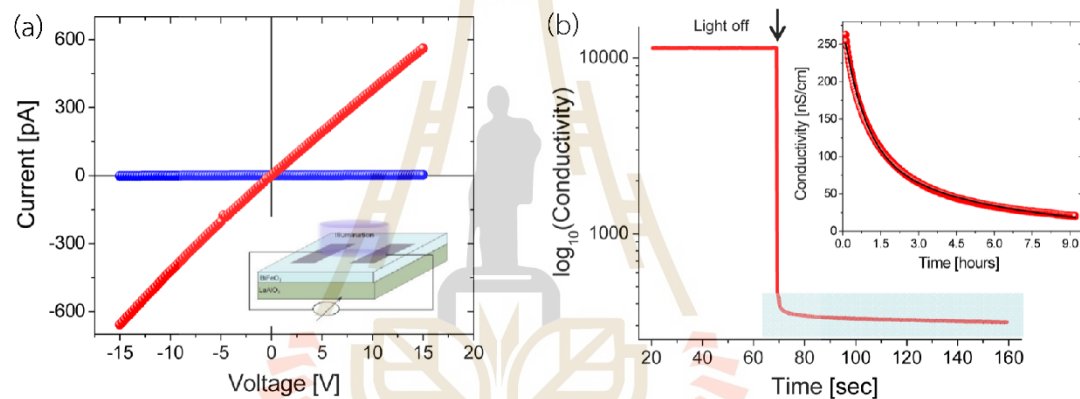


**Figure 2.6** (a) The I-V characteristics in the dark (blue) and during UV exposure (red) on BFO/LAO thin films and the schematic device geometry (insert), and (b) the conductivity as a function of time and the extended plot of the blue area as a gradual decay with the dark condition (insert figure) (Bhatnagar et al., 2014).

For example, the conductivity of 110 nm thick BFO films on  $\text{LaAlO}_3$  (LAO) was observed after the above-band gap light was exposed to the surface of the sample. Photoconductivity has been reported to be persistent (Bhatnagar et al., 2014). The current–voltage (I-V) characteristics of BFO/LAO before illumination were linear, with the current ranging within 1–2 pA, which corresponding conductivity is 0.85 nS/cm. After the UV light with photon energy above the band gap of BFO ( $h\nu = 3.06$  eV) was turned on, the photocurrent can be observed clearly with a conductivity of approximately 240 nS/cm. The photocurrent of the sample during UV exposure is almost 3 orders of magnitude higher than that of sample without UV exposure (Figure

2.6(a)). The conductivity as a function of time was shown in Figure 2.6(b). After UV exposure for 20 minutes, a logarithmic conductivity curve shows the abrupt decrease when the UV light is turned off. However, the decay time is very long from the high conductivity condition to the pristine conductivity value.

### 2.2.2 Photoelectric effect

The photoelectric effect is a phenomenon where electrons are emitted from the surface of a material when the material absorbs electromagnetic radiation. This process is also called photoemission, and the ejected electrons are called photoelectrons. The photoelectric effect was discovered in 1887 by Heinrich Hertz (Hertz, 1887). When ultraviolet light is irradiated on two metal electrodes with a voltage placed across them, Hertz discovered that the voltage between the electrodes change. This phenomenon indicates a light-matter interaction, that classical physics cannot explain, which characterizes light as an electromagnetic wave. In 1905, Einstein explained in quantum mechanics that each particle of light, or photon, contains a fixed amount of energy. The photon has energy ( $E = h\nu$ ), where  $\nu$  is frequency of light and  $h$  is Plank's constant. The work function ( $w$ ) is an intrinsic property of the metal that is the least amount of energy required to remove one electron from the surface of the bulk (solid) metal. When the photon energy that is larger than work function is exposed on surface of a material, the kinetic energy of an ejected electron ( $E_k$ ) is written as in equation 2.6.

$$E_k = h\nu - w \quad (2.6)$$

Where  $E_k$  is the kinetic energy of the ejected electron. In term of binding energy ( $E_b$ ) and work function ( $w$ ), the kinetic energy of the ejected electron can be written as in equation 2.7.

$$E_k = h\nu - E_b - W \quad (2.7)$$

From this equation, it can present with the binding energy as show equation 2.8.

$$E_b = h\nu - E_k - W \quad (2.8)$$

### 2.2.3 Ferroelectric photovoltaic effect

Ferroelectric materials have spontaneous polarization and can be switched by applying an external electric fields (Lines and Glass, 2001). These materials can also create electron-hole pairs that generate a steady state photocurrent by light, which is known as the photovoltaic effect. The ferroelectric photovoltaic (FEPV) effects have been seen in the ferroelectric materials and produce photovoltage and photocurrent in the polarization direction. The FEPV effects are distinct from regular photovoltaic devices in two aspects. First, in a conventional photovoltaic device, light absorption in a semiconductor creates electron-hole pairs, which are separated by an electric field in a micrometer-thick depletion region. The maximum voltage these devices can produce is equal to the semiconductor band gap ( $E_g$ ). On the contrary, the charge separation in ferroelectric materials is produced by spontaneous electric polarization. This produces a photovoltage that can be significantly greater than the band gap of ferroelectric materials, which is called an anomalous photovoltaic effect (S. Yang et al., 2010). Second, the direction of both photovoltage and photocurrent is switchable by changing the polarization direction (Choi et al., 2009). Therefore, ferroelectric materials can achieve a higher power conversion efficiency (PCE) than conventional solar cells. The schematic FEPV devices consisted of vertical and lateral structures are shown in Figure 2.7 (Yuan et al., 2014). The devices have two electrodes with an anode and a cathode. The electric dipole moment shows the polarization direction in ferroelectric materials. The photovoltage is determined by many factors, i.e., the distance between the two electrodes, light intensity, remnant polarization in the ferroelectric materials, crystal orientation, domain walls, and the ferroelectric/metal interface. Several mechanisms are proposed to explain the FEPV materials' better voltage output.

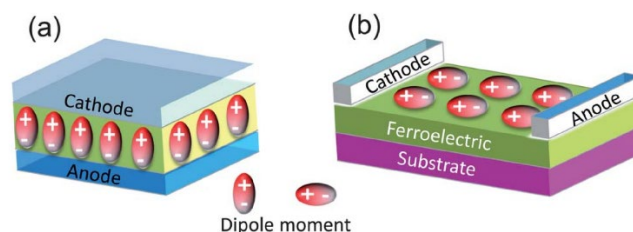


**Figure 2.7** The schematic diagram of ferroelectric photovoltaic device with (a) vertical and (b) lateral structures (Yuan et al., 2014).

Choi et al. reported a diode effect that has a nonlinear, unidirectional and high electric conduction in the BFO crystal. This was related to the direction of an electric polarization in the bulk. When the electric polarization is switched by an external electric field, the diode effect also flips. The system consists of thin platelike BFO crystal, with a thickness of  $\sim 90 \mu\text{m}$ , that has an in-plane dimension of  $\sim 1 \times 2 \text{ mm}^2$ , and a circular Ag electrode with a thickness of  $\sim 0.6 \text{ mm}$ , as shown in Figure 2.8(a). The forward and reverse bias directions are switched by large electric voltage pulses. When the Ag/BFO/Ag samples were biased with electric pulses of  $+150 \text{ V}$  ( $E \approx 17 \text{ kV cm}^{-1}$ ) on the top electrode, the ferroelectric polarization direction pointed down, as shown in the (piezoresponse force microscopy) PFM image in Figure 2.8(b). The electric current flowing through the sample is high and also in a downward direction. Therefore, the diode forward direction is from top to bottom, as shown in  $J(E)$  curve in Figure 2.8(c).

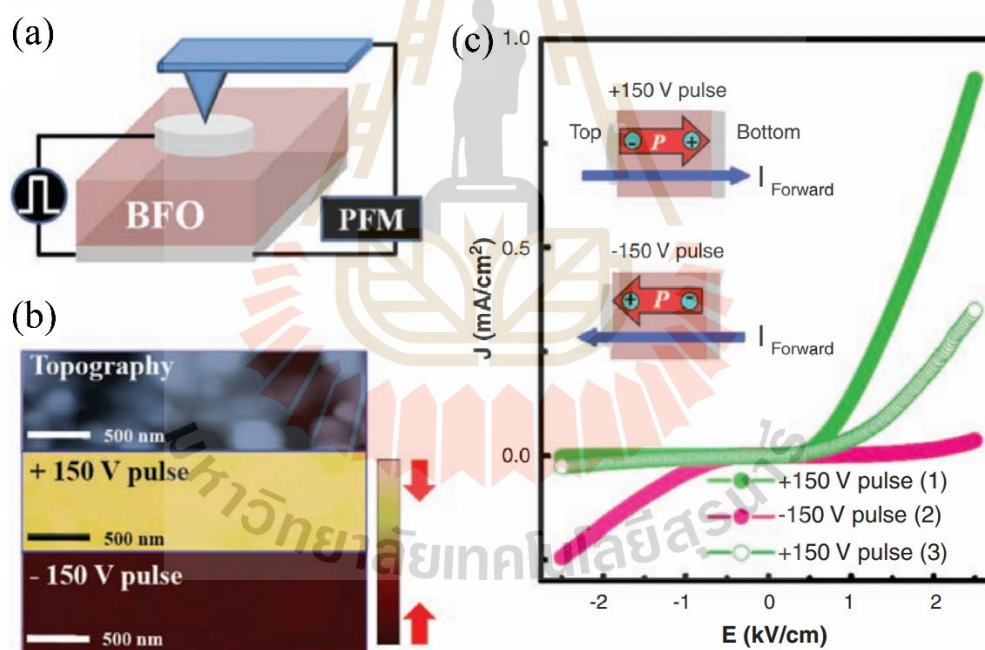


**Figure 2.8** (a) The schematic device geometry for PFM and current density  $J(E)$  measurements on Ag/BFO/Ag samples with electric pulses  $\pm 150 \text{ V}$  ( $E \approx 17 \text{ kV cm}^{-1}$ ). (b) The topography (top panel) and the out-of-plane PFM image with color-scaled after  $+150 \text{ V}$  pulse (middle panel) and  $-150 \text{ V}$  pulse (bottom panel). (c) The  $J(E)$  curves after the  $+150 \text{ V}$ ,  $-150 \text{ V}$ , and  $+150 \text{ V}$  pulses, respectively (Choi et al., 2009).

On the other hand, while the electric pulses of  $-150$  V were applied on top electrode, the ferroelectric polarization switched to the upward direction. Therefore, the diode forward direction changes from bottom to top (continuing along the polarization axis), which is called the reverse bias direction, as shown Figure 2.8(c) (pink line). After the  $+150$  V and  $-150$  V were done, the  $+150$  V pulses were applied again. However, the second application of  $+150$  V pulses does not entirely restore the original  $J(E)$  curve, which might be owing to complicated variables including partial polarization flipping or the development of conducting pathways (Choi et al., 2009).

S. Yang et al. discovered anomalous photovoltaic effects of single crystal of BFO thin films on DyScO<sub>3</sub> (DSO) substrate at an open-circuit voltage ( $V_{oc}$ ) of  $16$  V and a short-circuit current density ( $J_{sc}$ ) of  $\approx 1.2 \times 10^{-4}$  A cm<sup>-2</sup> measured perpendicular to the domain wall under white-light illumination. The I-V curves show a significant photocurrent with no photoinduced of  $V_{oc}$  measured parallel to the domain wall geometry, as shown in Figure 2.9. This photovoltage was when the domain walls are parallel to the electrodes, while it vanished when the electrode orientation and the domain walls are perpendicular to each other, as shown in Figure 2.9 (a and c) and (b and d), respectively.

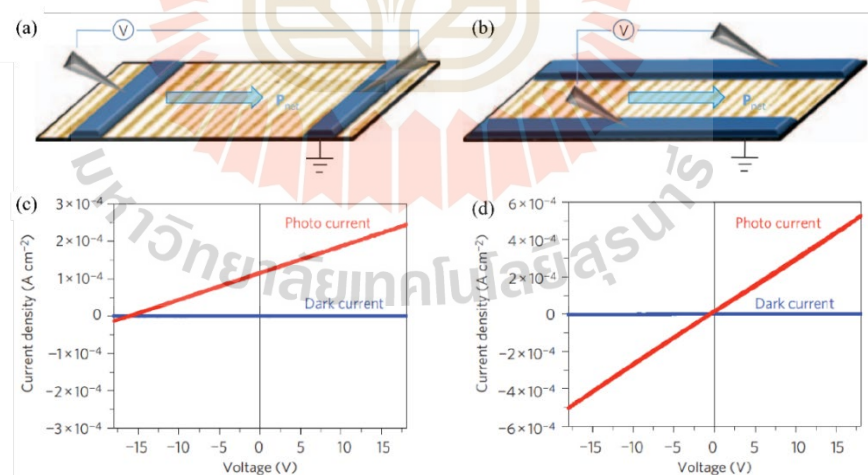


**Figure 2.9** The schematic diagram for I-V measurement with electrodes oriented (a) parallel and (b) perpendicular to the domain wall geometry. The I-V characteristics in the dark (blue) and after white-light exposure (red) on BFO/DSO thin films of the electrodes oriented (c) parallel and (d) perpendicular to the domain walls (S. Yang et al., 2010).

To demonstrate that the photovoltaic effect could be controlled by an electric field, voltage pulses of  $\pm 200$  V were applied to the planar of the two electrodes to switch polarization direction. The I-V characteristics of the sample a perpendicular with electrodes oriented to the domain walls for as-grown (black line) and after bias voltage pulses of  $\pm 200$  V (blue and red lines) were shown in Figure 2.10(a). It was consistent with Figure 2.9(d), that there is no observable photovoltaic response in this geometry for as-grown sample. The formation of an anomalous photovoltaic effect in this geometry occurs under light with +200 V (blue line). This corresponded to the PFM image then the domain walls rotated by  $90^\circ$  from that of as-grown state (Figure 2.10(b) (inset) top and middle panels). The in-plane and the net polarization directions for the entire device structure are shown by the thin arrows and big arrows, respectively. This result indicates that the domain configuration is essential to create the potential for the anomalous photovoltaic effect. In addition, I-V measurements with -200 V (red line) corresponds to the PFM image (Figure 2.10(b) (inset), bottom panels). This indicates that the photo-induced voltage and current can be switched by a change in the in-plane polarization direction of the BFO thin films.

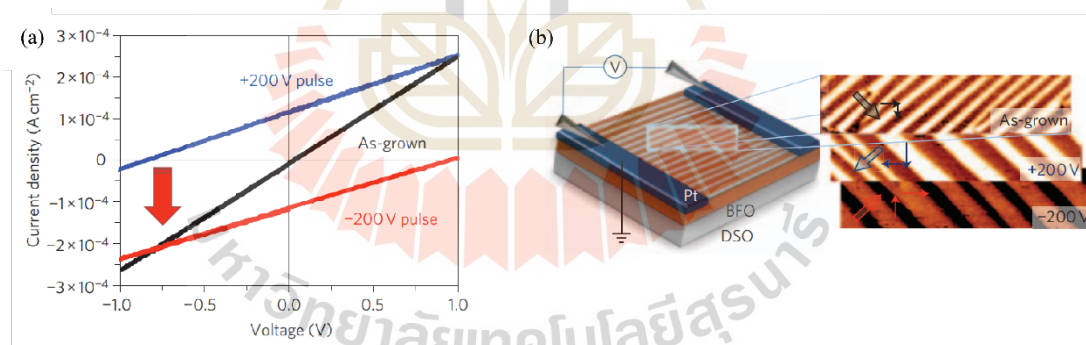


**Figure 2.10** (a) The I-V characteristics under white-light exposure on BFO/DSO thin films with electrodes oriented perpendicular to the domain wall for as-grown (black) and after bias a voltage pulses of  $\pm 200$  V (blue and red). (b) PFM images of the device structures as-grown (top panel), +200 V (middle panel), and -200 V (bottom panel) (S. Yang et al., 2010).

Yi et al. reported the direction of the FEPV current and a diode-like effect in BFO crystal can be reversibly switched by applying electric voltage pulses. The thin BFO crystal with Au as top and bottom electrodes was biased with a voltage

pulse of +210 V ( $E \approx 35 \text{ kV cm}^{-1}$ ) for 2 min, as shown in Figure 2.11(a). The downward ferroelectric direction occurs after applying a positive voltage. The I-V characteristics in the dark condition were observed as the forward bias direction (black open circles in Figure 2.11(a)). The green laser with a wavelength of 532 nm was exposed on the side of the sample, while top, and bottom surfaces were covered with black tape to prevent unwanted light illumination. After the light irradiation, the FEPV effect was observed in the forward bias direction with black solid circles. On the other hand, the upward polarization direction occurs with the application of voltage pulse of -210 V. The I-V curve shows the reverse direction in the dark and light irradiation, as shown in Figure 2.11(b) with black open and solid circles, respectively (Yi et al., 2011).

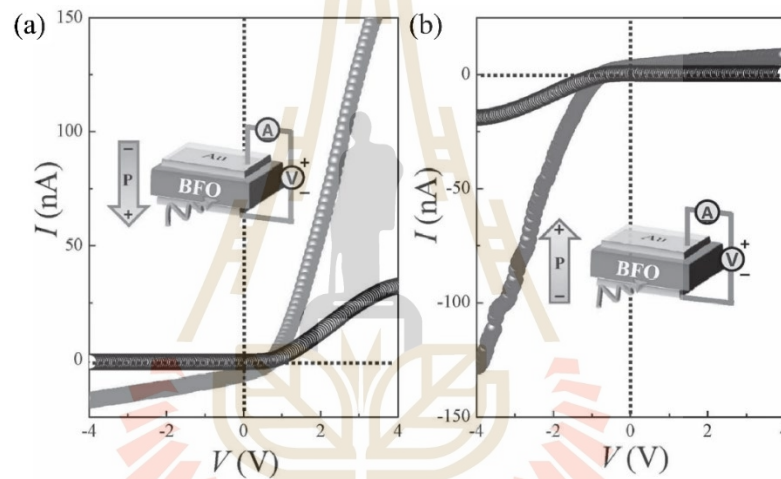


**Figure 2.11** The I-V characteristics in the dark (black open circles) and under green laser illumination (black solid circles) with (a) downward and (b) upward polarizations. The insets for (a) and (b) is the schematic device geometry with downward and upward polarization for I-V measurement, respectively (Yi et al., 2011).

## 2.3 Non-dynamic mechanism

### 2.3.1 Electronic structures of two-dimensional electron gases

A two-dimensional electron gas (2DEG) is a gas of free-moving electrons in two dimensions that forms on the interface of insulating materials, such as the interface of the insulating LAO and STO (Ohtomo and Hwang, 2004). Intensive UV irradiation has been used to study the formation and control of 2DEG (Meevasana et al., 2011). The 2DEG states at the bare lightly 0.1% La-doped STO (001) surface have

been previously reported after being exposed to ultraviolet synchrotron light probed by angle-resolved photoemission spectroscopy (ARPES). The 2DEG states of STO after exposure to synchrotron (UV) light are shown in the ARPES data of STO and the corresponding momentum distribution curves in the parabolic fits, as shown in Figure 2.12(a) and (b), respectively. The Fermi surface map from the ARPES data was observed in the two dispersions with the total surface charge density to be determined as  $7.1 \pm 2 \times 10^{13} \text{ cm}^{-2}$  (Figure 2.12(c)). This number is consistent with the 2DEG densities measured at LAO/STO surfaces (Kalabukhov et al., 2007). Figure 2.12(d) shows the schematic Fermi surface and band dispersions obtained from the measured electronic structure. These results show that the 2DEG could be created on the UV-irradiated STO surface (Meevasana et al., 2011).

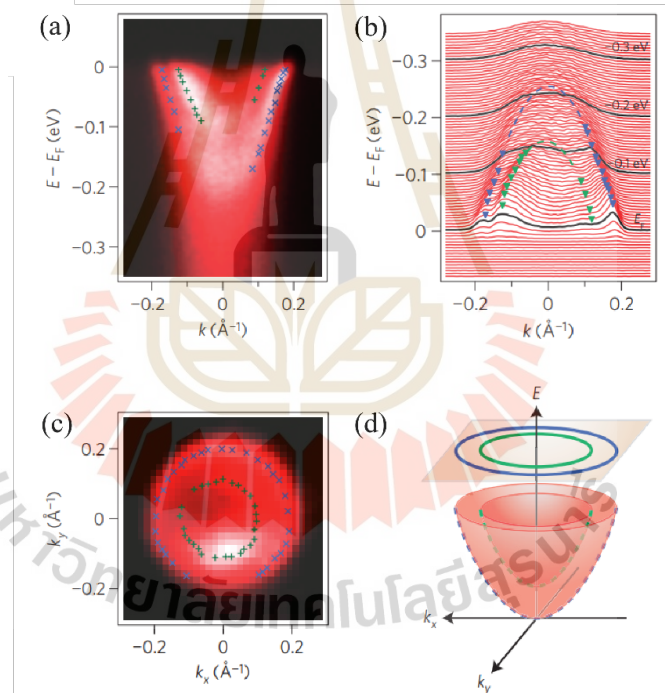


**Figure 2.12** The 2DEG states of the lightly 0.1% La-doped STO after exposure to synchrotron (UV) light. (a) ARPES data of La-doped STO at  $T = 20 \text{ K}$ , with corresponding momentum distribution curves in (b). (b) the parabolic fits to the data points from the ARPES data. (c) Fermi surface map from the ARPES data. (d) the schematic Fermi surface and band dispersions obtained from the measured electronic structure (Meevasana et al., 2011).

The undoped STO was also studied by the 2DEG during UV irradiation by ARPES, as shown in Figure 2.13(a) (Suwanwong, Eknapakul, et al., 2015). The 2DEG

state are extract of the surface density around  $9 \times 10^{13} \text{ cm}^{-2}$ . In comparison to a conventional semiconductor, this surface density has been high, showing that the insulating surface change is significant. To investigate the changes at the STO surface, the valence band of oxygen ( $O_{2p}$ ) peaks during the UV irradiation dose were measured. The  $O_{2p}$  peaks during UV irradiation dose becoming smaller, which is associated with the oxygen vacancy becoming larger, as shown in Figure 2.13(b). This result suggests that during irradiation, the oxygen vacancies are created, and the 2DEG state forms within the quantum well (Meevasana et al., 2011). This formation of 2DEG has also been studied on  $\text{KTaO}_3$  (KTO),  $\text{BaTiO}_3$  (BTO) and (Ca, Zr)-doped BTO surfaces using the same methodology (Jaiban et al., 2020; King et al., 2012). The conducting interface and the carrier densities, which are associated with the surface conductivity, can be suited for nano-scale oxide and photoconductors devices (Jaiban et al., 2020; Masingboon et al., 2013; Suwanwong, Eknapakul, et al., 2015; Suwanwong, Kullapapinyokul, et al., 2015).

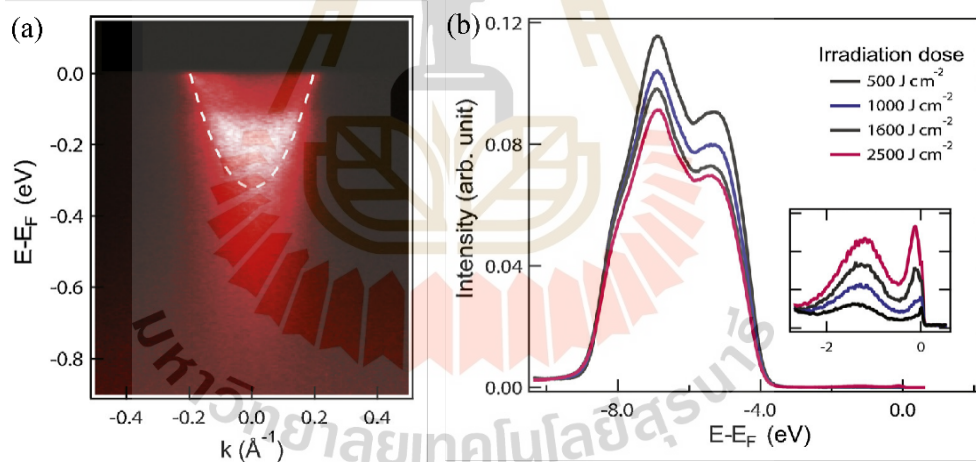


**Figure 2.13** The 2DEG states of the STO under exposure to synchrotron (UV) light. (b) The valence band of the oxygen state ( $O_{2p}$ ) and the oxygen-vacancy state as a function of UV irradiation dose (the zoomed-in graph is shown in the inset) (Suwanwong, Eknapakul, et al., 2015).

Recently, the 2DEG has been studied on the perovskite heterostructures  $\text{BiFeO}_3$  (BFO) on STO interfaces where the theoretical calculation indicates that the 2DEG exists at the  $(\text{BiO})^+$  and  $(\text{TiO}_2)^0$  interfaces (Z. Zhang et al., 2011). In terms of chemistry, the BFO/STO heterostructure is quite comparable to the LAO/STO one.

However, BFO exhibits ferroelectric and antiferromagnetic properties simultaneously at room temperature (Catalan and Scott, 2009; Ederer and Spaldin, 2005; Lebeugle et al., 2007) while LAO does not have those. This helps to distinguish the BFO/STO from the LAO/STO structure. A metallic nature with the creation of a 2DEG state on the BFO/STO interface has been demonstrated. To investigate the electrical characteristics of the interface, conductive atomic force microscopy (C-AFM) was examined on a cross-sectional sample with a thickness of 20  $\mu\text{m}$ . Figure 2.14 shows the surface topographic image and nanoscale current mapping of the cross-sectional BFO/STO interface. This demonstrated that the interface had a much higher current than its bulk elements. Therefore, the interface became conducting and the 2DEG developed at the interface. It is attributed to the difference in valence state caused by the Ti in STO diffusing into the Fe of BFO at interfaces (Chen et al., 2015).

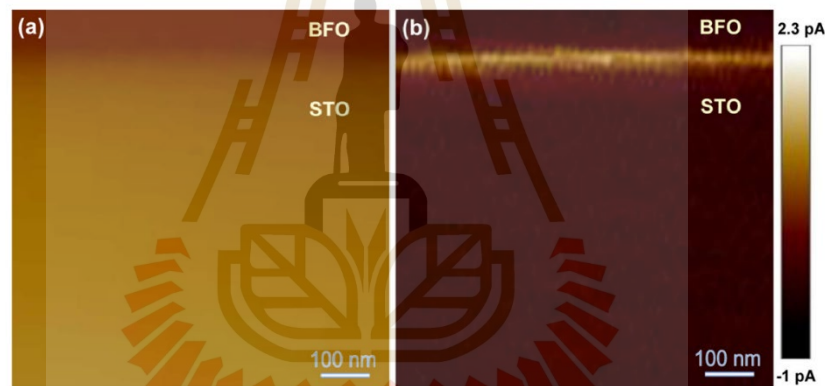


**Figure 2.14** The creation of 2DEG at the BFO/STO interface with (a) surface topographic image and (b) nanoscale current mapping (Chen et al., 2015).

The conducting interface can be controlled by the ferroelectric polarization of a BFO/STO superlattice (Fu et al., 2021) and a BFO/TbScO<sub>3</sub> (TSO) heterostructure (Y. Zhang et al., 2018). Under UV irradiation, the formation of an oxygen-vacancy-induced 2DEG state has been reported in the slightly doped metal Bi<sub>0.95</sub>La<sub>0.05</sub>FeO<sub>3</sub> (BLFO) (Nathabumroong et al., 2020). The creation of 2DEG has required epitaxially BFO thin films so far. To do that, the BFO thin films have to be grown on the STO (100) substrates at a high substrate temperature (580-750 °C) (Ji et al., 2010; Nakashima et al., 2018; Nakashima et al., 2020; Saenrang et al., 2017). However, there

are a few studies on amorphous oxides on STO substrate, that can create 2DEG via oxygen vacancy formation (Lee et al., 2012; C. Li et al., 2018; Scigaj et al., 2015).

### 2.3.2 Effects of oxygen vacancy

Oxygen vacancies are the most prevalent defect property in some metal oxides, which are important phenomena related to electrical conductivity (Tanaka et al., 2002). In the band structure of metal oxide, light exposure on the material surface can produce an oxygen vacancy state between the valence and conduction bands. Suwanwong et al. showed that the single crystal of STO on the (100) occurred in the 2DEG states at the UV-irradiated STO surface. UV irradiation on STO can create an oxygen vacancy and can change resistance (Suwanwong, Eknapakul, et al., 2015). These 2DEG states are attributed in part to the surface's conductivity. Therefore, a resistivity measurement was set up as shown in the inset of Figure 2.15(a). The gold electrodes were coated on the surfaces of these STO crystals with a interdigitated pattern. The experiment was set up to measure resistance. The resistance of the STO sample at a pressure of  $2 \times 10^{-8}$  mbar was roughly  $4 \text{ G}\Omega$  before UV irradiation. When the UV was on, the oxygen-vacancy-induced 2DEG state, the resistance decreased quickly to below  $10 \text{ M}\Omega$ . However, when the UV was off, the resistance would increase back to the initial state, but at a slower rate because of the 2DEG on the STO surface. The 2DEG happens over a significantly longer time period as in the ARPES data above (Figure 2.13). Jaiban et al. also measured the conductance under UV in at wavelength of 405 nm on STO. The UV was shone between two gold electrodes that were 2 mm apart (see Figure 2.15(b)). The conductances in the off states, whose contribution is mostly from the slow-changing 2DEG states, grow along the dash lines when the exposure period is increased. This result quantitatively agrees with the trends of increases in surface carrier densities found in ARPES data (Jaiban et al., 2020). This plays a major role in the resistance (conductance) changes found here.

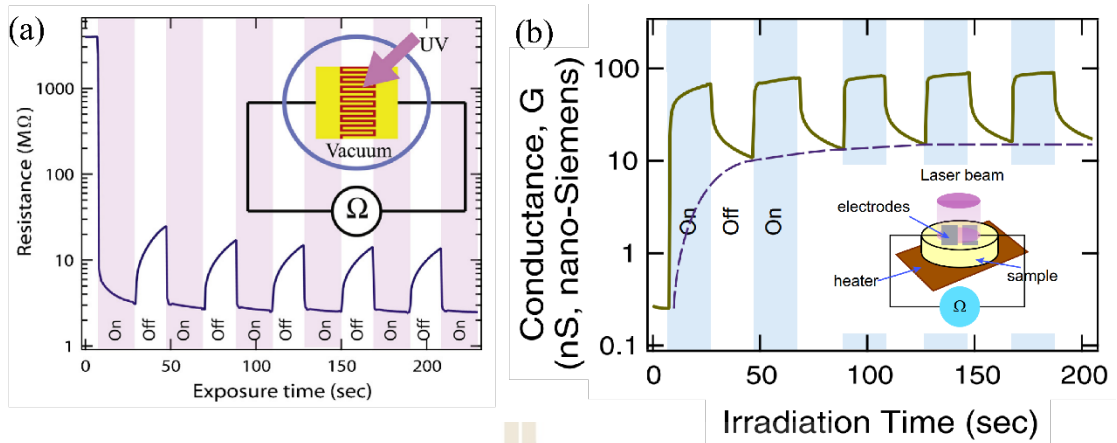


**Figure 2.15** The measured resistance (conductance) of the STO surface where the on-off UV irradiation process and the schematic diagram of the measurement setup (inset figure) (a) Suwanwong et al. (Suwanwong, Eknapakul, et al., 2015) and (b) Jaiban et al. (Jaiban et al., 2020), respectively.

## CHAPTER III

### THIN FILMS PREPARATION AND CHARACTERIZATION

In this chapter, section 3.1 explains the procedure of fabricating the BFO thin films heterostructure, including sample processing of the 3 configurations, e.g., Au/STO, Au/mBFO/STO, and Au/BFO/STO. In section 3.2 and 3.3, the measurement systems used in this work are discussed.

#### 3.1 Thin film deposition and sample processing

##### 3.1.1 BiFeO<sub>3</sub> thin films deposition by RF magnetron sputtering

In this thesis, we prepared BFO thin films on STO (100) using an RF magnetron sputtering system. A two-inch-diameter BFO target was used (Kurt J. Lesker Company, USA). The STO samples (Crystalbase, Japan) were used as the substrate. The BFO thin films were deposited on STO (100) substrates using RF magnetron sputtering with 3 different conditions as follows:

1. at room temperature (RT),
2. at room temperature, then calcination at 600 °C for 2 hours (CAL) in air,
3. at high temperature 600 °C (HT).

The other growth parameters were 100 W, 6.0 mTorr, and 4:1 for RF power, working pressure, and Ar:O<sub>2</sub> ratio, respectively. The films thicknesses were varied with deposition time, which was 1, 5, and 30 minutes.

In this thesis, the BFO thin films with RT conditions were the main sample to study the conductance of the heterostructure in 3 configurations and the effect of biasing high voltage. While the CAL and HT conditions were compared to the conductance with the RT condition, only the Au/BFO/STO configuration was tested.

### 3.1.2 Fabrication of Au top electrode

The STO substrates were cleaned with acetone, ethanol, and deionized water (DI water) using ultrasonic cleaners for 10 minutes, respectively. Then, these substrates were dried with nitrogen gas. In this thesis, there are 3 sample configurations. The schematic diagrams of the planar electrode in Figure 3.1(a), (b), and (c) show the 3 configurations mentioned earlier and will be devoted as Au/STO, Au/mBFO/STO (m stands for masked), and Au/BFO/STO, respectively. However, to prepare the Au electrode, we used the same procedure as follows. We prepared 65-nm-thick films of Au with a rectangular shaped on each configuration using a direct current (DC) sputtering system (GSL-1100X-SPC-12 Compact Plasma Sputtering Coater by MTI Inc.). We used a shadow mask to put on top of the substrate before depositing and creating the Au pattern electrodes. The sputtering current, the deposition time, and the pressure were 10 mA, 5 minutes, and 56 mTorr, respectively. The width, length, and interspacing of the planar electrodes are 350, 850, and 120  $\mu\text{m}$ , respectively. For the Au/mBFO/STO configuration, we also used a shadow mask to put on top of the Au/STO configuration before depositing and creating the BFO thin films pattern, as shown in Figure 3.1(b).

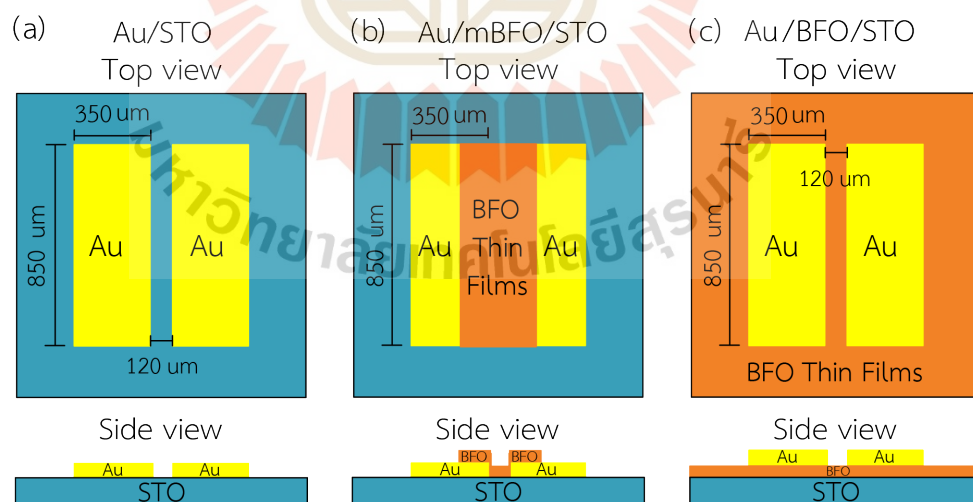


**Figure 3.1** The schematic diagram of the planar electrode of (a) Au/STO, (b) Au/mBFO/STO, and (c) Au/BFO/STO.

## 3.2 Basic characterization

### 3.2.1 X-ray diffraction (XRD)

X-ray diffraction (XRD) is a technique used to study the crystalline structure and identify phases. This technique distinguishes between amorphous and crystalline materials based on physical properties. The principle of X-ray diffraction is based on the constructive interference of monochromatic X-rays and a crystalline sample. A cathode tube generates X-rays, which are filtered to create monochromatic X-rays. It is collimated to concentrate and pointed towards the sample. When the x-ray beam hits a sample surface, which represents the wave input, the sample produces a scattered beam, which is the wave output, as shown in Figure 3.2. The interaction of the incident rays with the sample produces constructive interference, which is the identification of the difference between the structures of materials. The Bragg's law equation explains these phenomena, as shown in equation 3.1.

$$n\lambda = 2d\sin\theta \quad (3.1)$$

Where  $n$  is the order of diffraction,  $\lambda$  is the wavelength of the incident beam,  $d$  is the lattice spacing, and  $\theta$  is the angle of the diffracted beam in degree.

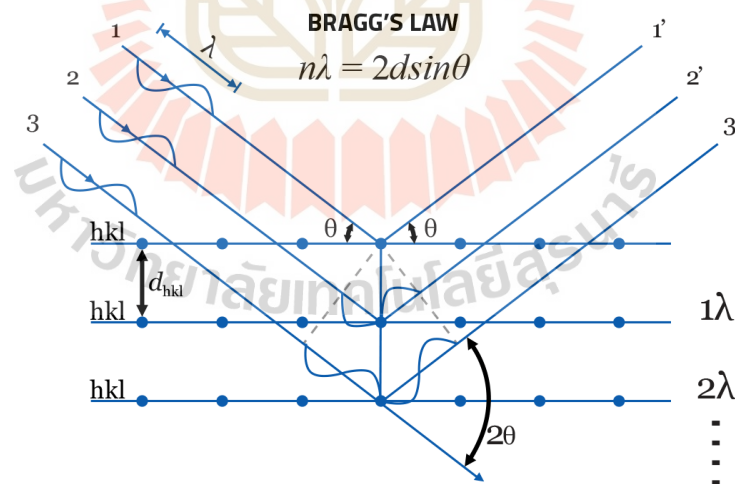


**Figure 3.2** The x-ray diffraction principle (<https://www.veqter.co.uk/residual-stress-measurement/x-ray-diffraction>).

In this thesis, the XRD was used to study the effect of the crystallinity on 3 different BFO thin films conditions. The phase and crystal structure were characterized by the XRD D8 Advance Bruker with Cu  $K\alpha$  radiation ( $\lambda = 1.54056 \text{ \AA}$ , 40 kV, 40 mA). The step size of  $0.02^\circ$  and step time of 0.2 s were used to record the XRD patterns in the  $2\theta$  range of  $15^\circ$  to  $80^\circ$ . The crystalline material was identified by comparison of the XRD pattern with the Joint Committee for Powder Diffraction Standards (JCPDS).

### 3.2.2 Atomic force microscope (AFM)

The atomic force microscope (AFM) is the most powerful microscopy technique for investigating nanoscale samples surface. It provides a three-dimensional topography image with high resolution up to an angstrom scale. The principle of AFM is used a cantilever as a probe tip to scan over a sample surface which consists of contact and non-contact mode. While the tip scans along the surface, the laser beam is detected the motion of cantilever by reflection an incident beam to the position-sensitive photo diode (PSPD) or photo detector. The feedback loop controls the height of the tip above the surface, as shown in Figure 3.3. Therefore, the AFM can build an accurate topographic map of the sample surface.

In this work, the AFM was used to identify the growth rate of BFO thin films and to examine the surface morphology of the as-grown BFO films.

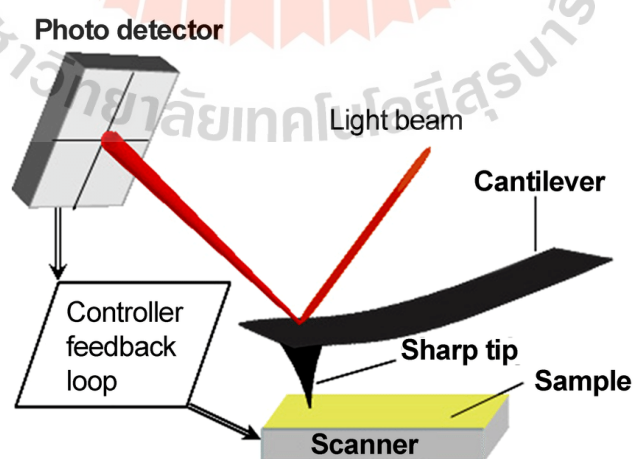


**Figure 3.3** Basic principle of atomic force microscopy (Pletikapić and Ivošević DeNardis, 2017).

### 3.2.3 Field emission scanning electron microscope (FESEM)

Field emission scanning electron microscope (FESEM) is used to investigate the surface morphology of material. It provides topography, particle sizes, and shapes at high magnifications of 10x to 300,000x more than scanning electron microscopy (SEM). The principle of FESEM has a field-emission cathode in the electron gun to provide the narrow electron beams with high electron energy. It can improve the resolution of up to a nanometers scale and decrease the electrical charging of samples. After the electron beam (primary electrons) impacts on the sample surface, the electron will interact with electrons on the sample surface to produce secondary electrons (inelastic interactions), which will be detected by the secondary electron detector. While the backscattered electrons are detected from the reflected electrons (elastic interactions), which will be detected by the backscattered electron detector. The two detectors convert these electrons to the electrical signal and process by computer, as shown in Figure 3.4.

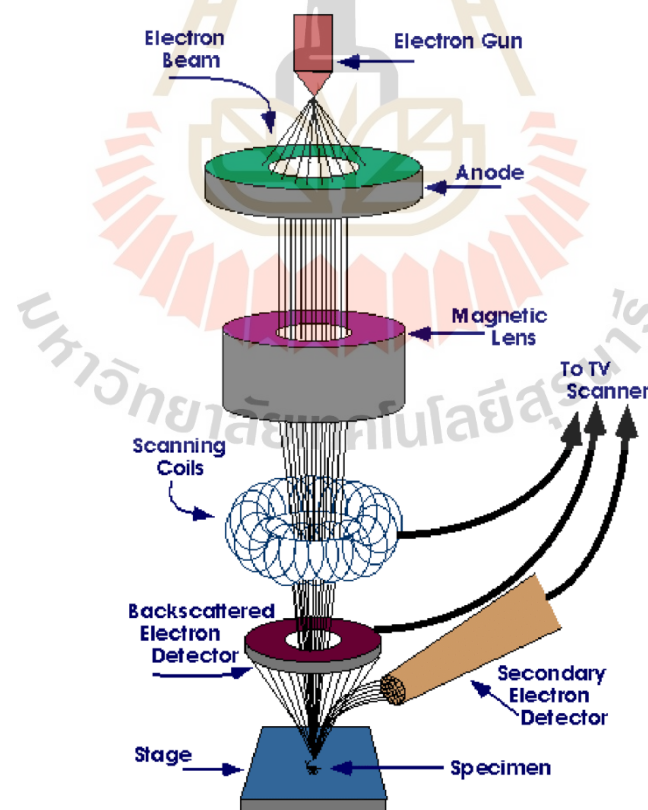


**Figure 3.4** The field emission scanning electron microscope (FESEM) principle (Billah, 2016).

In this thesis, the samples were placed onto stubs by using carbon tape and were coated with carbon in a vacuum for 20 nm. The sample must have conductivity to prevent charging. Therefore, coating the sample with carbon is necessary. The FESEM, JEOL JEM. 7800X, was used to investigate the morphology of BFO thin films.

#### **3.2.4 Energy dispersive X-ray spectroscopy (EDS)**

The energy dispersive X-ray spectroscopy (EDS) is used to analyse the chemical composition, quantity, and distribution of the elemental composition. The principle of EDS requires the appropriate high energy electrons to hit the electrons of a sample in ground state. These electrons at the core level receive high energy until the ejection of an atom. After that, an electron from a higher binding energy electron level falls into the core hole. It emits an X-ray with the energy of the difference between the electron level binding energies. The X-ray has a specific value for each element. Therefore, the energy of X-rays is investigated by EDS for determining elemental composition. In addition, the element analysis can set the area of interest and create the elemental mapping of the sample.

In this thesis, the EDS was used to analyze the chemical composition quantity and distribution of the Bi, Fe, and O compositions of the 3 different BFO thin films conditions. The EDS technique is measured after the FESEM technique on the same device.

#### **3.2.5 Ultraviolet visible spectroscopy (UV-VIS)**

Ultraviolet visible spectroscopy, or UV-VIS, is a technique that compares the quantity of UV or visible light absorbed or transmitted through a sample and a reference sample. The UV wavelengths of the spectrum range from 190 to 380 nm, while the visible light range is from 380 to 740 nm. The absorption and transmission are controlled by sample composition and electronic transitions within the molecule. The principle of the UV-VIS technique is to use light to irradiate the sample. Some atoms in the molecule will absorb light at various wavelengths depending on their chemical bonds and crystalline structure. The specific energy of light excited the electrons in the sample to the higher energy state. Electrons in the different chemical

bonds need the specific energy of light to excite the electrons to the higher energy state. Therefore, the absorption of light happens at the different wavelengths in different samples. A schematic of the main components in a UV-Vis spectrophotometer is shown in Figure 3.5. The optical band gap ( $E_g$ ) of the BFO thin film is calculated using the Tauc equation as described in equation 3.2.

$$(\alpha h\nu)^n = A(h\nu - E_g) \quad (3.2)$$

Where  $\alpha$  is the absorbance coefficient,  $n = 0.5$  for indirect band gap and  $n = 2$  for direct band gap materials,  $A$  is constant,  $h\nu$  is the photon energy with  $h$  is Plank's constant and  $\nu$  is the frequency of incident light.  $E_g$  is the optical band gap (Jubu et al., 2020). According to the direct band gap of the BFO thin films, the optical band gap is extrapolated by linear fitting of the plots between  $(\alpha h\nu)^2$  versus  $h\nu$ . Therefore,  $E_g$  values were determined using the linear extrapolation part of the plots to  $(\alpha h\nu)^2 = 0$ .

In this thesis, the absorption spectra were used to recording at room temperature by using the UV-Vis spectrophotometer (Specord 250 plus, Analytik Jena,  $\lambda=190-900$  nm, Germany). The transmission of BFO films was studied at a monochromatic light wavelength of 405 nm using Ocean Optics HR4000 high-resolution spectrometer.

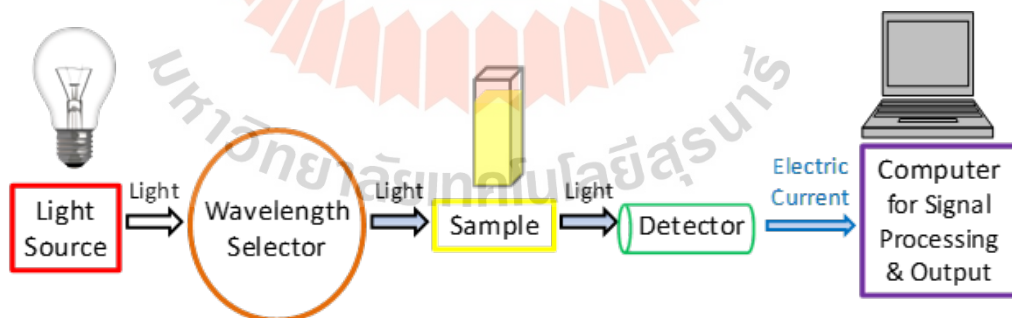


**Figure 3.5** A schematic of the main components in a UV-Vis spectrophotometer (<https://www.technologynetworks.com/analysis/articles/uv-vis-spectroscopy-principle-strengths-and-limitations-and-applications-349865>).

### 3.3 Conductance characterization

#### 3.3.1 Principle of 2-wire sensing

The 2-wire resistance measurement is extensively used to determine the sample's electrical conductance. It is developed from the four-point probe technique. Typically, the four-point probe technique is used to measure the electrical resistivity in bulk and thin-film materials. This technique removes the effect of the resistance of a wire and contacts. The 4-point probe technique is suitable for a low resistance sample, but it is inaccurate for a high resistance sample. However, the 2-wire resistance measurement is good for samples with a high resistance. Because the resistance of the sample is much greater than that of the wire, we may neglect the resistance of the wires in the circuit.

In this thesis, the 2-wire resistance measurement is used to measure the 3 configurations of electrical conductance, e.g., Au/STO, Au/mBFO/STO, and Au/BFO/STO. The schematic diagram of the 2-wire resistance measurement is shown in Figure 3.6. The resistance of the sample follows Ohm's law equation 3.3.

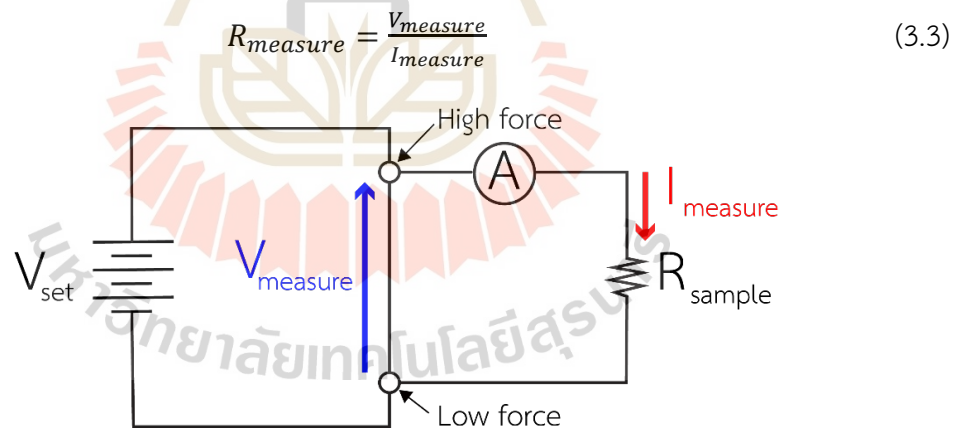


**Figure 3.6** The schematic diagram of resistance measuring circuit of 2-wire system.

#### 3.3.2 Conductance measurement

The conductance was measured using a precision source meter (Agilent B2901A) with/without an illuminating collimated ultraviolet laser at wavelength 405 nm ( $h\nu = 3.06$  eV with intensity  $\sim 12.45$  mW/cm<sup>2</sup>). An optical power meter was used to measure the UV light intensity (Thorlabs model PM100D). The illuminated region was a 0.15 mm radius circle that was set in the middle between Au electrodes. The voltage

was applied between Au electrodes in constant voltage mode at 5 V. In this thesis, there are 3 configurations of the heterostructure as follows: Au/STO, Au/mBFO/STO, and Au/BFO/STO. The details of the conductance measurement of each configuration are shown in section 3.3.3.

### 3.3.3 Sample configurations

#### 3.3.3.1 Au/STO configuration

The Au/STO configuration was used as a reference sample for the conductance measurement compared to samples with BFO films. The schematic device geometry for conductance measurements of the Au/STO configuration was shown in Figure 3.7.

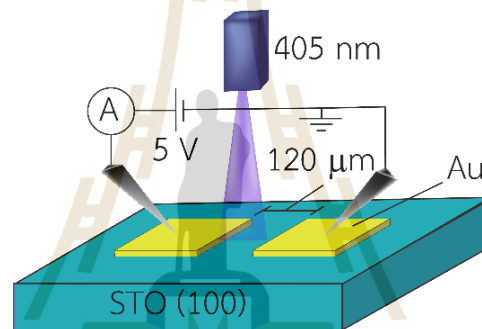


**Figure 3.7** The schematic device geometry for conductance measurements of the Au/STO configuration.

#### 3.3.3.2 Au/mBFO/STO configuration

The Au/mBFO/STO configuration was used to study the conductance at interface. The conductance is generated by both the BFO thin films and the STO substrate. The BFO thin films in this configuration are deposited at room temperature with deposition time of 1, 5, and 30 minutes. Because this configuration must deposit the Au electrode on the STO substrate before depositing BFO thin films, the CAL and HT conditions are not suitable for this configuration. The high temperature at 600 °C destroys the Au electrode, making it non-conductive. Figure 3.8(a) shows the device geometry (top right) of the STO and Au/mBFO/STO configurations with Au electrodes, while the optical surface image and the zoomed in area are presented at the top left and the bottom of the figure, respectively. The schematic device geometry for conductance measurements is shown in Figure 3.8(b).

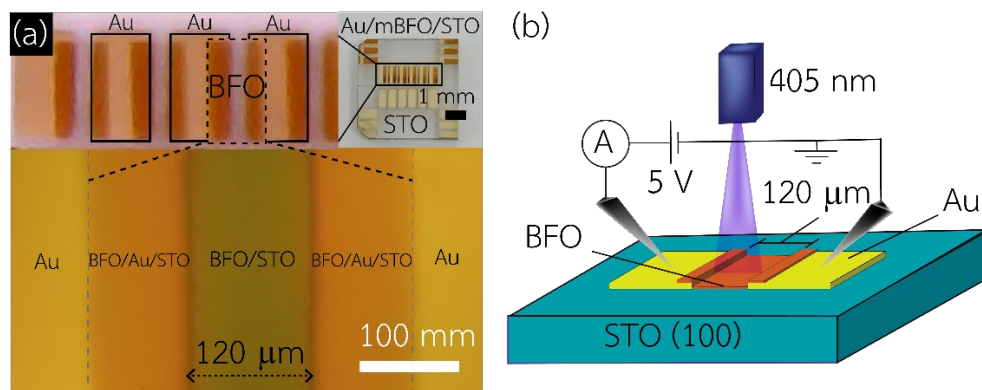


**Figure 3.8** (a) The device geometry (top right) of STO crystal and Au/mBFO/STO configuration with Au electrodes. The optical surface image (top left) and surface morphology (bottom) and (b) the schematic device geometry for conductance measurements of Au/mBFO/STO configuration.

To demonstrate how to control the conductance of Au/mBFO/STO configuration (at the BFO/STO interface) with deposition time of 1 minute, we applied electric fields across this interface, as shown in Figure 3.9. We applied a voltage of  $\pm 1.75$  kV ( $E \sim 67$  kV/cm) for 5 minutes between the top and bottom electrodes and then measured conductance. The bias high voltage direction was defined as positive if a positive bias voltage was applied to the top electrode and the bottom electrode was grounded. While the negative means that the negative bias voltage was applied to the top with the bottom electrode grounded.

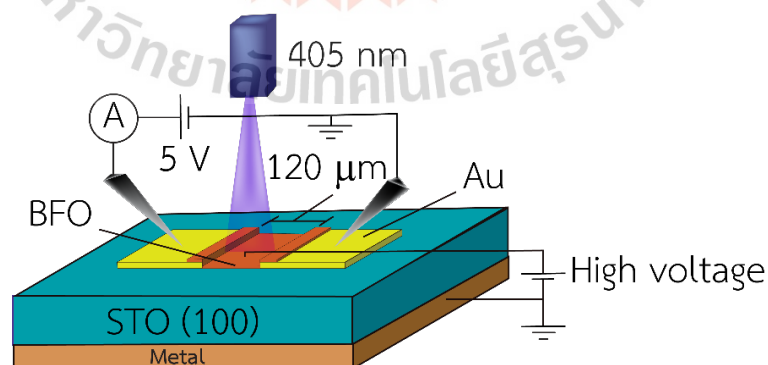


**Figure 3.9** The schematic device geometry for conductance measurements of Au/mBFO/STO configuration with applying high voltage on the top and bottom electrodes.

### 3.3.3.3 Au/BFO/STO configuration

The conductance of the Au/BFO/STO configuration was set up in a schematic device geometry as shown in Figure 3.10. This configuration was studied with a deposition time of 1 minute for two features. First, the conductance was compared with the Au/mBFO/STO configuration. Second, the effect of the crystallinity of BFO films on conductance was studied under 3 different conditions, e.g., RT, CAL, and HT with multiple UV light exposures.

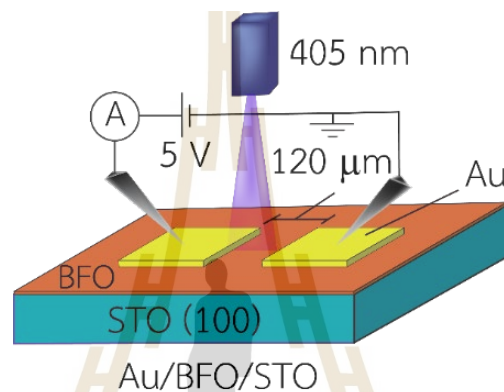


**Figure 3.10** The schematic device geometry for conductance measurements of Au/BFO/STO configuration.

### 3.3.4 Current-voltage measurement

The current-voltage (I-V) characteristic, or I-V curve, describes the relationship between current through and voltage across a BFO film. The I-V curve under UV illumination was performed to investigate the influence of BFO thin films on the photovoltaic effect. These phenomena were measured in the short-circuit current ( $I_{sc}$ ) at  $V = 0$  V and in the open-circuit voltages ( $V_{oc}$ ) at  $I = 0$  A. In these measurements, the voltage in sweep mode was applied, ranging from -10.0 V to 10.0 V for the Au/mBFO/STO configuration.

In this thesis, the Au/mBFO/STO configuration was applied at a high voltage of 0.80 kV ( $E \sim 20$  MV/cm) for 5 minutes between the electrodes and added electrodes with bias 1 and bias 2, as shown in the schematic diagram in Figure 3.11(a). Figure 3.11(b) shows the direction of applying positive and negative bias high voltage. Then, the I-V curve was measured from -10.0 V to 10.0 V upon UV irradiation. The

diode-like rectification effect was observed in which the positive and negative bias can be switched in the diode directions in the forward and reverse bias directions under UV illumination, respectively.

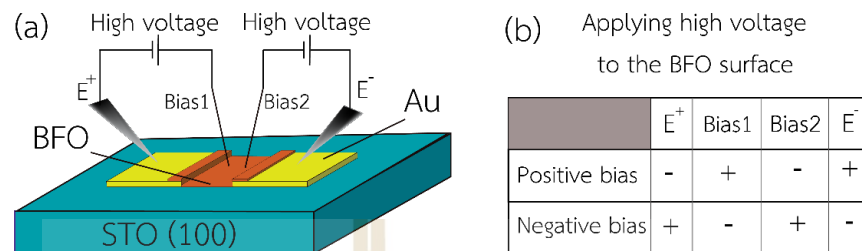


**Figure 3.11** (a) The schematic diagram of the Au/mBFO/STO configuration during bias high voltage. (b) the direction of positive and negative bias high voltage.



## CHAPTER IV

### RESULTS AND DISCUSSION

This chapter presents the results and the discussion. Section 4.1 presents the basic characterization of BFO thin films on the STO heterostructure. In sections 4.2 and 4.3, we present conductance and current-voltage characterizations. The last section is the mechanism and discussion.

#### 4.1 Basic characterization

##### 4.1.1 X-ray diffraction (XRD)

The 3 different conditions of BFO thin were studied in terms of crystallinity with a thickness of 743 nm. The x-ray diffraction spectra of the RT sample show an amorphous phase, and HT samples were clearly observed in the prominent (100) BFO reflections together with (100) peaks of the STO substrate, such as 100, 200, and 300, as shown in Figure 4.1. From the XRD pattern, the STO substrate shows an angle ( $2\theta$ ) equals  $22.75^\circ$  (100),  $46.47^\circ$  (200), and  $72.57^\circ$  (300). The BFO reflection peaks of the HT sample were shown to be higher than those of the CAL sample. That indicates the BFO thin films are almost epitaxial films on STO (100) single crystal substrates by the RF magnetron sputtering system. Except, BFO thin films are deposited at room temperature. However, the impurities phase from STO (100) substrates diffracted by Cu-K $\beta$  radiation were observed and labeled with the “\*” symbol.

In this thesis, the BFO thin films with RT conditions were the main sample to study the conductance of the heterostructure in 3 configurations and the effect of biasing high voltage. While the effect of the crystallinity on the conductance of the CAL and HT conditions was compared to the RT condition, only the Au/BFO/STO configuration was tested. Therefore, the next section of basic characterization of the CAL and HT conditions was explained in Appendix C.

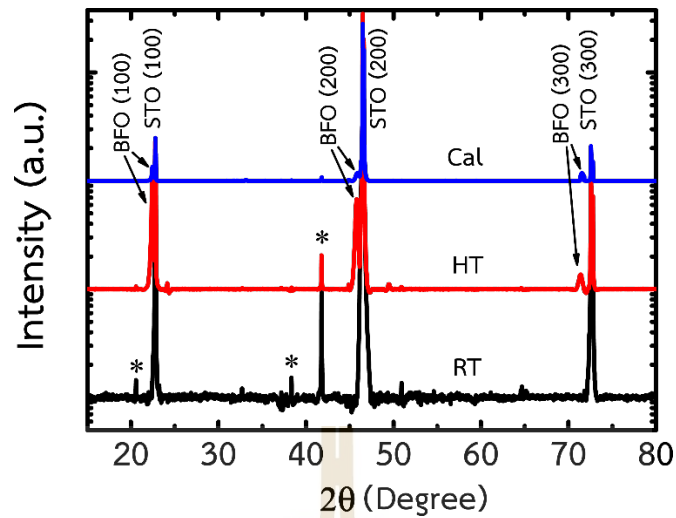


**Figure 4.1** XRD spectra of BFO/STO thin films at RT, HT, and CAL conditions. The diffraction peaks labeled with “\*” are from the STO (100) substrates diffracted by the Cu-K $\beta$  radiation.

#### 4.1.2 Atomic force microscope (AFM)

An atomic force microscope (AFM) is usually used to investigate a nanoscale sample's surface morphology. However, we employ AFM to investigate the thickness in cross-section. Before the deposition of BFO thin films, we used an ultra-thinned silicon wafer with a thickness of 50  $\mu\text{m}$  (University Wafer, Inc) to place on the center of an STO (100) substrate. After the deposition of BFO thin films, we removed the ultra-thinned silicon wafer from the STO substrate. It would have separate zones for coated BFO thin films and non-coated surfaces. Then, the AFM was scanned across these two areas. Figure 4.2 shows the line profile of the BFO/STO sample at a deposition time of 30 min (red) and the topography image as a contrast between high and low areas at RT condition. High and low areas are yellow and black, respectively. To average film thickness, we used data from five cross-section lines. The thickness of the BFO/STO at RT conditions was 20, 115, and 743 nm with a deposition time of 1, 5, and 30 min, respectively.

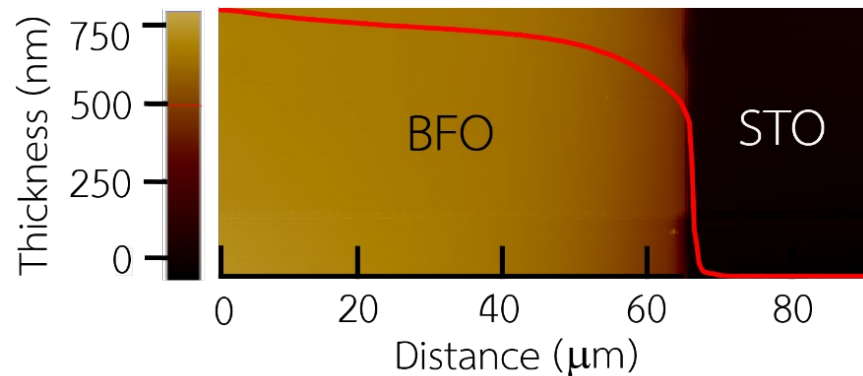


**Figure 4.2** The line profile of the BFO/STO sample at 30 min and the AFM image.

#### 4.1.3 Field emission scanning electron microscope (FESEM)

The morphology of the STO crystal and the BFO/STO sample were studied by FESEM using 50 kX magnification. Figure 4.3 shows the STO and BFO/STO at the RT condition at a deposition time of 1 min. Both surfaces are smooth and have a uniform surface. The morphology of BFO thin films at RT conditions is a like the STO crystal.

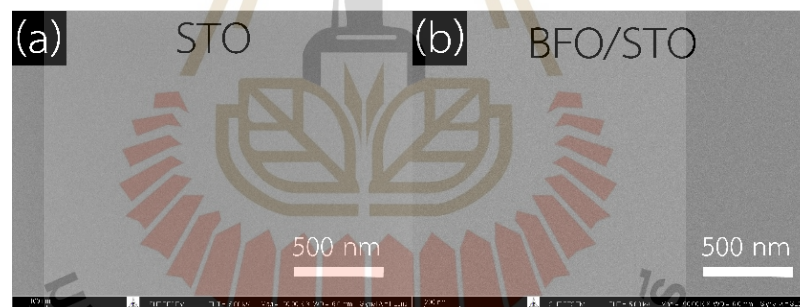


**Figure 4.3** FESEM images of (a) STO crystal and (b) BFO/STO sample in the RT condition at a deposition time of 1 min.

#### 4.1.4 Energy dispersive X-ray spectroscopy (EDS)

The elemental composition of the STO crystal and BFO/STO thin films was analyzed by energy dispersive X-ray spectroscopy (EDS). Figure 4.4 shows the EDS elemental analysis of the STO crystal and BFO/STO thin films in RT conditions. Each figure summarizes the number of elements in the weight percent and atomic percent. Figure 4.4(a) shows the STO crystal which the atomic percent of Sr, Ti, and O elements are 18.85, 16.96, and 64.18, respectively. The ratio of atomic percent between Sr, Ti, and O was 1:1:3. The EDS results of the BFO/STO samples at different deposition times

of 1, 5, and 30 min are shown in Figure 4.4(b-d). The atomic percent of Bi, Fe, and O were increased with increasing deposition times. Moreover, STO crystals could be detected at deposition times of 1, 5 min but the BFO of 30 min could only detect BFO thin films due to the thickness of BFO thin films. Therefore, the atomic ratios were 1:1:3, indicating the presence of  $\text{BiFeO}_3$  thin films in the BFO for 30 min. Except, the BFO for 1 and 5 min has oxygen from the STO crystal, which atomic percent of O was not 3 times.

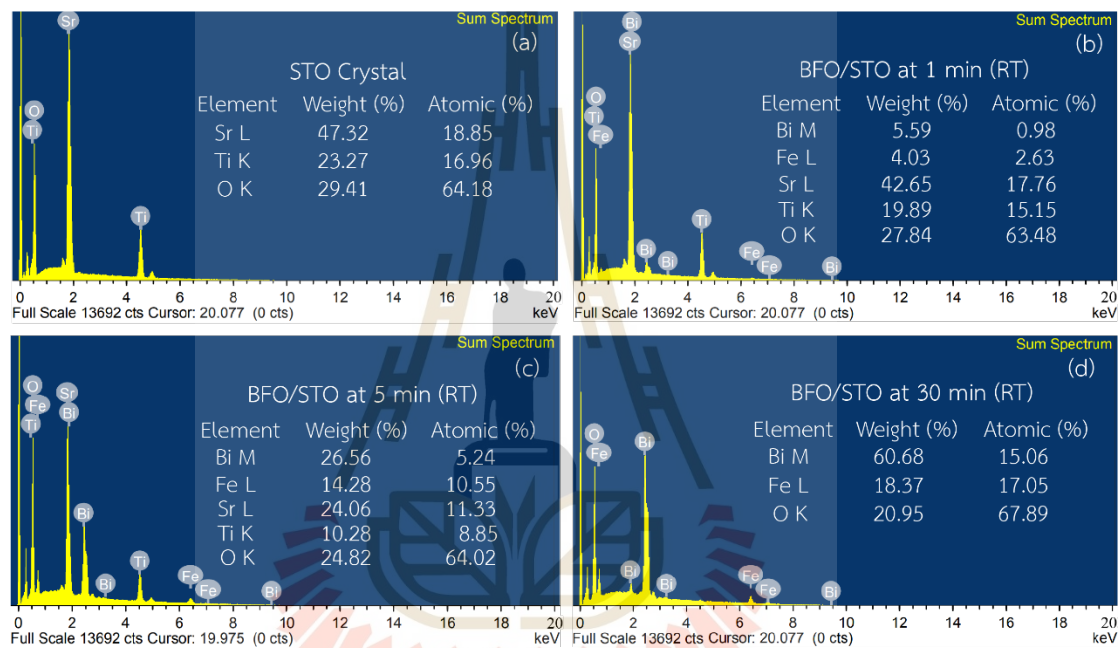


**Figure 4.4** EDS elemental analysis of (a) STO crystal. BFO on STO thin films in RT conditions with deposition times of (b) 1 min, (c) 5 min, and (d) 30 min.

#### 4.1.5 Ultraviolet visible spectroscopy (UV-VIS)

According to the Tauc equation as described in equation 3.2., the optical band gap ( $E_g$ ) is extrapolated by linear fitting of the plots between  $(\alpha hv)^2$  versus  $hv$  at  $(\alpha hv)^2 = 0$ . The BFO thin films were prepared on quartz substrates because they hardly absorb light, while the STO substrate has optical absorption. The optical absorption edges between  $(\alpha hv)^2$  versus  $hv$  of BFO/STO (RT) conditions with the thickness of 20, 115, and 743 nm and the band gap were determined by extrapolating the linear approach as illustrated in Figure 4.5. The optical band gap of BFO thin film has a band gap of 2.58, 2.60, and 2.67 eV for 20, 115, and 743 nm, respectively.

The transmission of BFO films was studied at a monochromatic light wavelength of 405 nm using Ocean Optics' HR4000 high-resolution spectrometer. The thickness of BFO thin films affected the transmission of a monochromatic light wavelength of 405 nm to the STO substrate. The transmission of BFO thin films through the STO substrate had a coefficient of 100, 62, 28, and 0.15 percent with a thickness of 0 (no BFO films), 20, 115, and 743 nm, respectively. Figure 4.6 show the transmission of BFO films at a monochromatic light wavelength of 405 nm varies with the thickness of the BFO films.

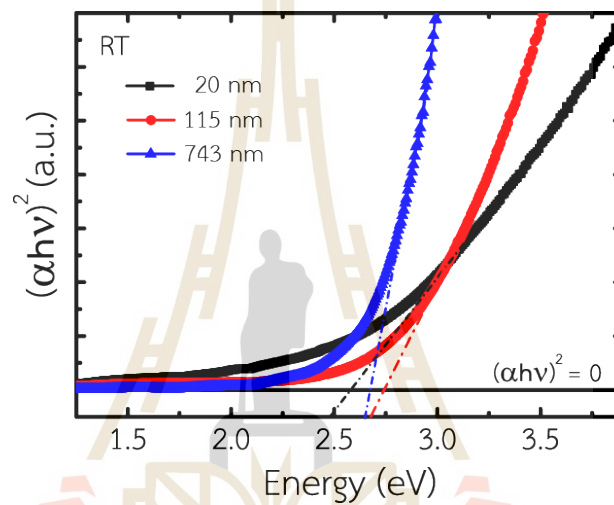


**Figure 4.5** The plots between  $(\alpha h\nu)^2$  versus  $h\nu$  of BFO/STO (RT) conditions with the thickness of 20, 115, and 743 nm.

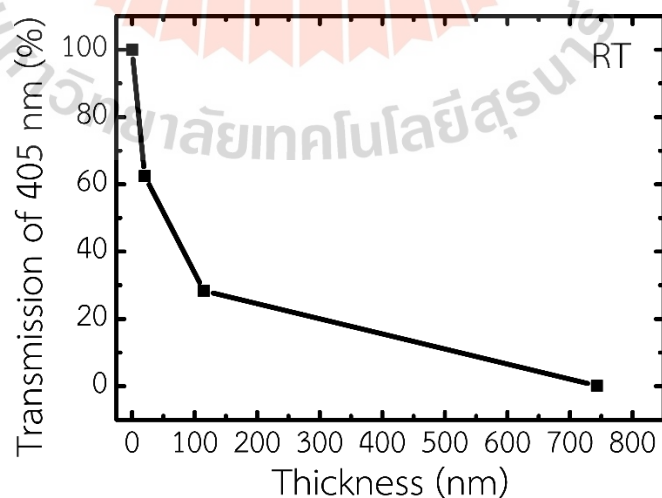


**Figure 4.6** The transmission of BFO films at a monochromatic light wavelength of 405 nm with the thickness of 20, 115, and 743 nm.

## 4.2 Conductance characterization

The electrical conductance of all samples was measured using the 2-wire resistance measurement. The heterostructures of Au/STO, Au/mBFO/STO, and Au/BFO/STO configurations were measured with multiple UV light exposures at 405 nm. The details of the conductance characterization are shown in sections 4.2.1 to 4.2.5, respectively.

### 4.2.1 Various configurations

In addition to the above-mentioned configurations, in this section we added two more samples to further cover the experimental results: the Au/SiO<sub>2</sub>/Si and the Au/mBFO/SiO<sub>2</sub>/Si configurations. The Au/SiO<sub>2</sub>/Si configuration was used as a reference sample, and it did not change with UV light exposure. While the Au/mBFO/SiO<sub>2</sub>/Si configurations were prepared BFO thin films, the growth parameters were the same as when coating on the STO substrate, but the deposition time was 5 minutes (115-nm-thick). The BFO thin films of the Au/mBFO/STO configuration was 115-nm-thick films. Figure 4.7 shows the time-dependent conductance with multiple UV light exposures. The conductance has non-linearly increased, with the Au/mBFO/STO configuration having greater conductance than the total of each individual BFO film (Au/mBFO/SiO<sub>2</sub>/Si configuration) and STO crystal (Au/STO configuration). The conductance of the Au/SiO<sub>2</sub>/Si configuration was 0.083 nS, which did not change when the UV was switched on. Therefore, this configuration was used as a reference sample and a substrate for BFO thin films for the conductance measurement. When the UV was switched on, the conductance of the Au/mBFO/SiO<sub>2</sub>/Si configuration rapidly increased from ~0.10 nS to ~0.23 nS ( $\Delta\sigma = 0.13$  nS). This result indicated the conductance of individual BFO thin films was switched by UV light. While the Au/STO configuration was enhanced from ~0.10 nS to ~3.67 nS ( $\Delta\sigma = 3.57$  nS). The conductance of Au/STO configuration was quickly increased to a peak state and subsequently rose due to the formation of oxygen-vacancy-induced and slow-charging 2DEG states at the STO substrate (Nathabumroong et al., 2020), (Suwanwong et al., 2015). After that, the conductance drops from the peak-state value to the dark-conductance value when the UV light is switched off, and the process continues under ON/OFF illumination. However, the Au/mBFO/STO configuration has

more conductance than the sum of each individual BFO thin films and STO crystal, which means the conductance has non-linearly increased from  $\sim 0.082$  pS to  $\sim 14.38$  nS ( $\Delta\sigma = 14.29$  nS).

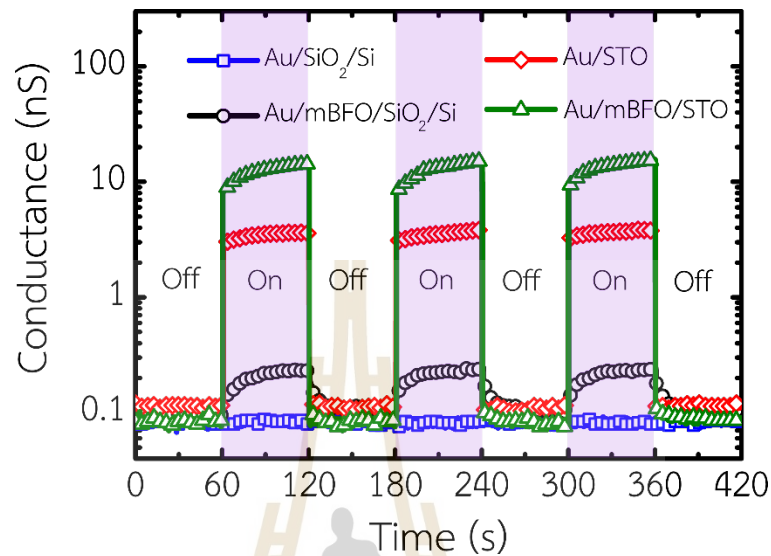


**Figure 4.7** The time-dependent conductance with different configurations with multiple UV light exposure cycles with Au/SiO<sub>2</sub>/Si, Au/mBFO/SiO<sub>2</sub>/Si, Au/STO crystal, and Au/mBFO/STO with the 115-nm-thick BFO films.

#### 4.2.2 Various thicknesses of BFO thin films

The conductances of the Au/mBFO/STO configuration with different thicknesses of 20, 115, and 743 nm and Au/STO were shown in Figure 4.8. When the UV was switched on, the conductance decreased with the increasing BFO film thickness. The 20-nm-thick films had the highest conductance under UV exposure, where the conductance increased from  $\sim 0.14$  nS to  $\sim 76.46$  nS ( $\Delta\sigma = 76.32$  nS). However, the 743-nm-thick films had the lowest conductance, which increased from  $\sim 0.10$  nS to  $\sim 0.92$  nS ( $\Delta\sigma = 0.82$  nS) under UV light irradiation. These results suggest that the conductance under UV exposure was mostly contributed by the BFO/STO interface. The thickness of BFO thin films was affected the transmission of a monochromatic light wavelength of 405 nm to the STO substrate. Therefore, the 20-nm-thick films had a transmission of BFO thin films through the STO substrate of 62%, which is the highest conductance response to UV light, as shown in Figure 4.6.

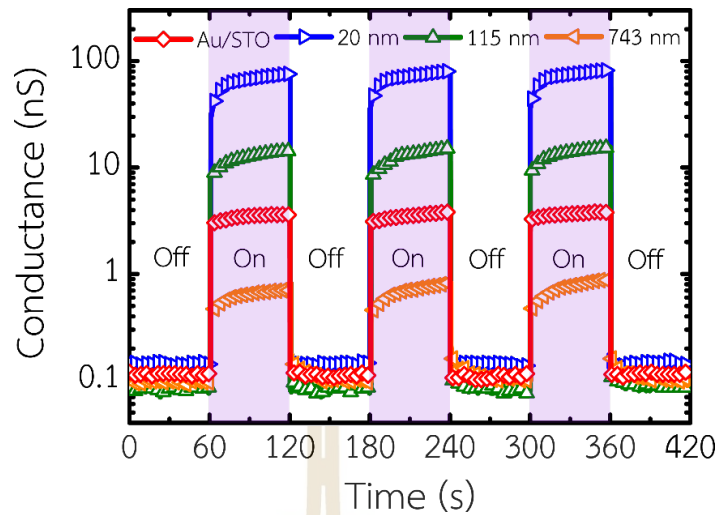


**Figure 4.8** The time-dependent conductance of Au/STO and Au/mBFO/STO configurations with different BFO thicknesses of 20, 115, and 743 nm with multiple UV light exposure cycles.

The maximum electrical conductance of two conditions with the topic 4.2.1 (varied configurations) and 4.2.2 (varied the thicknesses of BFO thin films) were summarized in Figure 4.9. The stack columns of the maximum conductance at different configurations with Au/mBFO/SiO<sub>2</sub>/Si (115-nm-thick BFO films), Au/STO, and Au/mBFO/STO (20-nm-thick BFO films) configurations have non-linearly increased under illumination.

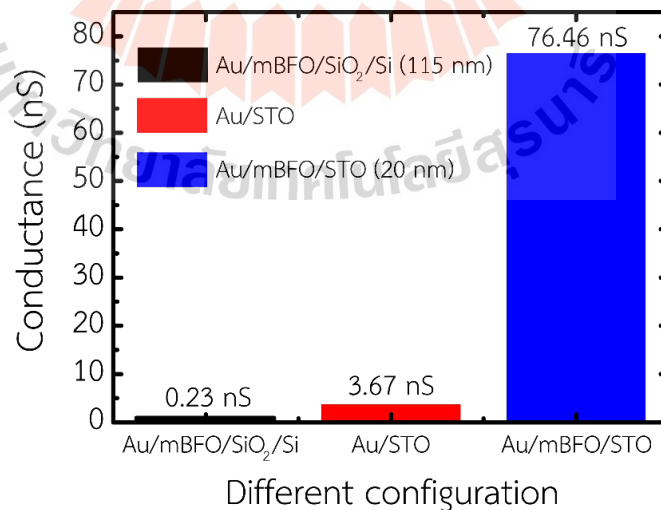


**Figure 4.9** The stack column of the maximum conductance at different configurations with Au/mBFO/SiO<sub>2</sub>/Si (115-nm-thick BFO films), Au/STO, and Au/mBFO/STO (20-nm-thick BFO films) configurations under illumination.

We fitted the transmission and maximum conductance values, which are reported in Figure 4.6 and Figure 4.9, respectively, as described in equation 4.1.

$$y = a \times \exp[b \times (x - c)] \quad (4.1)$$

Where  $a$ ,  $b$ , and  $c$  are coefficients, and  $x$  is the thickness of BFO thin films. The transmission coefficients of  $a$ ,  $b$ , and  $c$  are 66.27, 0.008, and 12.03, respectively, and conductance coefficients are 90.02, 0.017, and 10.64. We fitted the transmission and maximum conductance values as shown in Figure 4.10. It shows the transmission (black) and conductance (red) with the experiment data (symbol) and fitted data with equation 4.1 (line). An exponential decay of conductance is presented to create the 2DEG at the BFO/STO interface in the heterostructure. When the BFO thin films are thin, the conductance seems to be higher than that expected from the transmission. It may be due to the oxygen vacancy or quantum well effect in the thin film being higher than in the thick film. Therefore, BFO thin films with a thickness of 20 nm have shown the maximum conductance.

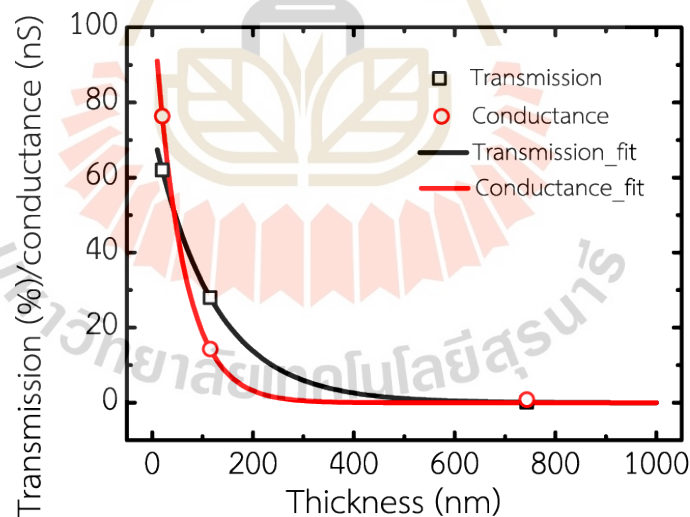


**Figure 4.10** The transmission (black) and conductance (red) of BFO films with thicknesses of 20, 115, and 743 nm with the experiment data (symbol) and fitted data (line).

To focus on stable conductance, we irradiated UV light all the time. The conductance progressively increased in the first stage, then reached its highest and most stable value, as shown in Figure 4.11. Under UV exposure, the conductance values for the Au/STO and Au/mBFO/STO configurations (20-nm-thick BFO films) were estimated to be  $\sim 4.05$  nS to  $\sim 110.51$  nS ( $\Delta\sigma = 106.46$  nS) at 300 seconds, respectively. The conductance of both samples under dark conditions was very close at  $\sim 0.10$ - $0.15$  nS, with the Au/mBFO/STO configuration slightly higher than the Au/STO configuration.

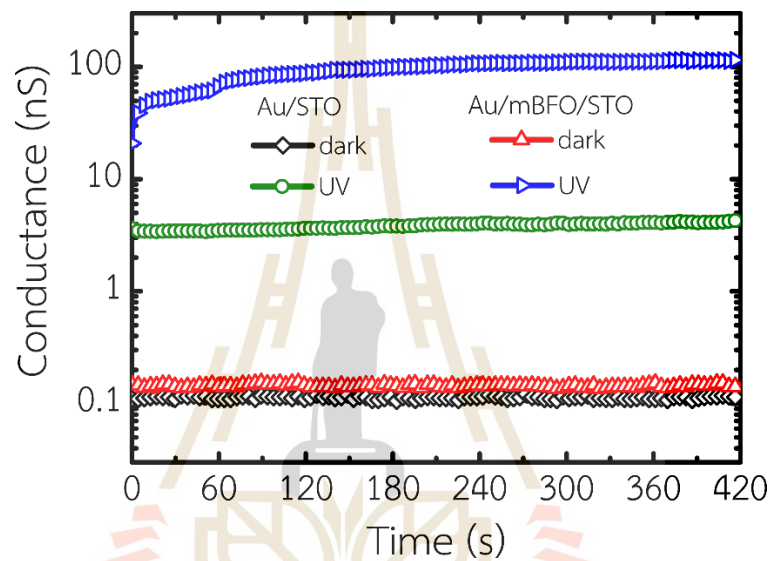


**Figure 4.11** The conductance of Au/STO and Au/mBFO/STO (20-nm-thick BFO films) configurations with and without (dark) UV illumination.

#### 4.2.3 Various Au/mBFO/STO and Au/BFO/STO configurations

The conductance of Au/mBFO/STO configuration was compared to the conductance of the Au/BFO/STO configuration under UV illumination. These results show that the conductance of the two configurations differed. The conductance of Au/mBFO/STO was higher than the Au/BFO/STO during UV light irradiation from  $\sim 35.52$  nS to  $\sim 76.85$  nS ( $\Delta\sigma = 41.33$  nS). The time-dependent conductance between Au/mBFO/STO and Au/BFO/STO (20-nm-thick BFO films) were shown in Figure 4.12. These results indicated that the Au/mBFO/STO configuration or BFO/STO interface created the 2DEG on STO. In dark conditions, the conductance of both samples was remarkably similar at  $\sim 0.10$ - $0.15$  nS where the conductance of the Au/mBFO/STO was slightly higher than the Au/BFO/STO.

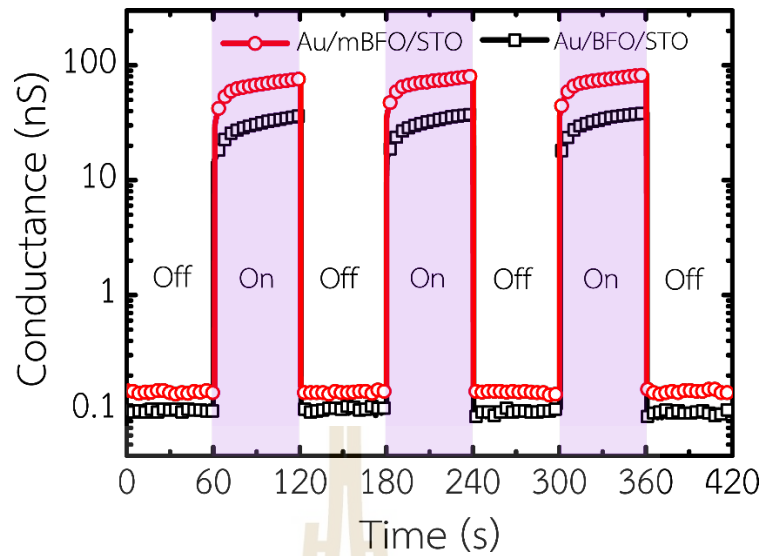


**Figure 4.12** The time-dependent conductance with different configurations with multiple UV light exposure cycles of Au/mBFO/STO and Au/BFO/STO configurations.

The 2DEG is created on the BFO/STO interface by UV radiation as shown in Figure 4.13. The conductance of the Au/mBFO/STO configuration is collected by 2DEG between the BFO/STO interface (Figure 4.13(a)), but not the conductance of the Au/BFO/STO configuration (Figure 4.13(b)). Therefore, the conductance of the Au/mBFO/STO configuration is higher than the Au/BFO/STO configuration due to the accumulated 2DEG. These results suggest that the 2DEG on BFO/STO was produced by UV radiation, and the Au/mBFO/STO configuration can measure the conductance to indicate the 2DEG formation.

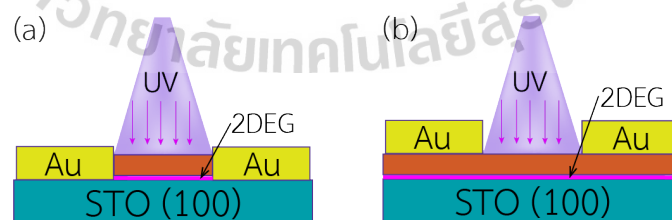


**Figure 4.13** Schematic diagram of the 2DEG creation with (a) Au/mBFO/STO and (b) Au/BFO/STO configurations.

#### 4.2.4 Various BiFeO<sub>3</sub> conditions of the Au/BFO/STO configuration

The effect of the crystallinity of BFO films on conductance was studied on the Au/BFO/STO configuration with 3 different conditions, e.g., RT, CAL, and HT. The thickness was 20 nm under all conditions. Because this configuration must deposit BFO thin films on the STO substrate before depositing the Au electrode, the CAL and HT conditions are suitable for this configuration. Figure 4.14 shows the time-dependent conductance with RT, HT, and CAL conditions with multiple UV light exposure cycles. Under UV illumination, the RT sample shows the highest conductance, and the HT and CAL samples are followed by ~35.50, ~27.61, and ~17.54 nS, respectively. In dark conditions, the conductance of both samples with RT and HT was remarkably similar at ~0.10 nS while the CAL sample was slightly smaller than in both conditions. The effect of 2DEG can be clearly observed on RT and HT samples, which increased conductance during UV illumination.

Consider the 2DEG, which is caused by UV radiation and induced by oxygen vacancies, as shown in Figure 4.13(b). The oxygen on the BFO surface has an important effect on oxygen vacancies and change conductance. We assume that oxygen on the BFO surface has an effect on oxygen vacancies, which more oxygen vacancies directly affects more conductance. Therefore, the atomic percent of oxygen (O) by EDS can be estimated to be that there is oxygen on the surface of the BFO. Figure 4.4(b) shows that amorphous BFO thin films (RT) have the highest atomic percent of oxygen, as shown in Figure C.3 of the HT condition and Figure C.4 of the CAL condition. Under UV illumination, the RT sample shows the highest conductance due to more oxygen vacancies than the CAT and HT conditions. Another reason is that the CAT condition should be more oxidized (less oxygen vacancies) in air annealing than the RT and HT conditions. The HT condition might also be oxidized in the high vacuum condition, which still has oxygen. Therefore, the defects and oxygen vacancies might be reduced in the annealing process as well, and fewer oxygen vacancies directly affect less conductance.

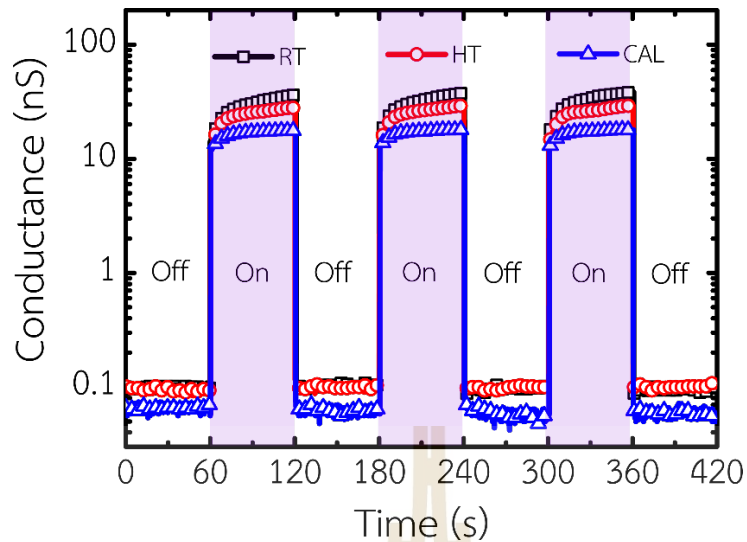


**Figure 4.14** The time-dependent conductance with RT, HT, and CAL conditions with multiple UV light exposure cycles.

#### 4.2.5 The effect of the electric field of the Au/mBFO/STO configuration

To demonstrate how to control the conductance of the Au/mBFO/STO configuration of 20-nm-thick BFO thin films, we applied electric fields across this configuration, as shown in Figure 3.10. The time-dependent conductances of the as-grown, after positive, and negative bias conditions are shown in Figure 4.15. The conductances were increased and decreased by  $\Delta\sigma = 58.91$  nS and decreased by  $\Delta\sigma = 9.93$  nS after the positive and negative bias under UV illumination, respectively. We can control the conductance to increase or decrease by using an electric field to change the polarization of BFO thin films. As a result, an electric field was used to switch the ferroelectric polarization and control the conductance. As we know from our previous work, during irradiation, oxygen vacancies are generated, and the 2DEG state begins to develop inside the quantum well (Meevasana et al., 2011; Suwanwong et al., 2015). The charge on the surface or interface localized oxygen vacancies causes a spatial redistribution of bulk carriers towards the surface/interface, which is associated with the band bending at the surface. To understand more about the increase or decrease of conductance by external electric fields, we explain the quantum-well states of the 2DEG state in the Au/mBFO/STO configuration. The polarization of BFO thin films can be controlled and switched in the polarization direction by an electric field. The quantum well may be modified to be shallower or

deeper by polarization of BFO thin films. The charges can accumulate less in shallow quantum wells. It causes the electrical conductivity of the material to decrease. The deeper quantum wells can accumulate more charges. As a result, the electrical conductivity is increased.

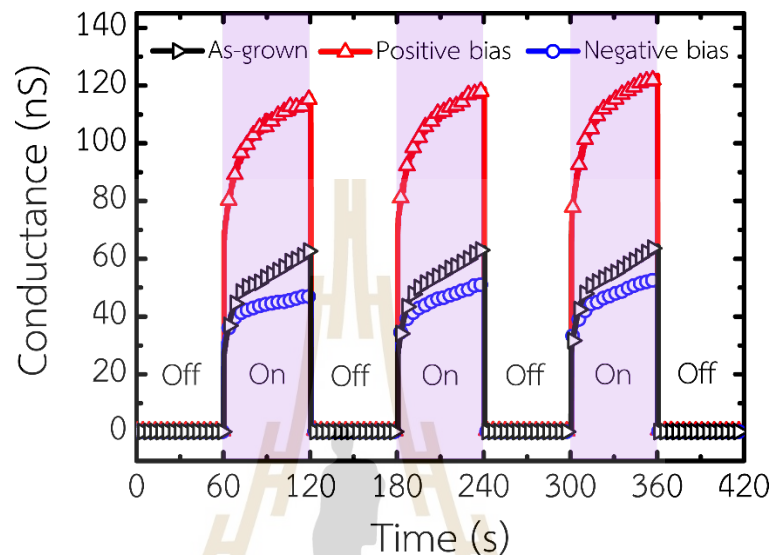


**Figure 4.15** The time-dependent conductance of the Au/mBFO/STO configuration with the as-grown, after positive and negative bias conditions (applying electric fields across the BFO/STO interface) with multiple UV light exposure cycles.

### 4.3 Current-voltage characterization

A significant diode-like rectification effect was observed at the Au/mBFO/STO configuration after applying an external electric field to the BFO surface under UV illumination. Figure 4.16(a) shows the I-V characteristics of the Au/mBFO/STO configuration with the as-grown, after positive, and negative bias conditions under UV light exposure. The photocurrent in the as-grown condition was clearly observed linearly upon illumination. The conductance of the I-V curve can be calculated from the slope of the curve. Therefore, the conductance of the as-grown condition was  $\sim 19.30$  nS. The electric field with positive and negative bias can be switched in the diode directions with the forward and reverse bias directions, respectively. The conductance in the positive voltage range (0 V to 10.0 V) was  $\sim 29.85$  nS (an increase of 54.66%) and  $\sim 8.48$  nS (a decrease of 56.10%) for positive and negative bias,

respectively. The conductance in the negative voltage range (-10.0 V to 0 V) was  $\sim 9.07$  nS (a decrease of 53%) and  $\sim 27.16$  nS (an increase of 40.72%) for positive and negative bias, respectively.

The zoomed in area clearly presents photovoltaic behaviors, as shown in Figure 4.16(b). The short-circuit current ( $I_{sc}$ ) at  $V = 0$  V and open-circuit voltages ( $V_{oc}$ ) at  $I = 0$  A were 35.0 nA and -1.86 V for as-grown conditions, respectively. This result demonstrated the photovoltaic behaviors that inferred the self-polarized and built-in electric field in BFO thin films under illumination (Li et al., 2021). The  $I_{sc}$  and  $V_{oc}$  can be controlled to increase or decrease by using an electric field to change the polarization of BFO thin films. The  $I_{sc}$  and  $V_{oc}$  were 65.0 nA and -4.62 V for positive bias. For negative bias, the  $I_{sc}$  and  $V_{oc}$  were 16.0 nA and -0.50 V.

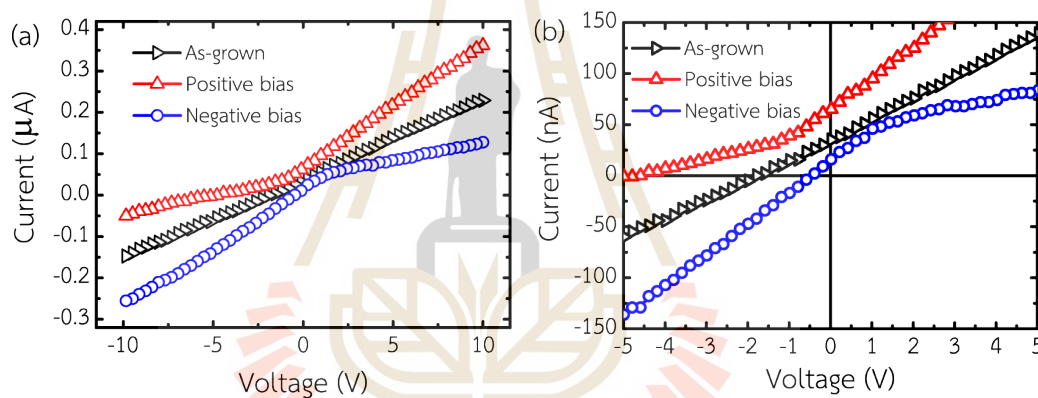
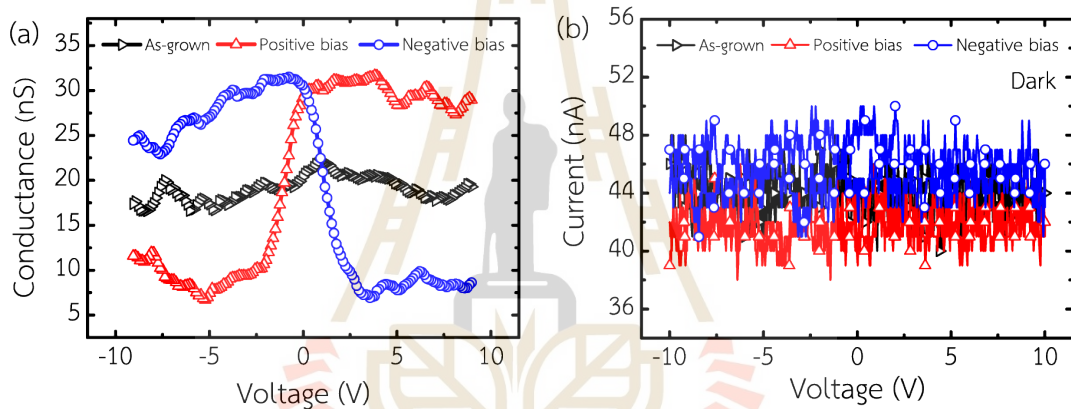


**Figure 4.16** The I-V characteristics of the Au/mBFO/STO configuration with the as-grown, after positive, and negative bias conditions under UV light exposure (a) from -10.0 V to 10.0 V and (b) from -5.0 V to 5.0 V. These zoomed in areas clearly present photovoltaic behaviors.

These results, compared with Figure 2.11 on page 20, showed a similar diode-like effect. After positive and negative bias conditions, the I-V characteristics under illumination (Figure 4.16) look like Figure 2.11(a) downward and Figure 2.11(b) upward polarizations. These indicated that applying an external electric field to the BFO surface under UV illumination showed the same behavior as applying electric voltage pulses to the top and bottom electrodes. The surface, or horizontal, bias was changed the polarization direction. However, the dark condition did not exhibit a diode-like effect, as shown in Figure 4.17(b), which was different from the experimental results in Figure

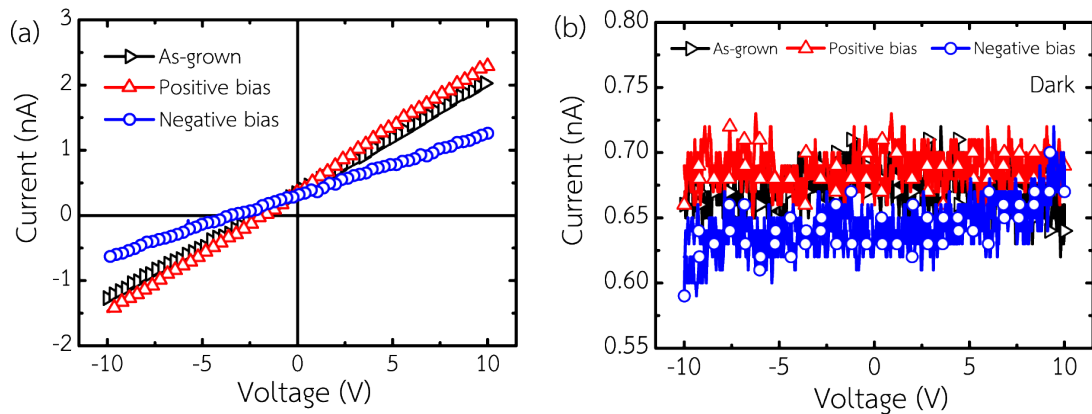
2.11. All the conditions, the as-grown, after positive and negative bias, the I-V curves look the same. The significant diode-like rectification effect was observed only under UV illumination.

Figure 4.17(a) presents the electrical conductance and voltage curves of the Au/mBFO/STO configuration measured under UV irradiation. Note that the electrical conductance shown in Figure 4.17(a) is calculated from the slope in Figure 4.16(a). The as-grown case (triangle black line) is linear upon UV irradiation, and the electrical conductance is  $\approx 19.30$  nS. Interestingly, the positive bias (triangle red line) increases the electrical conductance by up to  $\Delta\sigma = 20$  nS, while the negative bias (circle blue line) decreases the electrical conductance by up to  $\Delta\sigma = 20$  nS.



**Figure 4.17** (a) Conductance and voltage with UV illumination with the as-grown, after positive, and negative bias. (b) The I-V characteristics of the Au/mBFO/STO configuration with the as-grown, after positive, and negative bias in the dark condition.

Figure 4.18(a) shows the I-V characteristics of the Au/mBFO/Si configuration with the as-grown, after positive, and negative bias conditions under UV light exposure. The I-V curves of all conditions were observed to be linear. The conductance was  $\sim 0.16$ ,  $\sim 0.19$ , and  $\sim 0.09$  ns for as-grown, after positive and negative bias, respectively. The significant diode-like rectification effect was not observed in the Au/mBFO/Si configuration. The I-V curve also clearly presents photovoltaic behaviors. The  $I_{sc}$  and  $V_{oc}$  were 0.37 nA and -0.04 V, which are all almost the same. These indicate that the FEPV is observed from BFO thin films under UV illumination. Figure 4.18(b) shows the I-V characteristics in the dark condition, which do not exhibit a diode-like effect, as well as those shown in Figure 4.17(b).



**Figure 4.18** The I-V characteristics of the Au/mBFO/Si configuration with the as-grown, after positive, and negative bias with (a) under UV light exposure and (b) in the dark condition.

#### 4.4 Mechanism and discussion

Figure 4.19(a)-(h) presents our proposed mechanisms for explaining the change in electrical conductance of BFO thin films on STO. Consider the schematic representation of the oxygen vacancies caused by UV radiation on the STO substrate as shown in Figure 4.19(a). The oxygen vacancies originate from UV light irradiation of the STO surface after the 2DEG occupies the quantum well. The polarization ( $P$ ) direction is depicted, and the STO surface has donor-like surface states that form a positive charge, which bends the band downward in the system. The potential well of STO is shown in Figure 4.19(b). The electrostatic potential is  $U = qV$ , where  $q$  is the point charge and  $V$  is the electric potential of a point charge. The charge  $q$  is represented by the electron charge ( $e$ ). The slope of this graph represents the electric field, which is large at the surface, whereas the electric field is screened in the bulk (far from the surface). This represents the 2DEG states located inside the quantum well caused by the bending downward of the band due to the photo-induced oxygen vacancy. After UV irradiation of the BFO/STO interface, the 2DEG increases immediately due to the polarization produced by the BFO topping layer as shown in Figure 4.19(c). The polarization modifies the quantum well states of the STO substrate, resulting in the deeper quantum well states of the BFO/STO interface as shown in Figure 4.19(d). The proposed model suggests that the polarization produced by BFO explains how the electrical conductance of the BFO/STO interface is greater than that of STO.

Next, the variation in electrical conductance of the BFO/STO interface upon applying an external electrical field can be understood based on the mechanisms illustrated in Figure 4.19(e) and Figure 4.19(g). The tunable electrical conductance of the BFO/STO interface under external electric field is explained by the complementary electric field ( $E_0 + \Delta E$ ) in positive bias and by the opposite electric field in negative bias ( $E_0 - \Delta E$ ), resulting from the electric field switching the polarization in the BFO thin film, as shown in Figure 4.19(f) and Figure 4.19(h). The quantum wells of positive bias and negative bias become deeper (see Figure 4.19(f)) and shallower (see Figure 4.19(h)) by the polarization of BFO thin films, respectively. We conclude that the variation in the electrical conductance at the BFO/STO interface under an external electric field may be attributed to less electron accumulation in shallow quantum wells (negative bias) and more electron accumulation in deep quantum wells (positive bias), leading to the decrease in electrical conductivity and the increase in electrical conductivity, respectively.

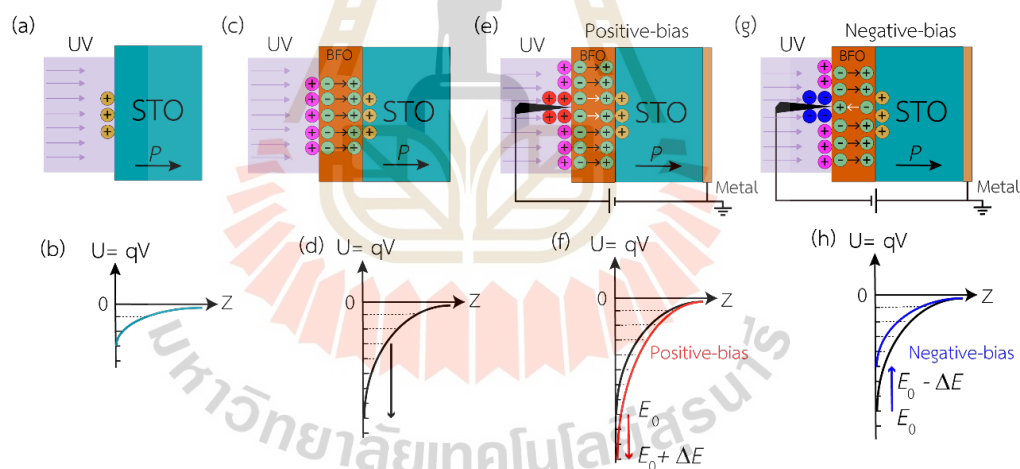


**Figure 4.19** Schematic diagram of UV-light-induced oxygen vacancies. (a) STO crystal and BFO/STO interface with (c) zero bias, (e) positive bias, and (g) negative bias. The electrostatic potential changes as a function of depth  $Z$  from the surface to the bulk. (b) STO crystal and BFO/STO interface with the (d) zero bias, (f) positive bias, and (h) negative bias. The yellow and pink positive charges represent the oxygen vacancy charge of STO and the BFO/STO interface, respectively. The injection charges are red and blue charges for positive and negative bias, respectively. The green charges represent polarization charges, while the black and white arrows represent polarization directions ( $P$ ) caused by UV light and bias, respectively.

## CHAPTER V

### CONCLUSION AND FUTURE RESEARCH

#### 5.1 Conclusions

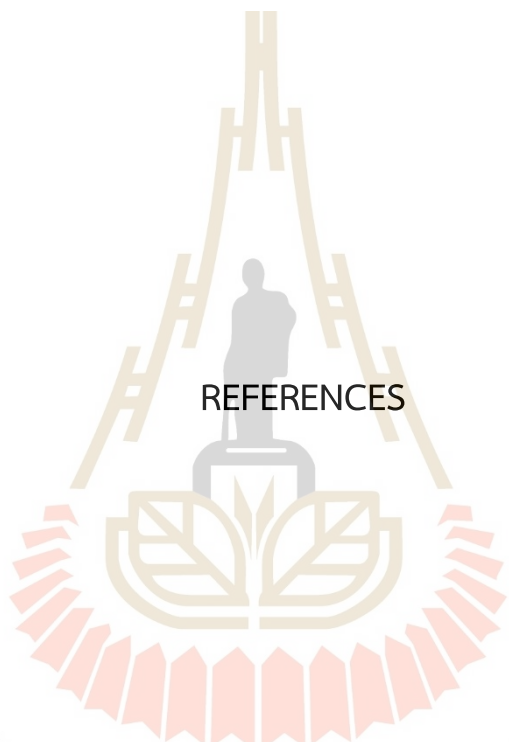
In this thesis, we study the BFO thin films heterostructure with basic characterization, conductance, and current-voltage measurement. The BFO thin films on STO (100) were prepared using our home-made RF magnetron sputtering system under 3 different conditions, e.g., RT, HT, and CAL conditions. For the conductance measurement, there are 3 configurations of the heterostructure as follows: Au/STO, Au/mBFO/STO, and Au/BFO/STO configurations under multiple UV light exposures. The BFO thin films with RT conditions were the main sample to study the conductance of the heterostructure in 3 configurations and the effect of biasing high voltage. While the CAL and HT conditions were compared to the conductance with the RT condition, only the Au/BFO/STO configuration was tested. The results of our experiment with the 20-nm-thick BFO thin films at RT conditions can be summarized as follows: First, the conductance has non-linearly increased, with the Au/mBFO/STO configuration having a greater conductance than the total of each individual BFO film and STO crystal. Under UV exposure, the conductance was  $\sim 76.46$  nS, while the BFO film and STO crystal were  $\sim 0.23$  nS and  $\sim 3.67$ . Second, the conductance can be controlled to increase or decrease by using an electric field to switch the ferroelectric polarization of BFO thin films. The conductances of the Au/mBFO/STO configuration were increased by  $\Delta\sigma = 58.91$  nS and decreased by  $\Delta\sigma = 9.93$  nS after the positive and negative bias under UV illumination. The quantum well may be modified to be shallower or deeper by the polarization of BFO thin films. The charges can accumulate less in shallow quantum wells. It causes the electrical conductivity of the material to decrease. The deeper quantum wells can accumulate more charges. As a result, the electrical conductivity is increased. Moreover, a significant diode-like rectification effect was observed at the Au/mBFO/STO configuration after applying an external electric field to the BFO surface under UV illumination. The electric field with positive and negative

bias can be switched in the diode directions with the forward and reverse bias directions, respectively. The polarization of BFO thin films can also be controlled by the electric field that is applied to the BFO surface. The I-V curve demonstrated the photovoltaic behaviors that inferred the self-polarized and built-in electric field in BFO thin films under illumination. The  $I_{sc}$  and  $V_{oc}$  can be controlled to increase or decrease by using an electric field to change the polarization of BFO thin films.

## 5.2 Improvement and future research

In studying the mechanism inside BFO thin films that increases the conductance during UV light illumination, we must do more experiments and characterization by X-ray photoelectron spectroscopy (XPS). The investigation of the polarization of BFO thin films should be characterized by piezoresponse force microscopy (PFM). The effects of light irradiation will be studied at a variety of wavelengths, such as green light and red light. The high voltage bias to BFO thin films should be reduced to levels equal to those used in general electronic circuits.





REFERENCES

มหาวิทยาลัยเทคโนโลยีสุรนารี

## REFERENCES

- Acharya, A., Roy, G. S., and Mishra, R. (2010). Comparative Study of Performance of CdS, CdSe thin film CdS-PTh, CdSe-PTh nanocomposite thin films Using SEM-EDXA (Scanning Electron Microscope) and FTIR (Fourier Transform Infrared Spectroscopy). *Latin-American Journal of Physics Education*. 4(3): 22.
- Achenbach, G., James, W., and Gerson, R. (1967). Preparation of single-phase polycrystalline BiFeO<sub>3</sub>. *Journal of the American Ceramic Society*. 50(8): 437-437.
- Andreeva, N., Petraru, A., Vilkov, O. Y., and Petukhov, A. (2020). Structure-resistive property relationships in thin ferroelectric BaTiO<sub>3</sub> films. *Scientific reports*. 10(1): 1-9.
- Aswin, V., Kumar, P., Pal, P., and Dogra, A. (2016). Photo-resistive properties of LaAl 0.6 Cr<sub>0.4</sub>O<sub>3</sub>/SrTiO<sub>3</sub> heterostructures: a comparative study with LaAlO<sub>3</sub>/SrTiO<sub>3</sub>. *Optics Letters*. 41(6): 1134-1137.
- Bhatnagar, A., Kim, Y. H., Hesse, D., and Alexe, M. (2014). Persistent photoconductivity in strained epitaxial BiFeO<sub>3</sub> thin films. *Nano letters*. 14(9): 5224-5228.
- Bibes, M., and Barthélémy, A. (2008). Towards a magnetoelectric memory. *Nature materials*. 7(6): 425-426.
- Catalan, G., and Scott, J. F. (2009). Physics and applications of bismuth ferrite. *Advanced Materials*. 21(24): 2463-2485.
- Chen, C., Lv, S., Li, J., Wang, Z., Liang, X., Li, Y., Viehland, D., Nakajima, K., and Ikuhara, Y. (2015). Two-dimensional electron gas at the Ti-diffused BiFeO<sub>3</sub>/SrTiO<sub>3</sub> interface. *Applied Physics Letters*. 107(3): 031601.
- Choi, T., Lee, S., Choi, Y., Kiryukhin, V., and Cheong, S.-W. (2009). Switchable ferroelectric diode and photovoltaic effect in BiFeO<sub>3</sub>. *Science*. 324(5923): 63-66.
- Das, M., and Kumar, S. (2021). Effect of Surface Variations on Resistive Switching. *Memristor: An Emerging Device for Post-Moore's Computing and Applications*: 25.

- Das, R., Kim, D., Baek, S., Eom, C., Zavaliche, F., Yang, S., Ramesh, R., Chen, Y., Pan, X., and Ke, X. (2006). Synthesis and ferroelectric properties of epitaxial BiFeO<sub>3</sub> thin films grown by sputtering. *Applied Physics Letters*. 88(24): 242904.
- Dziubaniuk, M., Bujakiewicz-Korońska, R., Suchanicz, J., Wyrwa, J., and Rękas, M. (2013). Application of bismuth ferrite protonic conductor for ammonia gas detection. *Sensors and Actuators B: Chemical*. 188: 957-964.
- Ederer, C., and Spaldin, N. A. (2005). Recent progress in first-principles studies of magnetoelectric multiferroics. *Current Opinion in Solid State and Materials Science*. 9(3): 128-139.
- Eom, C., Marshall, A., Laderman, S., Jacowitz, R., and Geballe, T. (1990). Epitaxial and smooth films of a-axis YBa<sub>2</sub>Cu<sub>3</sub>O<sub>7</sub>. *Science*. 249(4976): 1549-1552.
- Eom, C., Sun, J., Yamamoto, K., Marshall, A., Luther, K., Geballe, T., and Laderman, S. (1989). In situ grown YBa<sub>2</sub>Cu<sub>3</sub>O<sub>7- $\delta$</sub>  thin films from single-target magnetron sputtering. *Applied Physics Letters*. 55(6): 595-597.
- Fu, Z., Chen, H., Liu, Y., Liu, M., and Liu, W.-M. (2021). Interface-induced ferroelectric domains and charged domain walls in BiFeO<sub>3</sub>/SrTiO<sub>3</sub> superlattices. *Physical Review B*. 103(19): 195301.
- Gomez-Iriarte, G., Labre, C., de Oliveira, L., and Sinnecker, J. (2018). Pure phase BiFeO<sub>3</sub> thin films sputtered over Si: A new route towards high magnetization. *Journal of Magnetism and Magnetic Materials*. 460: 83-88.
- Guo, H., Saidi, W. A., and Zhao, J. (2016). Tunability of the two-dimensional electron gas at the LaAlO<sub>3</sub>/SrTiO<sub>3</sub> interface by strain-induced ferroelectricity. *Physical Chemistry Chemical Physics*. 18(41): 28474-28484.
- Hertz, H. (1887). Ueber einen Einfluss des ultravioletten Lichtes auf die elektrische Entladung. *Annalen der Physik*. 267(8): 983-1000.
- Ichinose, T., Miura, D., and Naganuma, H. (2021). High-Quality Sputtered BiFeO<sub>3</sub> for Ultrathin Epitaxial Films. *ACS Applied Electronic Materials*. 3(11): 4836-4848.
- Jaiban, P., Lu, M.-H., Eknapakul, T., Chaiyachad, S., Yao, S., Pisitpipathsin, N., Unruan, M., Siroj, S., He, R.-H., and Mo, S.-K. (2020). Spectral weight reduction of two-dimensional electron gases at oxide surfaces across the ferroelectric transition. *Scientific reports*. 10(1): 1-7.

- Ji, W., Yao, K., and Liang, Y. C. (2010). Bulk photovoltaic effect at visible wavelength in epitaxial ferroelectric BiFeO<sub>3</sub> thin films. *Advanced Materials*. 22(15): 1763-1766.
- Jubu, P., Yam, F., Igba, V., and Beh, K. (2020). Tauc-plot scale and extrapolation effect on bandgap estimation from UV-vis-NIR data—a case study of  $\beta$ -Ga<sub>2</sub>O<sub>3</sub>. *Journal of Solid State Chemistry*. 290: 121576.
- Katiyar, R. K., Sharma, Y., Barrionuevo Diestra, D. G., Misra, P., Kooriyattil, S., Pavunny, S. P., Morell, G., Weiner, B. R., Scott, J., and Katiyar, R. S. (2015). Unipolar resistive switching in planar Pt/BiFeO<sub>3</sub>/Pt structure. *AIP Advances*. 5(3): 037109.
- Khan, R., Ilyas, N., Shamim, M. Z. M., Ilyas Khan, M., Sohail, M., Rahman, N., Khan, A. A., Khan, S., and Khan, A. (2021). Oxide-Based Resistive Switching Devices: Fabrication, Influence Parameters and Applications. *Journal of Materials Chemistry C*.
- Kim, S. I., Kim, D. H., Kim, Y., Moon, S. Y., Kang, M. G., Choi, J. K., Jang, H. W., Kim, S. K., Choi, J. W., and Yoon, S. J. (2013). Non-volatile control of 2DEG conductivity at oxide interfaces. *Advanced Materials*. 25(33): 4612-4617.
- King, P., He, R., Eknapakul, T., Buaphet, P., Mo, S.-K., Kaneko, Y., Harashima, S., Hikita, Y., Bahramy, M., and Bell, C. (2012). Subband structure of a two-dimensional electron gas formed at the polar surface of the strong spin-orbit perovskite KTaO<sub>3</sub>. *Physical review letters*. 108(11): 117602.
- Kormondy, K. J., Gao, L., Li, X., Lu, S., Posadas, A. B., Shen, S., Tsoi, M., McCartney, M. R., Smith, D. J., and Zhou, J. (2018). Large positive linear magnetoresistance in the two-dimensional t<sub>2g</sub> electron gas at the EuO/SrTiO<sub>3</sub> interface. *Scientific reports*. 8(1): 1-9.
- Kossar, S., Amiruddin, R., and Rasool, A. (2021). Study on thickness-dependence characteristics of bismuth ferrite (BFO) for ultraviolet (UV) photodetector application. *Micro and Nano Systems Letters*. 9(1): 1-10.
- Kubel, F., and Schmid, H. (1990). Structure of a ferroelectric and ferroelastic monodomain crystal of the perovskite BiFeO<sub>3</sub>. *Acta Crystallographica Section B: Structural Science*. 46(6): 698-702.
- Lacy, F. (2010). Evaluating the resistivity-temperature relationship for RTDs and other conductors. *IEEE Sensors Journal*. 11(5): 1208-1213.

- Lebeugle, D., Colson, D., Forget, A., Viret, M., Bonville, P., Marucco, J.-F., and Fusil, S. (2007). Room-temperature coexistence of large electric polarization and magnetic order in BiFeO<sub>3</sub> single crystals. *Physical Review B*. 76(2): 024116.
- Lee, S. W., Liu, Y., Heo, J., and Gordon, R. G. (2012). Creation and control of two-dimensional electron gas using Al-based amorphous oxides/SrTiO<sub>3</sub> heterostructures grown by atomic layer deposition. *Nano letters*. 12(9): 4775-4783.
- Li, C., Hong, Y., Xue, H., Wang, X., Li, Y., Liu, K., Jiang, W., Liu, M., He, L., and Dou, R. (2018). Formation of two-dimensional electron gas at amorphous/crystalline oxide interfaces. *Scientific reports*. 8(1): 1-9.
- Li, J., Chen, W., Qian, G., and Cheng, J. (2020). Structure and Properties of Preferential (110) Orientation BiFeO<sub>3</sub> Thin Films by Sol-Gel Method. *Integrated Ferroelectrics*. 210(1): 161-166.
- Li, J., Wang, J., Wuttig, M., Ramesh, R., Wang, N., Ruetter, B., Pyatakov, A. P., Zvezdin, A., and Viehland, D. (2004). Dramatically enhanced polarization in (001),(101), and (111) BiFeO<sub>3</sub> thin films due to epitaxial-induced transitions. *Applied Physics Letters*. 84(25): 5261-5263.
- Li, Y., Sritharan, T., Zhang, S., He, X., Liu, Y., and Chen, T. (2008). Multiferroic properties of sputtered BiFeO<sub>3</sub> thin films. *Applied Physics Letters*. 92(13): 132908.
- Li, Z., Zhao, Y., Li, W.-L., Song, R., Zhao, W., Wang, Z., Peng, Y., and Fei, W.-D. (2021). Photovoltaic Effect Induced by Self-Polarization in BiFeO<sub>3</sub> Films. *The Journal of Physical Chemistry C*. 125(17): 9411-9418.
- Li, Z., Zhao, Y., Li, W., Song, R., Zhang, Y., Zhao, W., Wang, Z., Peng, Y., and Fei, W. (2021). Enhanced energy storage properties of amorphous BiFeO<sub>3</sub>/Al<sub>2</sub>O<sub>3</sub> multilayers. *Journal of Materials Research and Technology*. 11: 1852-1858.
- Lines, M. E., and Glass, A. M. (2001). *Principles and applications of ferroelectrics and related materials*: Oxford university press.
- Masingboon, C., Eknapakul, T., Suwanwong, S., Buaphet, P., Nakajima, H., Mo, S.-K., Thongbai, P., King, P., Maensiri, S., and Meevasana, W. (2013). Anomalous change in dielectric constant of CaCu<sub>3</sub>Ti<sub>4</sub>O<sub>12</sub> under violet-to-ultraviolet irradiation. *Applied Physics Letters*. 102(20): 202903.

- Maurya, D., Sardarinejad, A., and Alameh, K. (2014). Recent developments in RF Magnetron sputtered thin films for pH sensing applications an overview. *Coatings*. 4(4): 756-771.
- Meevasana, W., King, P., He, R., Mo, S., Hashimoto, M., Tamai, A., Songsiriritthigul, P., Baumberger, F., and Shen, Z. (2011). Creation and control of a two-dimensional electron liquid at the bare SrTiO<sub>3</sub> surface. *Nature materials*. 10(2): 114-118.
- Micard, Q., Condorelli, G. G., and Malandrino, G. (2020). Piezoelectric BiFeO<sub>3</sub> thin films: Optimization of MOCVD process on Si. *Nanomaterials*. 10(4): 630.
- Michel, C., Moreau, J.-M., Achenbach, G. D., Gerson, R., and James, W. J. (1969). The atomic structure of BiFeO<sub>3</sub>. *Solid State Communications*. 7(9): 701-704.
- Mijiti, A., Mamat, M., Xiaerding, F., Wang, Q., Abudurexiti, A., and Aihaiti, L. (2021). Electron-beam evaporated bismuth ferrite (BiFeO<sub>3</sub>) thin films and characterization. *Materials Research Express*. 8(3): 036408.
- Moreau, J.-M., Michel, C., Gerson, R., and James, W. J. (1971). Ferroelectric BiFeO<sub>3</sub> X-ray and neutron diffraction study. *Journal of Physics and Chemistry of Solids*. 32(6): 1315-1320.
- Naganuma, H. (2011). Multifunctional Characteristics of B-site Substituted BiFeO<sub>3</sub> Films. *New York: Intech*: 373.
- Nakashima, S., Hayashimoto, R., Fujisawa, H., and Shimizu, M. (2018). Bulk photovoltaic effects in Mn-doped BiFeO<sub>3</sub> thin films and the optical strains. *Japanese Journal of Applied Physics*. 57(11S): 11UF11.
- Nakashima, S., Higuchi, T., Yasui, A., Kinoshita, T., Shimizu, M., and Fujisawa, H. (2020). Enhancement of photovoltage by electronic structure evolution in multiferroic Mn-doped BiFeO<sub>3</sub> thin films. *Scientific reports*. 10(1): 1-8.
- Nakashima, S., Takayama, K., Uchida, T., Fujisawa, H., and Shimizu, M. (2015). Anomalous photovoltaic effects in Pt/single-domain-structured BiFeO<sub>3</sub>/Pt coplanar capacitors on SrTiO<sub>3</sub> substrates. *Japanese Journal of Applied Physics*. 54(10S): 10NA16.
- Nam, H., Seol, K.-H., Lee, J., Cho, H., and Jung, S. W. (2021). Review of capacitive touchscreen technologies: Overview, research trends, and machine learning approaches. *Sensors*. 21(14): 4776.

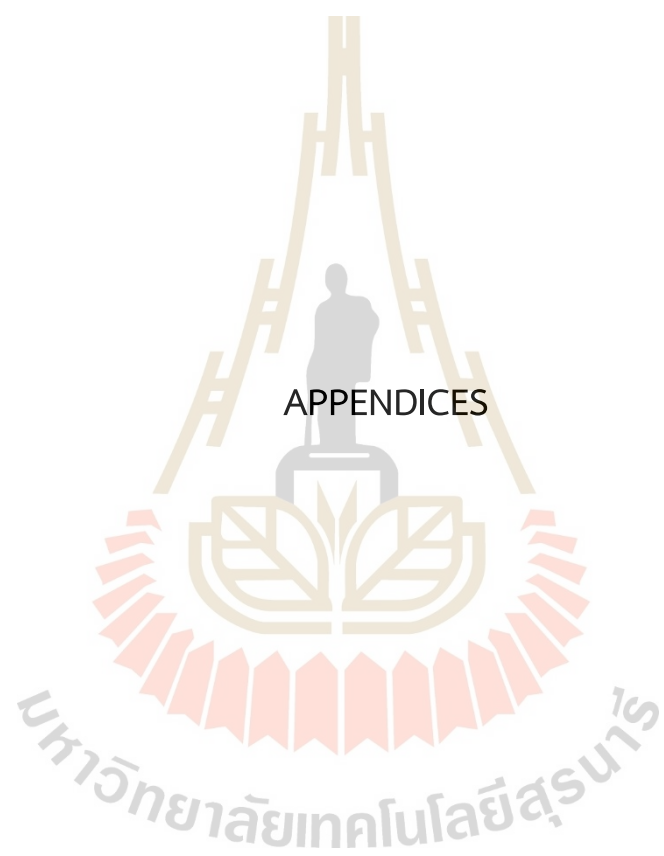
- Nathabumroong, S., Eknapakul, T., Jaiban, P., Yotburut, B., Siriroj, S., Saisopa, T., Mo, S.-K., Supruangnet, R., Nakajima, H., and Yimnirun, R. (2020). Interplay of negative electronic compressibility and capacitance enhancement in lightly-doped metal oxide  $\text{Bi}_{0.95}\text{La}_{0.05}\text{FeO}_3$  by quantum capacitance model. *Scientific reports*. 10(1): 1-6.
- Ohtomo, A., and Hwang, H. (2004). A high-mobility electron gas at the  $\text{LaAlO}_3/\text{SrTiO}_3$  heterointerface. *Nature*. 427(6973): 423-426.
- Pei, W., Chen, J., You, D., Zhang, Q., Li, M., Lu, Y., Fu, Z., and He, Y. (2020). Enhanced photovoltaic effect in Ca and Mn co-doped  $\text{BiFeO}_3$  epitaxial thin films. *Applied Surface Science*. 530: 147194.
- Pollock, D. D. (2018). *Physical properties of materials for engineers*: CRC Press.
- Qiu, J., Li, Y., and Jia, Y. (2020). *Persistent Phosphors: From Fundamentals to Applications*: Woodhead Publishing.
- Riley, J. M., Meevasana, W., Bawden, L., Asakawa, M., Takayama, T., Eknapakul, T., Kim, T., Hoesch, M., Mo, S.-K., and Takagi, H. (2015). Negative electronic compressibility and tunable spin splitting in  $\text{WSe}_2$ . *Nature nanotechnology*. 10(12): 1043-1047.
- Saenrang, W., Davidson, B., Maccherozzi, F., Podkaminer, J., Irwin, J., Johnson, R., Freeland, J., Íñiguez, J., Schad, J., and Reiersen, K. (2017). Deterministic and robust room-temperature exchange coupling in monodomain multiferroic  $\text{BiFeO}_3$  heterostructures. *Nature communications*. 8(1): 1-8.
- Sando, D., Agbelele, A., Rahmedov, D., Liu, J., Rovillain, P., Toulouse, C., Infante, I., Pyatakov, A., Fusil, S., and Jacquet, E. (2013). Crafting the magnonic and spintronic response of  $\text{BiFeO}_3$  films by epitaxial strain. *Nature materials*. 12(7): 641-646.
- Schroder, D. K. (2015). *Semiconductor material and device characterization*: John Wiley & Sons.
- Scigaj, M., Gázquez, J., Varela, M., Fontcuberta, J., Herranz, G., and Sanchez, F. (2015). Conducting interfaces between amorphous oxide layers and  $\text{SrTiO}_3$  (110) and  $\text{SrTiO}_3$  (111). *Solid State Ionics*. 281: 68-72.

- Silva, J., Kamakshi, K., Sekhar, K., Moreira, J. A., Almeida, A., Pereira, M., and Gomes, M. (2016). Light-controlled resistive switching in laser-assisted annealed  $\text{Ba}_{0.8}\text{Sr}_{0.2}\text{TiO}_3$  thin films. *physica status solidi (a)*. 213(4): 1082-1087.
- Singh, C., Thakur, V. N., and Kumar, A. (2021). Polarization controlled resistive switching in bulk ferroelectric ceramics: A universal phenomenon. *Journal of Alloys and Compounds*. 887: 161345.
- Smolenskii, G., Isupov, V., and Agranovskaya, A. (1959). NEW FERROELECTRICS OF COMPLEX COMPOSITION OF THE TYPE  $\text{A}22+(\text{Bi}^{3+}\text{Bi}^{5+})\text{O}^{-6}$ . 1. *SOVIET PHYSICS-SOLID STATE*. 1(1): 150-151.
- Sosnowska, I., Neumaier, T. P., and Steichele, E. (1982). Spiral magnetic ordering in bismuth ferrite. *Journal of Physics C: Solid State Physics*. 15(23): 4835.
- Suwanwong, S., Eknapakul, T., Rattanachai, Y., Masingboon, C., Rattanasuporn, S., Phatthanakun, R., Nakajima, H., King, P., Hodak, S., and Meevasana, W. (2015). The dynamics of ultraviolet-induced oxygen vacancy at the surface of insulating  $\text{SrTiO}_3$  (001). *Applied Surface Science*. 355: 210-212.
- Suwanwong, S., Kullapapinyokul, J., Eknapakul, T., Buaphet, P., Pattanakul, R., and Meevasana, W. (2015). Resistivity change in  $\text{SrTiO}_3$  upon irradiation and its application in light sensing. *Suranaree Journal of Science and Technology*. 22(1): 93-98.
- Tanaka, I., Oba, F., Tatsumi, K., Kunisu, M., Nakano, M., and Adachi, H. (2002). Theoretical formation energy of oxygen-vacancies in oxides. *Materials Transactions*. 43(7): 1426-1429.
- Teague, J. R., Gerson, R., and James, W. J. (1970). Dielectric hysteresis in single crystal  $\text{BiFeO}_3$ . *Solid State Communications*. 8(13): 1073-1074.
- Wan, Z., Kazakov, A., Manfra, M. J., Pfeiffer, L. N., West, K. W., and Rokhinson, L. P. (2015). Induced superconductivity in high-mobility two-dimensional electron gas in gallium arsenide heterostructures. *Nature communications*. 6(1): 1-5.
- Wang, J., Neaton, J., Zheng, H., Nagarajan, V., Ogale, S., Liu, B., Viehland, D., Vaithyanathan, V., Schlom, D., and Waghmare, U. (2003). Epitaxial  $\text{BiFeO}_3$  multiferroic thin film heterostructures. *Science*. 299(5613): 1719-1722.

- Wu, J., and Wang, J. (2010). BiFeO<sub>3</sub> thin films of (111)-orientation deposited on SrRuO<sub>3</sub> buffered Pt/TiO<sub>2</sub>/SiO<sub>2</sub>/Si (100) substrates. *Acta Materialia*. 58(5): 1688-1697.
- Wu, J., Wang, J., Xiao, D., and Zhu, J. (2011). Ferroelectric behavior in bismuth ferrite thin films of different thickness. *ACS applied materials & interfaces*. 3(9): 3261-3263.
- Wu, Y.-T., Yan, T., and Pan, Z.-J. (2020). Wearable carbon-based resistive sensors for strain detection: a review. *IEEE Sensors Journal*. 21(4): 4030-4043.
- Yang, B., Jin, L., Wei, R., Tang, X., Hu, L., Tong, P., Yang, J., Song, W., Dai, J., and Zhu, X. (2021). Chemical Solution Route for High-Quality Multiferroic BiFeO<sub>3</sub> Thin Films. *Small*. 17(9): 1903663.
- Yang, S., Seidel, J., Byrnes, S., Shafer, P., Yang, C.-H., Rossell, M., Yu, P., Chu, Y.-H., Scott, J., and Ager, J. (2010). Above-bandgap voltages from ferroelectric photovoltaic devices. *Nature nanotechnology*. 5(2): 143-147.
- Yi, H., Choi, T., Choi, S., Oh, Y. S., and Cheong, S. W. (2011). Mechanism of the switchable photovoltaic effect in ferroelectric BiFeO<sub>3</sub>. *Advanced Materials*. 23(30): 3403-3407.
- You, L., Zheng, F., Fang, L., Zhou, Y., Tan, L. Z., Zhang, Z., Ma, G., Schmidt, D., Rusydi, A., and Wang, L. (2018). Enhancing ferroelectric photovoltaic effect by polar order engineering. *Science advances*. 4(7): eaat3438.
- Yu, X. L., Wang, Y., Hu, Y. M., Cao, C. B., and Chan, H. L. W. (2009). Gas-Sensing Properties of Perovskite BiFeO<sub>3</sub> Nanoparticles. *Journal of the American Ceramic Society*. 92(12): 3105-3107.
- Yuan, Y., Xiao, Z., Yang, B., and Huang, J. (2014). Arising applications of ferroelectric materials in photovoltaic devices. *Journal of Materials chemistry A*. 2(17): 6027-6041.
- Zhang, F., Jiang, W.-M., Li, C.-J., Jin, Y., Wang, Z., Nie, J.-C., and Dai, J.-y. (2020). Flexoelectric Modulation on the Two-Dimensional Electron Gas at (110) LaAlO<sub>3</sub>/SrTiO<sub>3</sub> Interfaces. *ACS Applied Electronic Materials*. 2(7): 1861-1866.
- Zhang, Y., Lu, H., Xie, L., Yan, X., Paudel, T. R., Kim, J., Cheng, X., Wang, H., Heikes, C., and Li, L. (2018). Anisotropic polarization-induced conductance at a ferroelectric-insulator interface. *Nature nanotechnology*. 13(12): 1132-1136.

- Zhang, Z., Wu, P., Chen, L., and Wang, J. (2011). First-principles prediction of a two dimensional electron gas at the BiFeO<sub>3</sub>/SrTiO<sub>3</sub> interface. *Applied Physics Letters*. 99(6): 062902.
- Zhu, H., Ma, H., and Zhao, Y. (2018). In-situ growth of high-quality epitaxial BiFeO<sub>3</sub> thin film via off-axis RF magnetron sputtering. *Vacuum*. 157: 428-432.





## APPENDIX A

### RF MAGNETRON SPUTTERING SYSTEMS

All experiments in this thesis were carried out on our home-made RF magnetron sputtering systems. These systems consisted of five main parts: a vacuum system, water-cooling system, RF power supply system, magnetron sputtering source, and substrate holder system. The details for each part were given as follows.

#### A.1 Vacuum system

The vacuum system produced a high vacuum at a base pressure of  $\sim 10^{-7}$  Torr, which controlled and monitored the essential process parameters. These systems consisted of a cylindrical stainless steel chamber, vacuum pumps, pressure gauges, and gas flow controllers.

The cylindrical stainless steel chamber had a diameter of 254 mm and a height of 340 mm and was made by the Synchrotron Light Research Institute (SLRI), as shown in Figure A.1. The top and bottom flanges were connected to the substrate holder and magnetron sputtering source, respectively. The right-side flange and gate valve were connected to vacuum pumps, which are a turbomolecular pump, and a dry scroll pump. The left-side flange was connected to the fast-entry access load lock doors. The small flanges on the front and right were reserved for pressure gauges, as shown in Figure A.1.

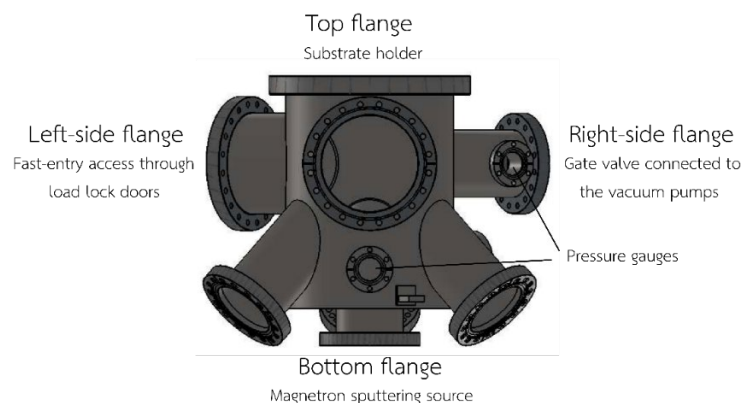


**Figure A.1** A 2-dimensional drawing of the cylindrical stainless steel chamber.

A schematic diagram presenting all the components of the vacuum systems is shown in Figure A.2. The evacuation, operation, and ventilation procedures were the three primary processes for these systems. The chamber was evacuated to a base pressure of below  $8 \times 10^{-7}$  Torr using the vacuum pumps, including the dry scroll pump and turbomolecular pump. The dry scroll pump was employed to decrease pressure in the vacuum chamber with the atmospheric pressure down to  $3 \times 10^{-3}$  Torr. After that, the turbomolecular pump was turned on, and it reduced the pressure to the base pressure, which was monitored by a wide range gauge and displayed on the pressure monitor. The power supply readouts type 247 controlled a mass flow controller (MFC) to adjust the flow rate of argon and oxygen gases. Before the RF magnetron sputtering system was operated, the argon and oxygen gases were introduced and flowed into the chamber in two directions: the bottom of the chamber and the magnetron sputtering source. After the film coating process was completed, the two vacuum pumps and gate valve were turned off, and the nitrogen gas was introduced to the chamber. Finally, the chamber's atmospheric pressure was at  $7.5 \times 10^2$  Torr.

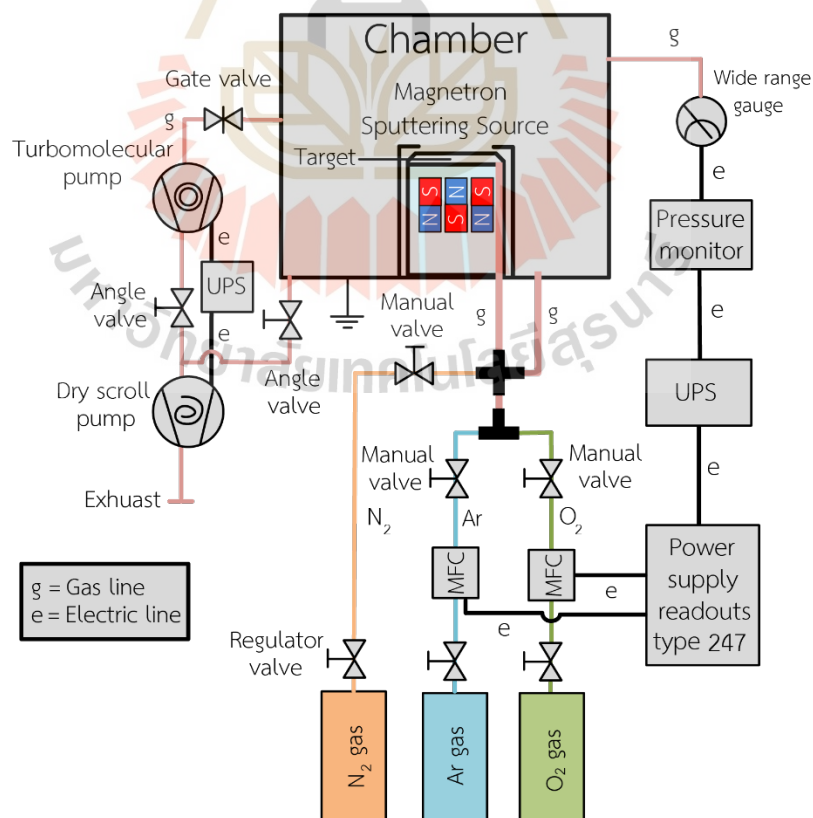


Figure A.2 A schematic diagram of vacuum systems.

## A.2 Water-cooling system

A schematic diagram presenting the water-cooling system is shown in Figure A.3. This system consisted of a water chiller, a water filter, tubes, and ball valves. The water chiller model AX 1.8A was purchased from Advance Cool Technology, Ltd. It controlled water temperatures between 10-15 °C. The cooling water flowed to a water filter to filter coarse sediment before it entered the magnetron sputtering source and turbomolecular pump. The arrows show the direction of the cooling water.

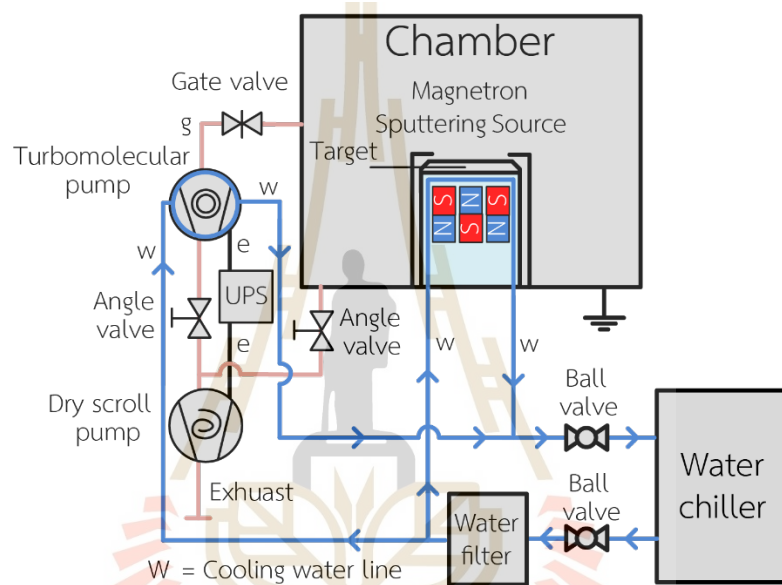
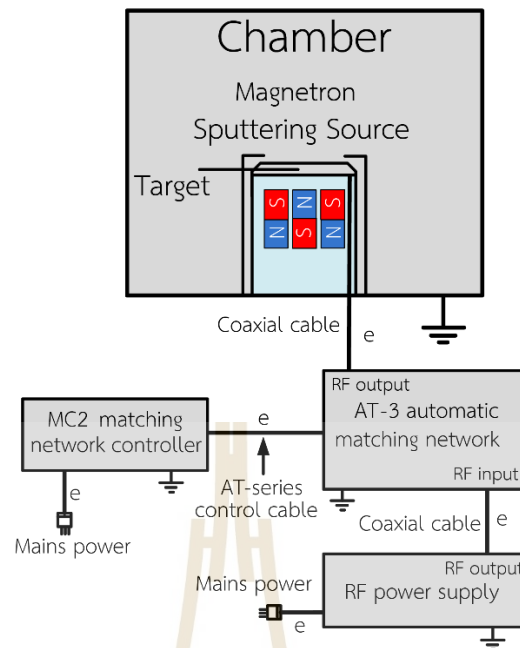


Figure A.3 A schematic diagram of the water system.

## A.3 RF power supply system

A schematic diagram of the RF power supply system by AJA International, Inc. is shown in Figure A.4. The RF power supply system consisted of the RF power supply, model A300RF, It applied power at radio frequency of 13.56 MHz to the AT-3 automatic matching network. The MC2 matching network controller adjusted the appropriate radio frequency in the AT-3 automatic matching network and sent the signal via coaxial cable to the magnetron sputtering sources. The maximum RF power is 300 watts and can be delivered to the source for growing the thin films.



**Figure A.4** A schematic diagram of the RF power supply systems. Noted: e=Electrical line.

#### A.4 Magnetron sputtering sources

The magnetron sputtering source, model A320-XP, was from AJA International, Inc. for a target size of 2.0 inch  $\times$  0.25 inch in diameter. A maximum RF/DC discharge power of 300 watts can be delivered to the source via cable. During the deposition of thin films, the target was cooled by cooling water. The shutter was open. The sputtering atoms were deposited onto the substrate. The target was mounted on a copper cup to have good electrical and heat conductivities.

#### A.5 Substrate holder system

A schematic diagram of the substrate holder system consists of a 2.0 inch sample stage substrate heater by Meivac Inc., model SU-200-HH, and a temperature controller as shown in Figure A.5. The maximum temperature was 950 °C with a ramp time of 12 min. The distance between the substrate and the target was approximately 6 cm. The temperature controller was designed in our lab for a maximum DC voltage of 45 V and a maximum current of 10 A, which corresponds to the specification of the substrate heater.

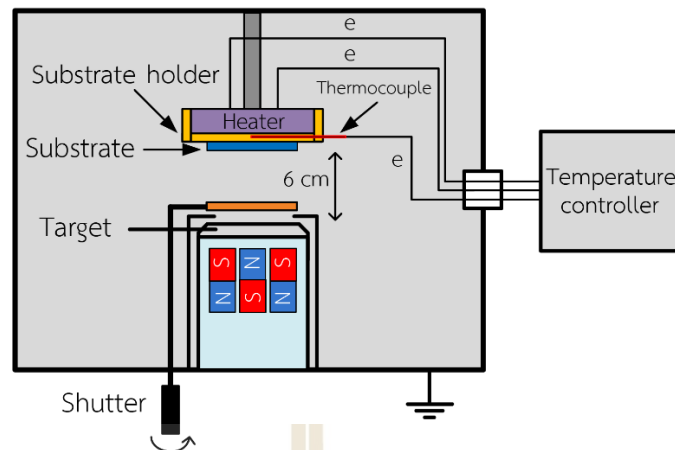


Figure A.5 A schematic diagram of the substrate holder.

## A.6 Deposition procedure

This section shows an operation of the RF magnetron sputtering for the deposition of the BFO thin films. The deposition procedure was as follows:

1. Apply silver paste to the bottom of the sample, then place it on the substrate holder and heat it for 10 minutes at around 80 °C to dry the silver paste.
2. Place the sample in the vacuum chamber and shut the load lock doors.
3. Open the dry scroll pump and the angle valve between the vacuum chamber and the dry scroll pump to evacuate and decrease the pressure down to  $3 \times 10^{-3}$  Torr.
4. Open the water chiller, the gate valve, and the angle valve between the turbomolecular pump and the dry scroll pump (close the angle valve between the vacuum chamber and the dry scroll pump). After that, the turbomolecular pumps were turned on to make the base pressure below  $8 \times 10^{-7}$  Torr.
5. In the case of thin film deposition at room temperature (RT), the Ar and O<sub>2</sub> gases were introduced to the chamber at a flow rate of 16 and 4 sccm (rate ratio of 4:1), and the gate valve was dimmed slowly to set the operating pressure of  $6 \times 10^{-3}$  Torr. Next, the RF power supply and the AT-3 automatic matching network operated the glow discharge at 100 W and set up a pre-sputtering time of 5 minutes. After that, turn on the shutter and set the deposition time.

6. In the case of thin film deposition at high temperatures (HT), the substrate heater was operated up to 600 °C by the power supply heater. While the substrate temperature increased between 300 °C to 600 °C, the Ar and O<sub>2</sub> gases were introduced into the chamber at a flow rate of 16 and 4 sccm (rate ratio of 4:1), respectively, and the gate valve was gradually dimmed to set an operating pressure of 6×10<sup>-3</sup> Torr. The glow discharge was operated at 100 W and set up with a pre-sputtering time of 5 minutes. Then, the pre-sputtering was completed, and the substrate temperature was stabilized at 600 °C. The shutter was open. The sputtering atoms were deposited onto the substrate and set the deposition time. After the thin film deposition was completed, the shutter and raise the temperature to 700 °C for 1 hour to anneal the BFO thin films and purge the O<sub>2</sub> gas at a pressure of 6×10<sup>-3</sup> Torr.

7. After the thin film deposition was completed, the shutter, the power supply readouts type 247 (mass flow controller), the RF power supply, the AT-3 automatic matching network, and the power supply heater (for high temperature) were closed.

8. The gate valve and the angle valve between the turbomolecular pump and the dry scroll pump were closed. In the case of thin film deposition at high temperatures, the substrate heater must reach near room temperature before closing it.

9. To flow N<sub>2</sub> gas to atmospheric pressure, open the manual valve between the N<sub>2</sub> gas tank and the chamber. Bring the sample out of the chamber.

10. In the case of thin film deposition at room temperature and moving to a furnace, the sample was calcined at 600 °C for 2 hours. This process is called “calcination temperatures (CAL)”.

## APPENDIX B

### PUBLICATIONS AND PRESENTATIONS

#### B.1 List of publications

##### B.1.1 First author

Laohana, P., Polin, S., Jindata, W., Rasritat, A., Eknapakul, T., Leuasongnoen, P., Pinitsoontorn, S., Janphuang, P., Saenrang, W., and Meevasana, W. (2022). Large increase in photoinduced conductivity of two-dimensional electron gas at SrTiO<sub>3</sub> surface with BiFeO<sub>3</sub> topping layer. *Applied Physics Letters*. 121(24): 241601.

##### B.1.2 Co-first author

Laohana, P., Tanapongpisit, N., Kim, S., Eknapakul, T., Fongkaew, I., Supruangnet, R., Nakajima, H., Meevasana, W., Bark, C. W., and Saenrang, W. (2021). Particle size dependence of the electrochemical properties of SrMnO<sub>3</sub> supercapacitor electrodes. *Journal of Solid State Electrochemistry*. 25(4): 1121-1129.

Tanapongpisit, N., Wongprasod, S., Laohana, P., Kim, S., Butburee, T., Meevasana, W., Maensiri, S., Bark, C. W., and Saenrang, W. (2022). Effects of the particle size of BaMnO<sub>3</sub> powders on the electrochemical performance of supercapacitor electrodes. *Materials Letters*. 319: 132258.

#### B.2 List of oral presentations

Laohana, P., Saenrang, W., Yotburut, B., Eknapakul, T., Sonsupap, S., Siriroj, S., and Meevasana, W. (2017). Enhanced specific capacitance of activated carbon by BiFeO<sub>3</sub> thin film prepared by RF magnetron sputtering. *The First Materials Research Society of Thailand International Conference*. Chiang Mai, Thailand.

Laohana, P., Meevasana, W., and Saenrang, W. (2020). Photoresistive property in planar Au/BiFeO<sub>3</sub>/Au structure. *The 5<sup>th</sup> International Conference on Smart Materials and Nanotechnology*. Chonburi, Thailand

Laohana, P., Saenrang, W., Polin, S., Eknapakul, T., and Meevasana, W. (2021). Enhancement of photo-induced conductivity of two-dimensional electron gas at SrTiO<sub>3</sub> surface with BiFeO<sub>3</sub> topping layer. *The 21<sup>st</sup> International Union of Materials Research Societies - International Conference in Asia*. An online meeting.

### B.3 List of poster presentation

Laohana, P., Saenrang, W., Yotburut, B., Eknapakul, T., Polin, S., Siriroj, S., and Meevasana, W. (2019). Photoresistance properties of BiFeO<sub>3</sub> thin films on SrTiO<sub>3</sub> substrates prepared by RF magnetron sputtering. *The 2<sup>nd</sup> Materials Research Society of Thailand International Conference*. Chonburi, Thailand.



## APPENDIX C

### SUPPLEMENTARY RESULTS

#### C.1 Atomic force microscope (AFM)

The atomic force microscope (AFM) is used to investigate the thickness of BFO thin films in cross-section. To average film thickness, we used data from five cross-section lines. The thickness of the BFO/STO at RT, HT, and CAL conditions is shown in Figure C.1. The deposition rate is calculated from the deposition time of 1, 5, and 30 min under all conditions. To find the deposition rate, we used a linear function to fit the graph. The deposition rates were 24.90, 16.36, and 14.15 nm/min at RT, HT, and CAL conditions, respectively.

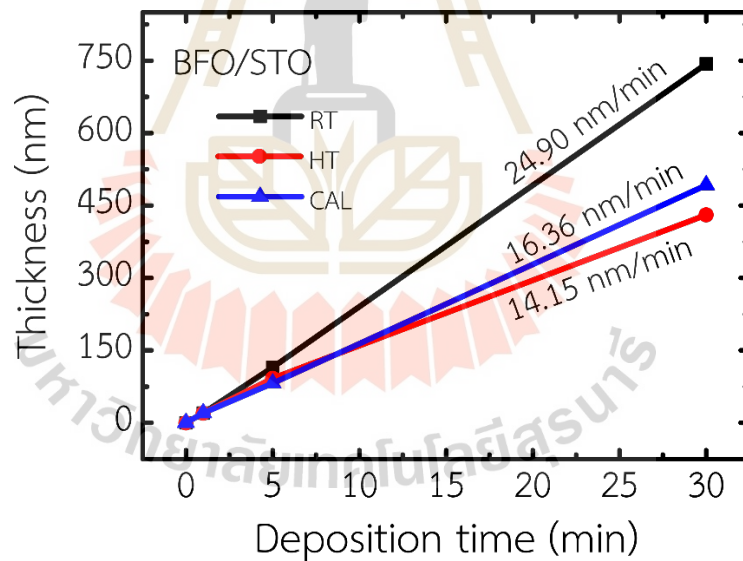
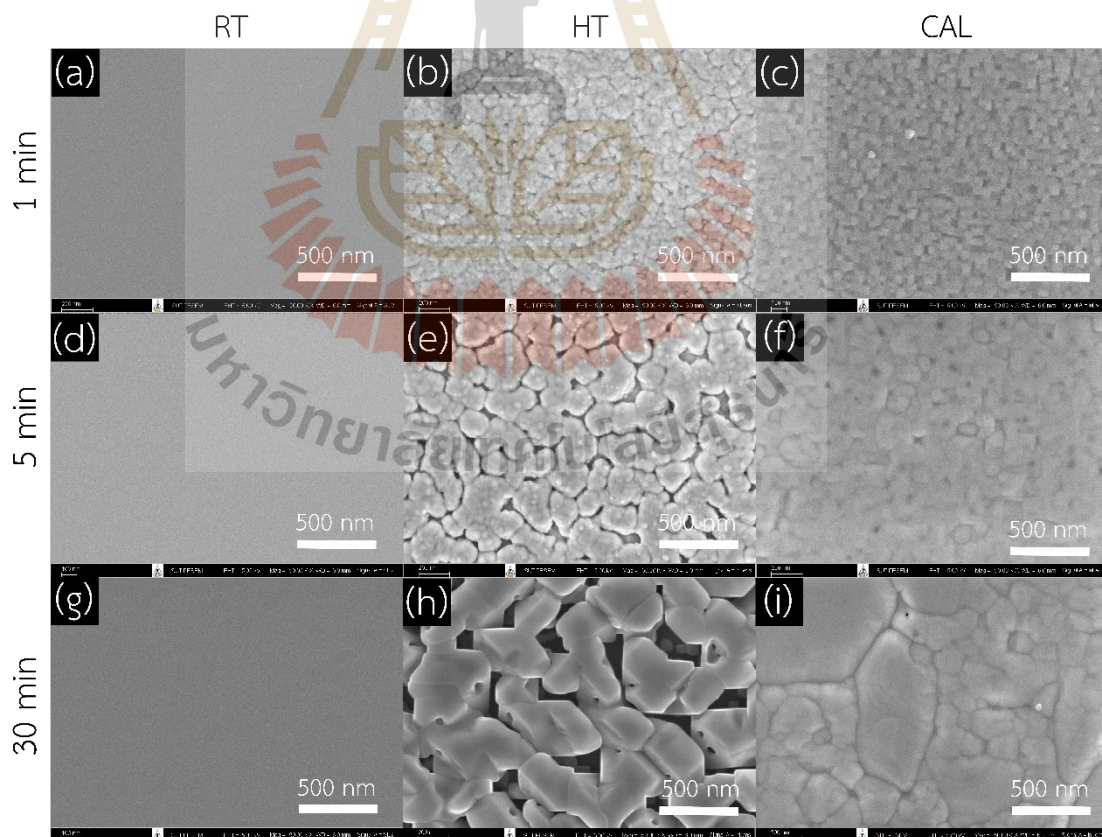


Figure C.1 The thickness of the BFO/STO at RT, HT, and CAL conditions.

#### C.2 Field emission scanning electron microscope (FESEM)

The morphology of the STO crystal and the BFO/STO sample were studied by FESEM using 50 kX magnification. Figure C.2(a-i) shows the morphology in RT, HT, and CAL conditions with deposition times of 1, 5, and 30 min. The morphology of BFO thin films with various deposition times exhibits a smooth and uniform surface at RT

conditions, as illustrated in Figures C.2(a), (d), and (g). The FESEM images of HT and CAL conditions reveal the crystalline grains to increase with deposition time. As shown in Figure C.2(b), and (c), the surface is uniformly distributed and have small pore for deposition times of 1 min. In addition, the deposition times were increased to 5 and 30 min, the crystalline grains and pore sizes have increased. Figure C.2(e) shows the BFO thin film growth with layer-by-layer plus islands, which we observed on the crystalline grains. While the BFO thin film in the CAL condition is denser in the crystalline grains than in the HT condition, as shown in Figure C.2(f). The crystalline grains and pore sizes were very large at the highest deposition times due to growing in HT conditions with the island model, as illustrated in Figures C.2(h). The effect of calcination combines the crystalline grains together, as shown in Figure C.2(i). As a result, these images indicate different features of the crystalline grains and pore sizes due to different crystal orientations according to the x-ray diffraction spectra, as shown in Figure 4.1.



**Figure C.2** FESEM images of the BFO/STO sample in RT, HT, and CAL conditions with deposition times of 1, 5, and 30 min.

### C.3 Energy dispersive X-ray spectroscopy (EDS)

The elemental composition of the STO crystal and BFO/STO thin films was analyzed by energy dispersive X-ray spectroscopy (EDS). The EDS elemental analysis of the BFO/STO thin films in HT conditions is shown in Figure C.3. Each figure summarizes the number of elements in the weight percent and atomic percent. The Bi element cannot be detected at the BFO for 1 and 5 min due to the highly volatile nature of Bi atoms at high temperatures, as shown in Figure C.3(a) and (b). The atomic percent of Fe was increased with increasing deposition times. The EDS results of all conditions show the Sr, Ti, and O elements because pore sizes were very large, as shown in FESEM images in Figure C.2(b), (e), and (h). The ratio of atomic percent between Sr, Ti, and O was almost 1:1:3 in both conditions, where the atomic percent of O came from BFO thin films. However, the Bi element can be identified at the BFO for 30 min, as shown in Figure C.3(c). Although the amount of Bi is small compared to the Fe elements, the BFO reflection peaks of the HT condition were shown to be higher than those of the CAL condition, as shown in Figure 4.1. That indicates the BFO thin films are almost epitaxial films, which is indicated by the XRD result as shown in Figure 4.1.

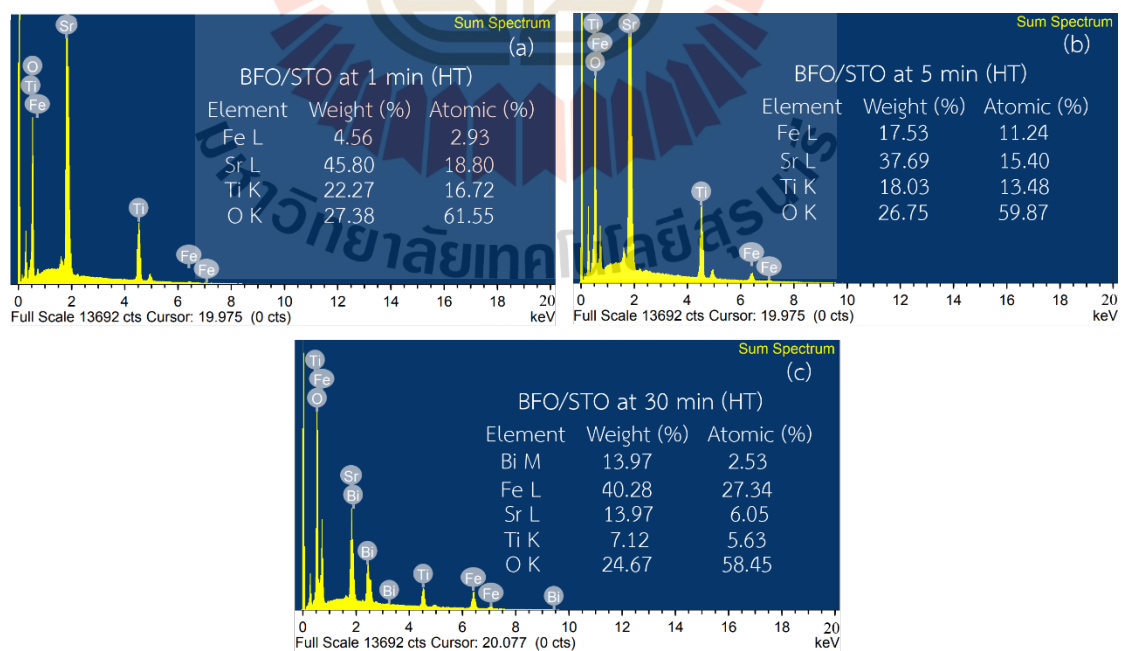


**Figure C.3** EDS elemental analysis of BFO on STO thin films in HT conditions with deposition times of (a) 1 min, (b) 5 min, and (c) 30 min.

Figure C.4 shows the EDS elemental analysis of the BFO/STO thin films in CAL conditions. With increasing deposition times, the atomic percent of Bi and Fe increased while Sr and Ti decreased together with RT and HT conditions. The BFO for 1 and 5 min has a thickness of around 20 and 120 nm, respectively, and many pores, while the BFO thin film at 30 min (the thickness of 430 nm) is denser, as shown in Figure C.2(c), (f), and (i). An electron beam can penetrate the BFO thin film, so we can detect Sr and Ti elements, as shown in Figure C.4(a) and (b). The quantity of Bi is little in comparison to the amount of Fe elements according with HT conditions because of the volatile nature of Bi atoms. Therefore, the atomic ratios of the BFO thin film were not 1:1:3, while the CAL conditions showed the BFO reflections together with the STO peaks of the STO substrate, as shown in Figure 4.1. This suggests that the BFO thin films are nearly epitaxial, which is indicated by the XRD result as shown in Figure 4.1.

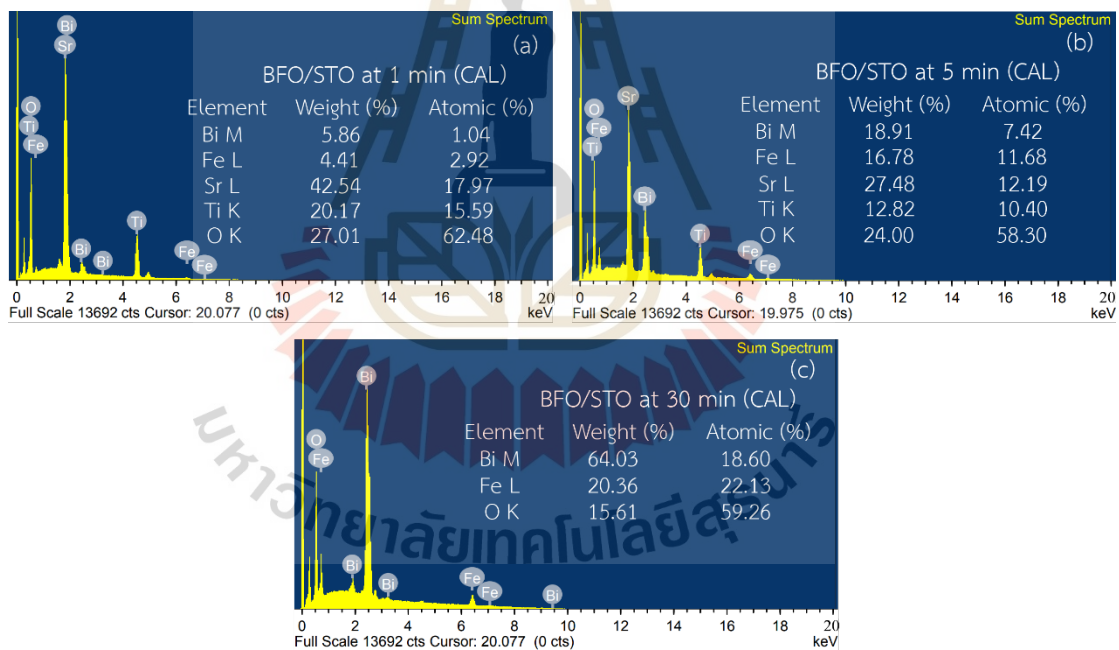


**Figure C.4** EDS elemental analysis of BFO on STO thin films in CAL conditions with deposition times of (a) 1 min, (b) 5 min, and (c) 30 min.

## CURRICULUM VITAE

**Name** Mr. Peerawat Laohana

**Date of birth** December 9, 1992

**Place of birth** 27/3 Srivised Rd., Mueang Nuer Sub-district,  
Mueang District, Sisaket Province, Thailand.

**Education**

2015-2022 **Doctor of Philosophy (Physics): Ph.D. (Physics)**  
Suranaree University of Technology, Nakhon Ratchasima,  
Thailand.

2011-2014 **Bachelor of Science (Physics): B.Sc. (Physics)**  
Mahasarakham University, Maha Sarakham,  
Thailand.

**Grants and Fellowships** Science Achievement Scholarship of Thailand  
(SAST)

**Publications**

Laohana, P., Polin, S., Jindata, W., Rasritat, A., Eknapakul, T., Leuasongnoen, P., Pinitsoontorn, S., Janphuang, P., Saenrang, W., and Meevasana, W. (2022). Large increase in photoinduced conductivity of two-dimensional electron gas at SrTiO<sub>3</sub> surface with BiFeO<sub>3</sub> topping layer. *Applied Physics Letters*. 121(24): 241601.

Tanapongpisit, N., Wongprasod, S., Laohana, P., Kim, S., Butburee, T., Meevasana, W., Maensiri, S., Bark, C. W., and Saenrang, W. (2022). Effects of the particle size of BaMnO<sub>3</sub> powders on the electrochemical performance of supercapacitor electrodes. *Materials Letters*. 319: 132258.

Laohana, P., Tanapongpisit, N., Kim, S., Eknapakul, T., Fongkaew, I., Supruangnet, R., Nakajima, H., Meevasana, W., Bark, C. W., and Saenrang, W. (2021). Particle size dependence of the electrochemical properties of SrMnO<sub>3</sub> supercapacitor electrodes. *Journal of Solid State Electrochemistry*. 25(4): 1121-1129.